NTNU
Norwegian University of
Science and Technology

Pulsed Laser Deposition of ZnO Nanostructures for Hybrid Inorganic/ Organic Solar Cells

Daniel Gundersen Skåre

Master of Science in Electronics
Submission date: June 2009
Supervisor: Helge Weman, IET
Co-supervisor: Christian Weigand, IET

Norwegian University of Science and Technology
Department of Electronics and Telecommunications

Problem Description

Hybrid inorganic/organic solar cells are promising candidates for achieving low-cost solar cell devices. Nanostructural control of the morphology of the inorganic acceptor bears potential for improving charge transfer and conversion efficiencies in such devices by creating direct charge carrier pathways and increasing surface area, respectively. ZnO as a wide band gap material is a promising inorganic acceptor material, because of its transparency (band gap 3.37eV) and its low price due to great abundance. Pulsed laser deposition (PLD) allows for controlled growth of thin films and nanostructures of various materials, including ZnO.

In the proposed master project, the student will prepare ZnO nanostructures by PLD with the idea of implementing the grown structures in hybrid organic/inorganic solar cells. The influence of different growth parameters such as substrate treatment and growth catalyst will be investigated by characterizing the grown samples using scanning electron microscopy (SEM) and x-ray diffraction measurements (XRD). Throughout the project, the student will gain valuable practical experience in dealing with ultra-high vacuum (UHV) chambers and state-of-the-art high-resolution characterization techniques important in thin film analysis, not only ZnO growth. With his work, the student can significantly contribute to the understanding of how ZnO nanorods grown by PLD and how the growth of these nanostructures could be controlled for the use in hybrid inorganic/organic solar cell devices.

For the growth of the ZnO nanostructures, a technique was chosen that uses a Au catalyst to aid the ZnO nanostructure growth. This has been shown to lead to promising nanostructures. Investigation around the Au catalyst growth and the substrate annealing treatment will therefore be the focus of this master project.

Assignment given: 20. January 2009
Supervisor: Helge Weman, IET

Abstract

Au catalyst ZnO nanostructures have been grown on the a- and c-plane sapphire substrate by PLD. Influence of substrate lattice orientation, substrate surface and different substrate annealing temperature have been characterized by AFM, SEM and XRD.

This report shows that a-plane sapphire substrate annealed at 1000°C and 1200°C improves the growth condition of Au catalyst ZnO nanostructures. For c-plane sapphire; annealing at 1200°C and 1400°C enhances the nanostructure growth. The better growth condition is a result of the terrace-and-step morphology seen on the substrate surface prior to growth.

This report also indicates a correlation between the azimuthal in-plane alignment of the grown nanostructures and the sapphire substrate lattice orientation.

Preface

In 2007, the Research Council of Norway was, in addition to the National Science Foundation, granted funding of a collaboration research project between Colorado School of Mines (US), SINTEF materials and chemistry and NTNU. The project aim was at nanostructured oxide thin films for organic/inorganic solar cell applications. Implementation of nanostructures in traditional applications is a new and revolutionary phenomenon, which result in different behavior and improvements in many areas.

This report is a result of a work carried out at the Department of Electronics and Telecommunications at NTNU during spring 2009. During the semester, I have worked within an international research group. This has given me a lot of experience at the laboratory, theoretical insight, but most of all I have learned the value of team-work, discussions and sharing information. Several persons have been involved during my work and I would like to thank all of them. Christian Weigand has acted as a supervisor and a great partner for discussion, even though he has been in the US during the semester, communication has worked great through e-mail, video conference and instant messages. Øystein Dahl has been of great help at the lab and I thank you for your time. I would also like to thank my supervisor professor Helge Weman. A special thanks goes to Cécile Ladam, who has been a unique guide and a remarkable discussion partner throughout the project.

In the end, I would just like to say that it has been a pleasure working with all of you, and I wish you the best of luck with the future work.

Trondheim, June 2009
Daniel Gundersen Skåre

Contents

List of Abbreviations

AFM	Atomic Force Microscopy
CL	Cathodoluminescence
CM	Contact Mode
EDX	Energy Dispersive Spectrometry
FTO	Fluorine-doped Tin Oxide (SnO_2:F)
FWHM	Full Width at Half Maximum
HOMO	Highest Occupied Molecular Orbital
HSC	Hybrid inorganic/organic Solar Cell
ITO	Indium Tin Oxide or tin-doped indium oxide (In_2O_3:Sn)
kWh	Kilo Watt Hour
LUMO	Lowest Unoccupied Molecular Orbital
LVFe-SEM	Low Voltage Field Emission SEM
MEH-PPV	Poly[2-methoxy-5-(2'-ethyl- hexyloxy)-1,4-phenylene vinylene]
MOCVD	Metal-Organic Chemical Vapor Deposition
oBHJ	Organic Bulk Heterojunction
OPVC	Organic Photovoltaic cell
OTES	Octadecyltriethoxysilane
P3HT	Poly(3-hexylthiophene)
$PC_{70}BM$	[6,6]-phenyl-C_{71} butyric acid methyl ester
PCBM	Fullerene derivative [6,6]-phenyl-C_{61}-butyric acid methyl ester
PEDOT:PSS	Poly(3,4-ethylenedioxylenethiophene): Polystyrene sulfonic acid
PLD	Pulsed Laser Deposition
PVD	Physical Vapor Deposition
R.M.S.	Root-Mean-Square
SAM	Scanning Auger electron Microscope
SE	Secondary Electrons
SEM	Scanning Electron Microscopy
SFM	Scanning Force Microscopy
SPM	Scanning Probe Microscopy
TEM	Transmission Electron Microscopy
TESP	Tapping Mode Etched Silicon Probe
TiO_x	Titanium(IV) isopropoxide ($Ti[OCH(CH_3)_2]_4$)
TM	Tapping Mode
TSST	Twente Solid State Technology
VLS	Vapor-Liquid-Solid (growth mechanism)
VS	Vapor-Solid (growth mechanism)
XRD	X-Ray Diffraction

List of Figures

List of Tables

Chapter 1

Introduction

In recent years, the worldwide community has drawn their attention towards sustainable development and renewable energy. Higher energy demands has made it important to conduct research in solar cell technology for use in future applications. In present day, there are many different types of solar cells. These types are very different in technology and mean of usage, but the common functionality is that they can harvest low quality energy in the sunlight and transform it into high quality energy in the form of electrical energy. On the commercial market today 85% of the solar cells consist of expensive silicon wafers [1]. This tendency is believed to change, and the traditional solar cells will be substituted by either more efficient solar cells or less expensive solar cells (this as a reduction of efficiency).

Hybrid inorganic/organic solar cells (HSC) are a low cost/low efficiency solar cell. It is a relatively new technology, which have increased in research activity over the past few years. HSC is traditionally an organic solar cell consisting of a polymer as the photoactive layer with a metal oxide introduced to improve the efficiency of the solar cell. Introducing metal oxides (e.g. ZnO, TiO_2 SnO_2 or Fe_2O_3) into organic solar cells offers high physical and chemical stability, and has therefore been widely investigated as a material for polymer PV conversion [2, 3, 4]. The TiO_2 semiconductor has been the most studied, but also ZnO in HSC has shown growing interest due to its large band gap (E_g=3.37eV) and high exciton binding energy ($E_{binding}$=60meV) [5]. In addition, the ZnO is a low-cost material (because of its abundance), is an environmentally friendly material and it has the possibility of being synthesized with a variety of methods (e.g. PLD, CVD, MBE, VPE) [6, 7, 8, 9]. Because of its unique physical properties, ZnO has been used in applications such as ultraviolet/blue emission device (LED and lasers), solar cells, chemical sensor, surface acoustic wave (SAW) devices, logic circuits and field effect transistors (FET) [10, 11, 12, 13, 14, 15].

1.1 Basis of thesis

In this master thesis, ZnO nanostructures have been prepared by PLD with the idea of implementing the grown structures in HSC. The goal of this work is to gain knowledge and control of the ZnO nanostructure growth parameters. In this work the influence of substrate structure and substrate treatments such as lattice orientation of substrate, annealing condition and a general understanding of how the growth occurs will be investigated. Characterizing the grown samples using scanning electron microscopy (SEM) and atomic force microscopy measurements (AFM) will be of importance. For ZnO nanostructures growth, Au as a catalyst will be used. Also, investigating the catalyst Au (gold) droplet formation has been an essential part of this work.

1.2 Thesis Outline

This thesis starts with an introduction to photovoltaic cells (PVC), chapter 2. Here, HSC is discussed as a special case, how it works, advantages and limitations. In our case, HSCs are made by growing ZnO nanostructures, and in chapter 3 an introduction to growth theory, which is important in this work, has been described. In chapter 4, the characterization tools used during this work have been described followed by a detailed description of experimental procedure in chapter 5. The first experiment regarding annealing of sapphre substrate and the results and discussion is given in chapter 6. The results of an investigation of Au droplets formed on top of the sapphire substrate is described in chapter 7. In chapter 8, experimental results shows the influence of the annealed substrate including a discussion part. In the final chapter, the thesis is concluded.

Chapter 2

Photovoltaic Cells

Even though most of the work has been carried out on the material growth rather than the actual solar cell device, it is important to understand the background of hybrid inorganic/organic solar cells (HSC). In this chapter an introduction on the HSCs will be given, in order to motivate our work.

The term photovoltaic cell (PVC) is a preferential term used when the source of illumination is not specified, in contradiction to a solar cell where the sun or solar spectrum is the source. In this chapter, the main focus will be on organic PV cells (OPVC), and as a special case hybrid organic/inorganic PVC.

2.1 Generation of PV cells

As there are so many different types of solar cells, a classification into three different categories has been commonly accepted. These categories are deduced from the term cost/kWh and shows how much it costs to produce a solar cell versus the efficiency the cell can achieve. In figure 2.1, the three generations of solar cells are depicted. First generation is today's most common solar cell, which is based on a rather old and expensive p-n doped silicon technology. Second generation, or thin film solar cells, consists of less expensive material than first generation, but more research is needed in order to obtain the depicted efficiencies. Third generation solar cells have a lot of research in progress, and concepts such as quantum-dot, intermediate band structure, hot electron diffraction, sunlight concentration and many others, are investigated to improve the efficiency towards the thermodynamic limit of 86.8% [16]. In the future it is believed that the second and third generation solar cells will be commercially available and will make up for the large production costs of first generation cells. The target group for second and third generation may be shared according to the area of application. As the high efficiency third generation solar cells are needed in large consumption electronics where no other energy sources are available. For an example, it can be used in satellites and space crafts, while the second generation can be used in small every day-use electronics like cell phones and laptops. In this way both technologies may have a bright future.

Inorganic semiconductors, such as mono- and multi-crystalline Silicon, are some of the most effective solar cells there is. These traditional solar cells (Si crystalline) can collect up to nearly 25% of the incoming solar energy [17]. Unfortunately, this efficiency is approaching its theoretical upper limit of 33% [18]. By using more expensive material and advanced production techniques, even higher power conversional energies are found for the third generation of solar cells. I.e. 26%, 34%, 40.7% for GaAs (crystalline), GaInP/GaInAs/GaInAs (tandem) and Low-AOD spectrum

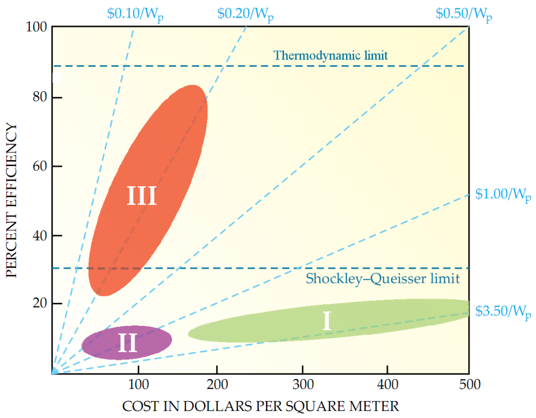

Figure 2.1: Generation of Solar Cells. The horizontal axis represents the cost of the solar cell module only, packing and mounting may double this value. Dotted lines indicate the cost per watt of peak power (W_p). Adapted from source: [1].

GaInP/GaAs/GaInAs, respectively [19, 20, 21] (2008). These PV cells require many lithographic steps, high vacuum conditions, many high energy intensive processes at high temperature which give rise to expensive production costs. This leads to a long payback period typically from 1-4 years depending on the type and location of use [22]. As an alternative to high cost/high efficiency solar cells[1] a search for low cost solar cells with satisfying efficiency has been a goal for many scientists.

2.2 Organic Photovoltaic cell (OPVC)

Organic PVC is a subcategory of the excitonic solar cells. It has recently been in focus because of its significant progress in efficiency. The efficiency of thin film plastic solar cells using a polymer-fullerene bulk heterojunction as a photon absorber has risen sharply. Since the first efficient charge transfer between excited organic semiconductors and fullerene was discovered in 1992 [23] the efficiency has increased more than 6% in less than 15 years, as shown in table 2.1. As higher efficiency is achieved, a more complex layer structure is fabricated. In order to implement low cost solar cells in industry, efficiency above approximately 10% is desirable, and in order to succeed, a lot of research in alternative materials (e.g. metal oxides) and optimization of the cells is needed. In this section a principle of operation for the OPVC is given.

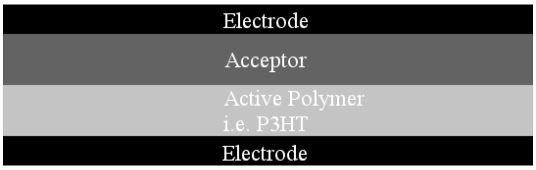

Figure 2.2: Planar organic heterojunction solar cell.

---

[1] high cost/high efficiency - 3rd generation solar cell

Cell structure	Efficiency	Year	V_{oc}[mV]- I_{sc}[mA/cm^{-2}]- F.F.	Reference
Polymer(P3OT,PHDK,MEH-PPV)/C60	-	1992	- - -	[23]
Glas/Plastic: ITO: MEH-PPV/C_{60}: Al/Ca	$< 1\%$	1995	- - -	[24]
Glas: ITO: PEDOT/PSS: P3HT/PCBM: Ca/Ag	2.8%	2002	580 - 8.7 - 0.55	[25]
Glas: ITO: PEDOT/PSS: P3HT/PCBM: Al/LiF	3.5%	2003	550 - 8.5 - 0.6	[26]
Glas: ITO: PEDOT/PSS: P3HT/PCBM: Al	4.4%	2005	610 - 10.6 - 67.4	[27]
Glas: ITO: PEDOT/PSS: P3HT/PCBM: TiO_x: Al	5.0%	2006	610 - 11.1 - 0.66	[28]
Glas: ITO: PEDOT/PSS: PDTBT/PCBM: TiO_x: PEDOT/PSS: P3HT/PC_{70}BM: TiO_x :Al$^{*)}$	6.5%	2007	1240 - 7.8 - 0.67	[29]

Table 2.1: Progress for the OPVC. F.F - Fill factor. $^{*)}$Tandem Cell.

2.2.1 Principle of operation

In all PV cells, there are a material which absorbs the energy of the photons and converts it in electrical charges. This can be done by creating a free electron hole pair (EHP) as in traditional silicon solar cell, or creating a bound EHP (exciton) as in OPVC [30]. In a planar OPVC, the exciton created in the active layer diffuses towards the acceptor interface (see figure 2.2), where the exciton is transformed into two separated charges. The positive and negative charges drift towards each electrode because of a built in electric field. The reason why these strongly bound excitons consist in these polymeric materials is because of the weak, non-covalent, van der Waals interactions between the molecules. This results in a low intermolecular orbital overlap and low dielectric constant in the organic solid. This is why the electron and the hole do not dissociate as they do in high dielectric inorganic materials. The exciton possess a much higher probability of recombination, contrary to the EHP found in traditionally solar cell. If recombination occurs, the photon energy is lost and cannot be transferred into electrical energy.

An advantage of the organic material is the high peak optical absorption coefficient and the direct band gap. As a result of the high absorption, the layer only has to be in the range of 100-500nm thick, to absorb most of the light, this in contrast to crystalline Si PVCs, which must be made in the size of around 100μm [31]. In order to collect most of the excitons the polymer layer has to be very thin as the exciton diffusion length is in order of 3-40nm [32]. This becomes a trade-off between absorption length and exciton diffusion length which leads to that only a small region near the interface contributes to the photocurrent. This limitation result in a very low efficiency for this kind of device. In order to increase the interface and absorption area the bulk heterojunction is introduced.

2.2.2 Organic bulk heterojunction (oBHJ)

There are mainly two types of oBHJ; disordered bulk heterojunction and ordered bulk heterojunction, see figure 2.3(a) and (b), respectively. Here, the disordered HJ is a chemical compound of a conjugated polymer and an electron acceptor (e.g. P3HT:PCBM). The physical structure and the active layer are of importance to optimize the cell. The active layer has widely been investigated by mixing different chemical solutions. Materials absorb different types of spectrum and are more or less suited in solar cells application. A solution which has been used extensively, and shows potential for improvements, is the P3HT:PCBM compound. These devices rely on ultra-fast photo induced charge transfer between the electron donor (P3HT) and the acceptor (PCBM). This is despite the narrow absorption spectrum where researchers are working on making a polymer which absorbs more in the red and IR region. Another problem with chemical solution is the fact that even if the exciton is dissociated, it is not always a conductive path for the charges to travel in order to reach the electrodes. EHP recombination is therefore a problem. Another problem is the poor hole mobility.

In the ordered HJ, the idea is to control the distance between the conjugated polymer and the electron acceptors. This is done by nanostructuring highly aligned metal oxides, e.g. ZnO, TiO_2 SnO_2 or Fe_2O_3 [2, 3, 4]. Common materials used for electrodes are Ag (Al is also common) as cathode and ITO[2] or FTO[3] as the transparent anode. The cathode has been selected from a suitable low work function in order to collect the holes, while the anode has been selected from a high work function to extract the electrons (see figure 2.3(c)).

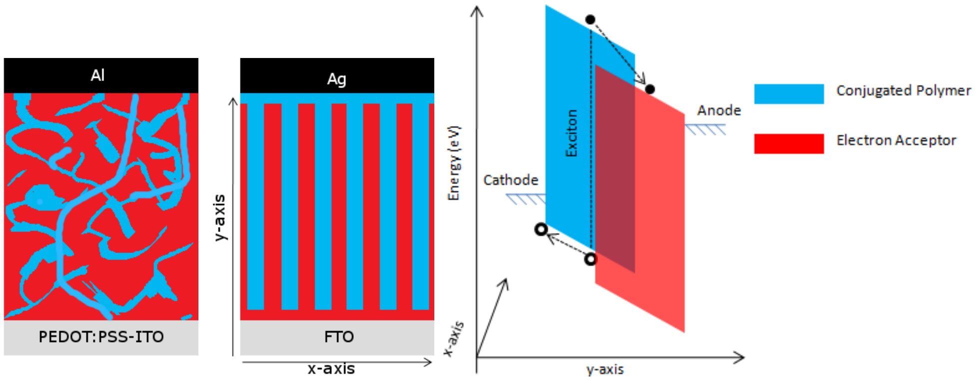

(a) (b) (c)

Figure 2.3: Two different types of polymer bulk heterojunction solar cell. (a) Disordered bulk heterojunction. (b) Ordered bulk heterojunction. (c) Energy band structure for ordered bulk HJ.

The energy conversion and absorption process is similar to the planar OPVC. It consists of four fundamental steps in the commonly accepted energy transfer mechanism [33]:

1. Absorption of light and generation of excitons
2. Diffusion of the excitons
3. Dissociation of the excitons with generation of charge
4. Charge transport and charge collection

These four steps can be illustrated as in figure 2.4 for the ordered bulk HJ solar cell. 1) The sun light passes through the transparent electrode and get absorbed by the conjugated polymer

---

[2] Indium Tin Oxide or tin-doped indium oxide (In_2O_3:Sn)

[3] Fluorine-doped Tin Oxide (SnO_2:F)

where an exciton is created. This exciton diffuses between the aligned nanorod structure and has a very short life time and diffusion length 2). The exciton make contact with a nanorod where charge dissociation occurs 3). The positive charge is transported inside the polymer material, while the negative charge is transported inside the acceptor material 4). The main objective for nanostructering the electron acceptor (or the active layer) is to dissociate the exciton before recombination. The distance between the electron acceptor rods should therefore be on the order of the exciton diffusion length, while the size or diameter of the rods should not be limit the electron transport, neither should the diameter be too large since this would limited to the absorption volume.

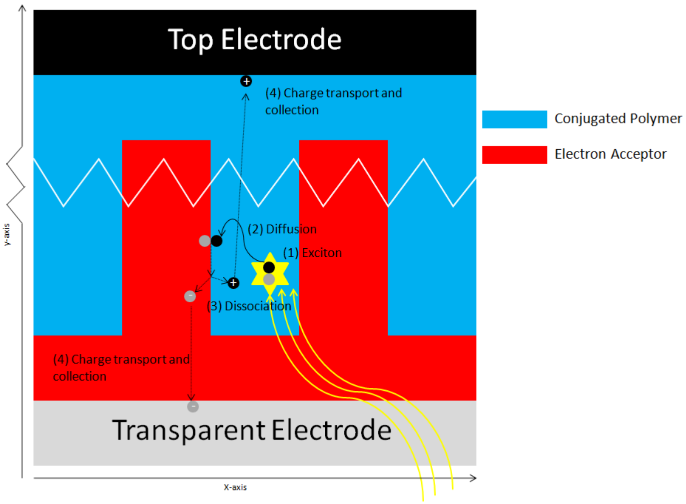

Figure 2.4: Four steps for the energy conversion process

In the ordered bulk HJ, which is of special interest in this thesis, the energy bands occur in a more 3-Dimensional way. This is because the dissociation of the exciton can occur in the x-direction, while the charge transfer occur in the y-direction making the PVC more efficient, see figure 2.3(c). Introducing a nanostructured periodic array is believed to increase the exciton dissociation remarkably. By focusing on the energy conversion in the form of energy band, it is seen in figure 2.5 that the exciton dissociation and charge diffusion is energetically favorable. The photon can be absorbed both in the donor and the acceptor material depending on the material properties. In figure 2.5(a), only photon absorption in the donor (active polymer) is shown. The exciton migrates to the donor-acceptor interface and during this migration, a probability of the exciton to decay to the ground state via radiative or non-radiative process is present, figure 2.5(b). At the interface, the electron leaves the exciton connection and charge separation occurs. This is because of the energy offset of the donor and acceptor orbitals, figure 2.5(c). It is an exothermic process which reduces the V_{OC} and makes the cell less efficient [34]. This kind of polymer works like a semiconductor, where the valence band is called highest occupied molecular orbital (HOMO) and the condution band is called lowest unoccupied molecular orbital (LUMO). Note that the difference in the energy of the HOMO and the conduction band of ZnO is directly related to the open circuit voltage of the solar cell. After the exciton dissociation, the donor (e.g. P3HT) transport the hole to the cathode and the acceptor (e.g. ZnO) transports the electron to the anode, figure 2.5(d).

One of the biggest problems in organic PVC and in excitonic solar cells is the short lifetime, or short diffusion length of the exciton, given in equation 2.1. By gaining control of metal oxide

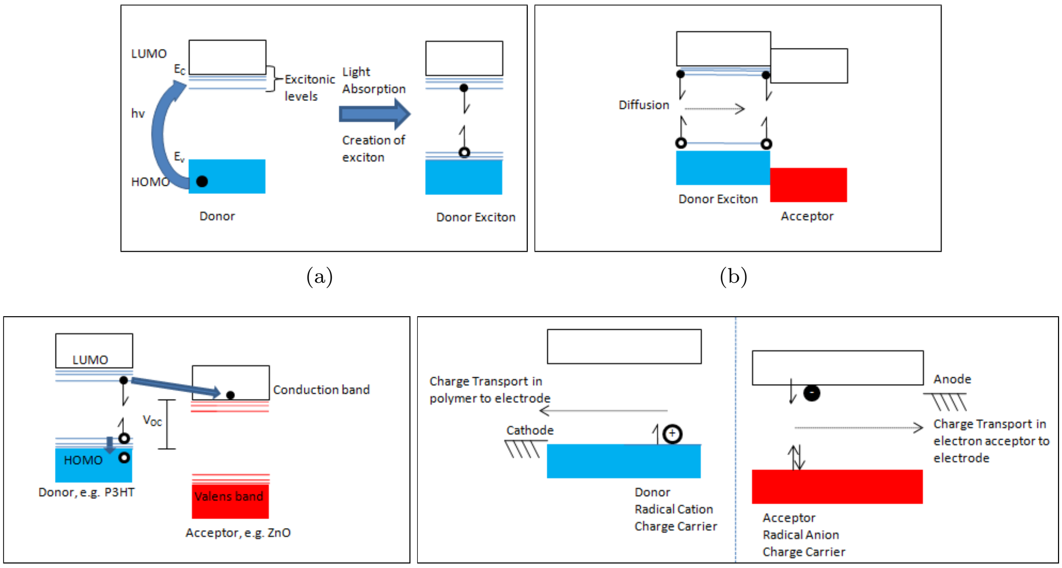

(a) (b)

(c) (d)

Figure 2.5: Four steps for the energy conversion process. (a) Absorption of light and generation of excitons, (b) Diffusion of the exciton, (c) Dissociation of the exciton with generation of charge, (d) Charge transport to the electrodes.

nanorod growth, the solar cell may be less influenced by this limitation.

$$L_D = \mu\tau E = \mu\tau \frac{V - V_{bi}}{d} \tag{2.1}$$

,where μ is the mobility of the exciton, τ is the carrier recombination time, E is the electric field, V is a given potential in the PVC, V_{bi} is the built in potential and d is the thickness of the cell. The electric field, E, is often seen as a constant.

2.2.3 Motivation for this work

The preliminary goal of the research performed in the research group is to obtain a better understanding of interface processes in hybrid organic/inorganic solar cells and use the gained knowledge to produce more efficient solar cells. The research group is divided into two groups; the research group at Colorado School of Mines is mainly working on how to deposit the active polymer into the interdigital ZnO nanorod structure and how to assembly it towards a solar cell. The research group at NTNU and SINTEF is working on how to understand and control the growth of ZnO nanorods by pulsed laser deposition (PLD).

The research group at Colorado School of Mines have been working on inserting P3HT into the interdigital ZnO nanostructures. One of the main problems has been the insertion of the polymer in between the nanostructures due to poor wetting conditions. This problem increases as the distance between the nanostructures decreases and treatment of the ZnO surface to increase the wetting condition is neccessary (e.g. OTES[4] [35]).

---

[4] OTES - octadecyltriethoxysilane

The PLD work carried out by the research group at NTNU and SINTEF has grown ZnO on sapphire and silicon. PLD is too expensive of a technique that will never be favorable in commercial solar cells. However, PLD is chosen since it has shown to be very well suited for growing high quality films and nanostructures with few defects [36]. This is very important for the purpose of creating a model system to undestand the polymer-ZnO interface of the HSC. Sapphire and silicon are also substrates that will never be utilized in commercial solar cells, but are good materials for nanostructuring (due to lattice parameters, high melting temperature, smooth surface etc.). They are therefore very useful to understand growth mechanisms and optimizing the process.

Chapter 3

Growth mechanisms and ZnO crystal structure

In order to create a controlled, ordered bulk heterojunction the growth mechanism of the metal oxide have to be understood. In this chapter, it is given an introduction to some of the most important things to take into consideration during the ZnO growth.

3.1 Growth mechanisms

During the ZnO nanostructure growth, a catalyst has been utilized. It will therefore be described in this chapter both the Vapor-Liquid-Solid (VLS) and Vapor-Solid (VS) growth mechanism. This catalyst is Au and it contributes in using the Au droplets as nucleation centers for the growth.

3.1.1 Vapor-Liquid-Solid (VLS) mechanism

A typical assumed growth mechanism for catalyst deposition of nanorods is the VLS mechanism which was first described by Wagner and Ellis in 1964 [37]. In figure 3.1(b) it can be seen that the Au metal functions as a catalyst for the ZnO growth. Generally, noble metals and transition metals like Cu, Ag, Pd, Fe, Co, Ni have been used as catalyst on silicon and sapphire substrates growing structures of Si, GaAs, ZnO and such [38, 39]. By these catalysts, Au is commonly used for ZnO nanorod growth by VLS mechanism [40].

At high temperature, when the Au droplets are in liquid state the VLS process starts. This happens as the Au catalyst droplet reacts with the Zn which is present, see figure 3.1(b). These two elements create an alloy according to the binary phase diagram, see figure 3.1(a). This alloy is in liquid phase as long as the temperature is held above the eutectic temperature. It should be kept in mind that this diagram is only used for guiding, and since a very thin layer of Au is present the melting point is much lower (see figure 3.3(b)) and the phase diagram far more complicated. Reducing the temperature below the eutectic temperature of Au-Zn or removing the reactant (Zn) from the liquid droplet will terminate the VLS process. The liquid droplet is a preferential spot for the gas phase reactant. When this droplet becomes supersaturated it serves as a nucleation site for the crystallization and ZnO precipitate underneath the droplet. Most likely it is the Zn which precipitates and get oxidized by the oxygen atoms. The presence of ambient oxygen during growth aids for the depositing of oxides. In addition, the presence of

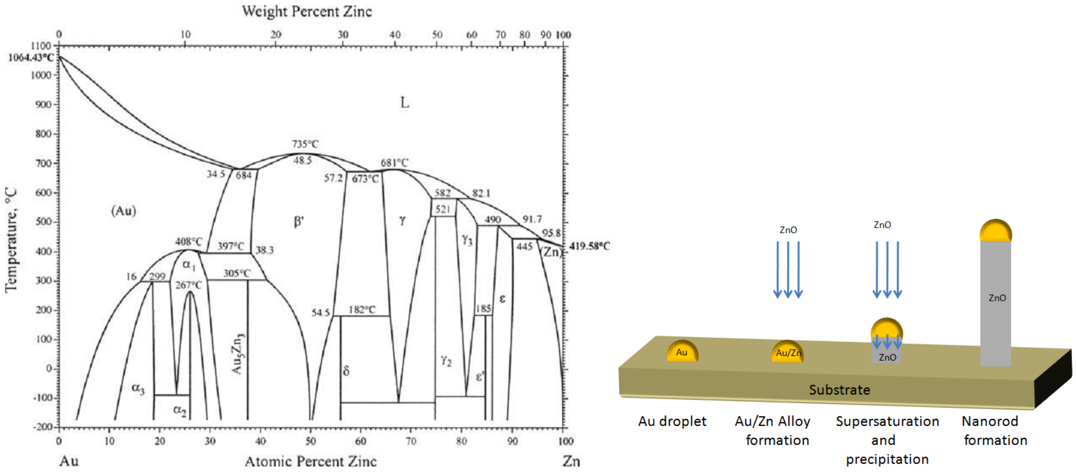

(a) (b)

Figure 3.1: (a) Binary phase diagram of Au-Zn, source:[41]. (b) Vapour-Liquid-Solid (VLS) mechanism.

oxygen also aids the growth by reducing oxygen vacancies during the growth. The VLS growth mechanism is usually determined whether there is a solid Au droplet present at the top of the grown structure.

The nanosized Au droplets used as catalyst can be formed in many ways. The easiest and most common way is to deposit a thin Au film and anneal it at high temperature.

Formation of Au droplets

The formation of Au droplets from thin film at elevated temperature is a well-known phenomena and is commonly used as a catalyst for the vapor liquid solid (VLS) growth of e.g. GaAs nanowires on Si substrate, ZnO nanowires on $Al_{0.5}Ga_{0.5}N$ substrate, ZnO nanostructures on Si substrate [42, 43, 44]. The Au droplet formation on i.e. GaAs is well understood and is explained by an Au-Ga liquid alloy due to the binary phase diagram. Au droplets on sapphire substrate is a less understood phenomena. One theory is droplet nucleation and Ostwald Ripening as shown in figure 3.2. At low annealing temperature the thin film is nucleating. The Au atoms are contracted and Au accumulation occurs, figure 3.2(a) and (b). At higher temperature the influence of Ostwald ripening may enlarge the biggest droplets and reduce (and remove) the smallest [45]. Ostwald ripening is a phenomenon in solid or liquid solutions where large particles will draw material out of smaller particles. Large particles grow, while small particles shrink, see figure 3.2(c).

Eutectic point is the point at which the liquid phase borders directly on the solid phase, as seen in the binary phase diagram in figure 3.3(a). Another more far-fetched theory could be that the droplets are formed when the temperature rises above the Au-Al[1] eutectic point, creating Au-Al alloy droplets on the wafer surface. Mixing Au with Al greatly reduces the melting temperature of the alloy as compared to the alloy constituents, according to the binary phase diagram in figure 3.3(a). The melting point varies according to the alloy of Al_xAu_{1-x}. The melting point of Al_2O_3 is above 2030°C, although the melting point of pure, bulk Al is

---

[1] Aluminium is the metal part in sapphire, Al_2O_3

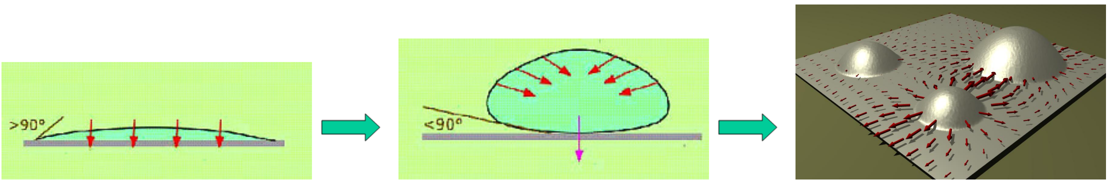

(a) (b) (c)

Figure 3.2: Au droplet formation proposal. Au thin film nucleates, (a), and form droplets, (b). Au droplets formation due to Ostwald ripening (c). Source: [45]

determined to be 660°C. The high melting point of Al_2O_3 is due to the tightly bound Al and O atoms. In situ XRD measurements of a 25nm thick Au film on c-plane sapphire was investigated by Margenthaler et al. in 2008 [46]. They observed neither interaction of gold with the substrate material nor an incorporation of Al. During the annealing they observed a more intense (111) Au diffraction peak with reduced FWHM. This could be due to an azimuthal alignment of the gold on the sapphire substrate.

The melting point of bulk Au material is 1064°C. This seems to decrease as the bulk material moves toward thin film, see figure 3.3(b). Buffat et al. predicted that the melting point of a pure Au droplets less than 20 nm is much lower than 700°C. The formation of Au or Au-Al droplets at an annealing temperature around 700°C is commonly observed.

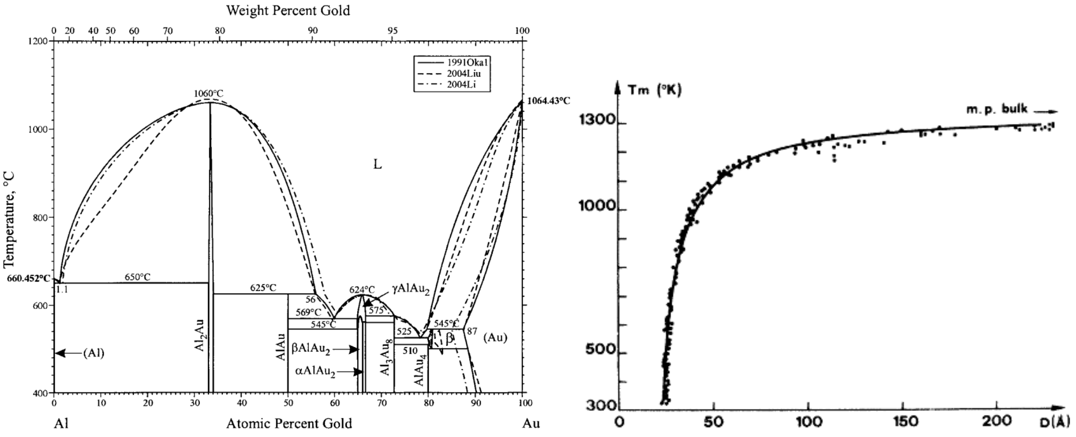

(a) (b)

Figure 3.3: (a) Binary phase diagram of Au-Al reported by [1991Oka1], [2004Liu], and [2004Li]. Source:[47]. (b) Experimental and theoretical values of the melting point temperature of Au particles. Solid line results from least-squares fit using all of the experimental points. Source:[48].

3.1.2 VS thin film growth mechanism

Another form of growth is referred to as vapor–solid (VS) growth and occurs without catalyst present. This is more like a depostion of thin film. This mechanism was proposed when ZnO nanostructures were grown without any form of catalyst [49].

Surface free energy

In thin film growth, the structural growth is normally explained by the surface free energy. In solid state physics, the atoms in the bulk of a material possess a more energetically favorable position than atoms at the surface. The surface energy density and surface tension has SI-units J/m^2 and N/m, respectively. These are equivalent in liquid since it is not more energetically favorable for atoms to align in some sort of lattice structure in liquid phase. A minimalization of the surface free energy is the driving force in order to have good structural growth. The surface free energy (G) increases due to the presence of the thin film, see equation 3.1. Here γ is the surface free energy for interface of film-air (γ_f), substrate-air (γ_s), film-substrate (γ_i) and the epitaxial energy gain (γ_e) [6].

$$G = (\gamma_f - \gamma_s) + \gamma_i - \gamma_e \tag{3.1}$$

The thin film will grow in the direction where it obtains the minimum surface free energy, G$_{min}$. This is the case for epitaxial thin-film growth where γ_e is predominant, otherwise γ_f (film-air) is predominant. The lowest surface energy for ZnO (γ_f) is the c-plane, (0001), and this is in general found to be the preferred texture for ZnO films [50, 46].

In order to fullfill G$_{min}$ adatoms (deposited atoms) align in different ways creating different kinds of growth modes. This is the case from a thermodynamic perspective where the growth is close to equilibrium. This means that the adatoms can move freely, with no interactive forces or external forces. In general, there are four types of film growth. Namely Frank-Van der Merwe, Volmer-Weber, Stranski-Krastanov and step-and-flow, see figure 3.4. In the layer by layer growth, (figure 3.4(a)) there is a very strong bonding between the thin film and the substrate, causing the surface free energy to be less than the bare substrate ($\gamma_f + \gamma_i < \gamma_s$). If there is no bonding between the film and the substrate there arise no energetically favorable places for the adatoms. The adatoms will then start to nucleate with each other and island formation occur, figure 3.4(b). This can also occur when the mobility of the adatoms are to low. In figure 3.4(c) the Stranski-Krastanov growth is given. This only occurs for heteroepitaxial growth and origins from the strain introduced to the film as a result of the mismatch between the substrate and the grown film. This starts out at a layer by layer growth, but as it exceeds a critical growth height it gets more energetically favorable to introduce dislocations due to the built in stress. The last example is the step-and-flow growth which origins as a result of the adatoms which diffuses on the terrace steps of a surface, figure 3.4(d). It finds an energetically favorable spot at the terrace step and nucleates there with either the substrate or the thin film. These growth types were mainly derived from [51].

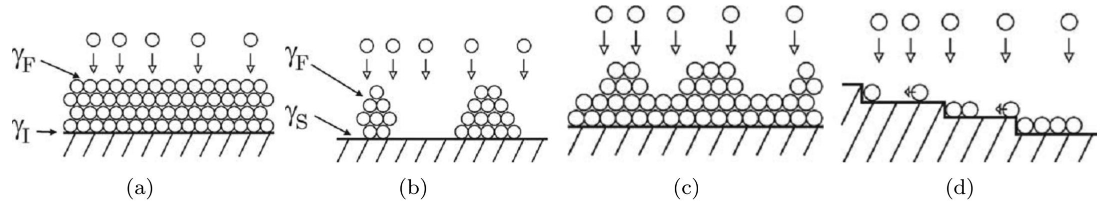

(a) (b) (c) (d)

Figure 3.4: Four VS thin film growth modes: (a) Frank-Van der Merwe (layer-by-layer), (b) Volmer-Weber (island), (c) Stranski-Krastanov, (d) step-and-flow. Source: [51].

3.2 ZnO structure

Zinc Oxide has a hexagonal wurtzite structure with lattice parameters a=0.3296 and c=0.52065nm. It is well known that ZnO is a polar crystal, and the structure of ZnO can be described as an alternating Zn and O planes whose positive polar plane is Zn rich and the negative polar plane is rich in O, see figure 3.5 [52]. This alternating stacking of Zn and O planes is causing a net dipole momentum, which further causes the surface free energy to diverge.

The different surface structure of ZnO is causing an anisotropic growth. Normally, under thermodynamic equilibrium condition, facets with higher surface energy have poor growth, while facets with low surface energy have a fast growth direction. In ZnO, the highest growth rate is along the (0001) direction, while the large facets are usually $(01\bar{1}0)$ and $(2\bar{1}\bar{1}0)$ [53]. The preferred growth directions for ZnO were first found by Laudise and Ballman and showed that $(0001) > (10\bar{1}1) > (10\bar{1}0)$, as seen in figure 3.5(a) [54]. By controlling the growth kinetics it should be possible to form the structure which is desirable.

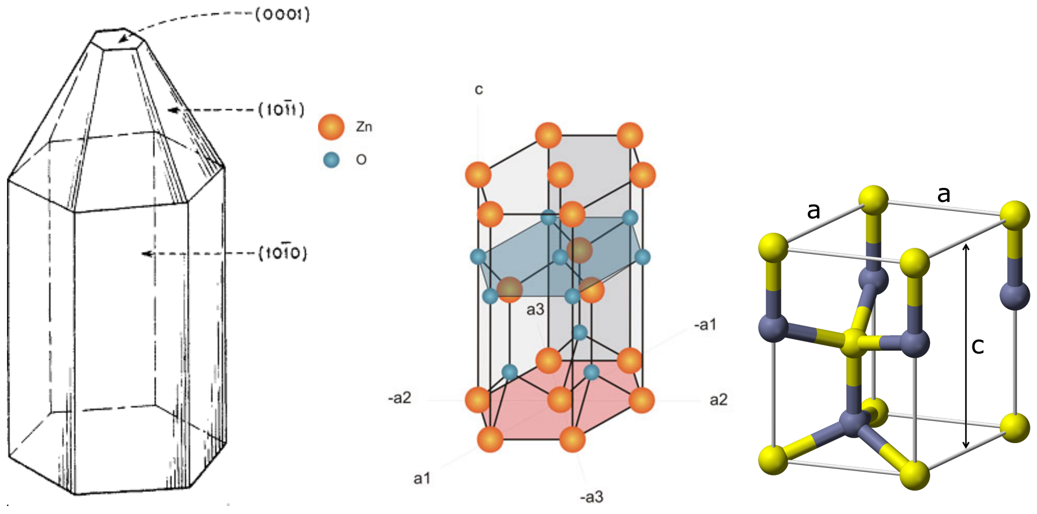

(a) (b) (c)

Figure 3.5: (a) Growth facets of ZnO, Source:[54]. (b) Hexagonal Zink Oxide. (c) Wurtzite Zink Oxide with lattice parameters a=0.3296 and c=0.52065nm. The yellow and grey spheres represents the Zn and O atoms, respectively.

Chapter 4

Characterization methods

Since we look at structures at nanometer scale, optical microscopy can not be used. The reason being the spatial resolution is limited mainly by the wavelength of light, λ, as seen in equation 4.1. Also the highest practical aperture, NA, equal to around 0.95 leads to the lowest obtainable distance, d, and is around 200nm for optical microscopy. In order to get images with resolution down to nm, electrons can be used instead of light as for the scanning electron microscope (SEM), section 4.1. Objects at atomic scale can be viewed with SEM using electrons with short wavelength (e.g. 0.122nm for 100eV electrons versus about 550nm for light) [55]. Another method of imaging surfaces at atomic scale is to measure the attraction forces between an atomic small probe and the sample in a so called atomic force microscope (AFM), section 4.2. A third method is to emit an X-ray wave, which interfere with the crystal lattice atoms. This imaging method, called XRD, is described in section 4.3. A short introduction to these imaging techniques is given in the sections below.

$$d = \frac{\lambda}{2 \cdot NA} \tag{4.1}$$

4.1 SEM

The earliest known work describing the concept of SEM, and also the first SEM image was obtained by Max Knoll in 1935 [56]. The SEM has electromagnets instead of lenses and has therefore a better control in the degree of magnification. The microscope consists of an electron beam, which emit electrons at an acceleration voltage between 0.1-20kV. The system is in UHV chamber, mainly because of three things. 1) High pressure would have made the electrons collide with particles in air and prevented them to reach the sample. 2) The filament (electron emitter) would oxidize rapidly if it is used in air (like a light bulb). 3) If gas molecules were ambient in the chamber it could react with the sample and create thin films on the surface, which would have made bad images. The electrons are accelerated towards the anode where the electrons are directed in one beam towards the magnetic lens as seen in figure 4.1(b). When the electrons are approaching the sample, they are focused into a narrow beam with a cylindrical magnetic objective lens often combined with electrostatic focusing elements [55]. As the incoming beam of electrons is hitting the sample electrons and photons are emitted or transmitted out from the sample. Secondary electrons, backscattered electrons, X-rays, auger electrons and cathodoluminescence (CL) have to be collected by different kinds of detectors to create an image to be viewed on an external monitor, figure 4.1(c).

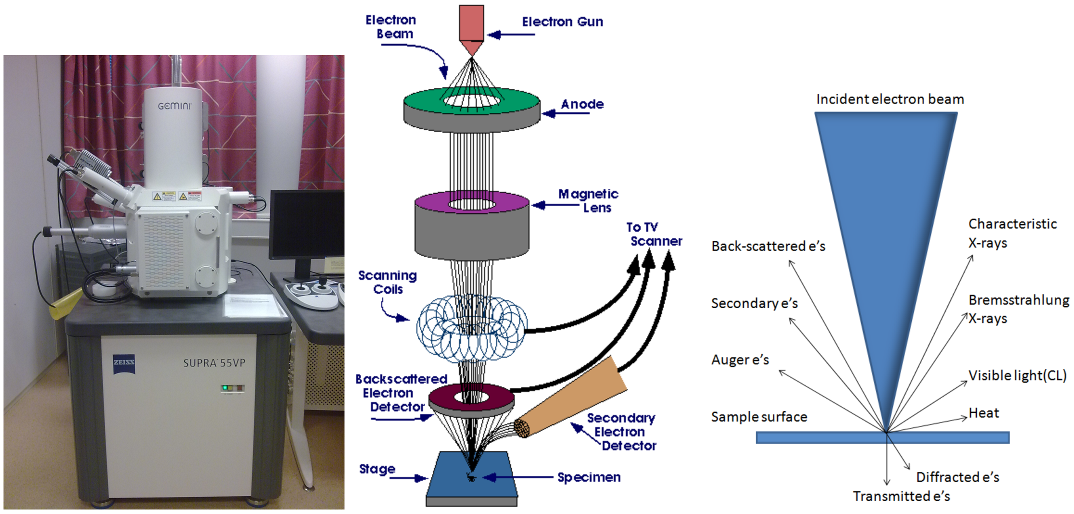

(a) (b) (c)

Figure 4.1: (a) Zeiss Supra 55 VP, LVFe-SEM. (b) Drawing of how the SEM works. Source:[55]. (c) Electron beam interaction on the surface. Emitted and transmitted electrons and photons are used for surface imaging and characterization.

4.1.1 SE

In this study, mainly the secondary electrons (SE) have been used for surface imaging. These detected electrons are numerous and with low energy (below 50eV) [57]. SE (in addition to Auger electrons) create images with the best image resolution since these electrons are emitted from small volumes near the surface of the sample. The spatial resolution of SE imaging (smallest feature detectable) is in the order of 3-5nm [55]. In addition, is the SE a non-destructive and non-contact imaging method. SE are those electrons which are knocked out of their orbits around an atom by an incident electron from the beam. SEM gives best resolution images on metals and conducting materials, since these materials emit the most signals. A method of increasing the conductivity of insulators and semiconductors (e.g. sapphire) is to use a conducting tape (e.g. Cu) to fasten the samples onto the substrate holder. This kind of special care was used during experiments in order to minimize this type of charging effect. An alternative method is to coat the insulating samples with conductive films prior to imaging. This is mostly avoided since it affects the sample surface.

4.1.2 EDX

Energy-dispersive spectrometer (EDX) is a complementary characterization tool to the SEM, and is commonly found on most SEM today. EDX detects and measures the X-rays emitted from the sample. The electron beam excites an electron from an inner shell and an electron hole is created where the ejected electron was. During relaxation an electron from a higher energy shell takes the place of the electron hole. The energy difference between the outer shell and inner shell is released in the form of an X-ray. Each element has a unique form of X-ray spectrum, which the EDX can detect and identify within few minutes. It is a powerful analytical technique in order to determine contamination as well as structural elements imaged by SE. It is important to use high electron beam voltage (up to 20keV) when characterizing the sample with EDX. This is to have enough energy to excite the electrons from different shells for different kinds of elements. I.e. to detect Au spectrum on EDX, an electron source of at least 9.22keV have to be impressed, since this is the energy needed to remove an electron from the L-shell of the Au atom.

4.2 AFM

Atomic force microscopy (also called scanning force microscopy, SFM) is a relatively new technology, which was first demonstrated in 1986 [58]. The laser is aligned to the cantilever tip which reflects the laser beam onto a photodiode detector as shown in figure 4.2(b). Beneath the cantilever there is a very sharp tip with a nominal tip radius of around 5nm. A sample-tip distance lower than $\sim$ 10nm the force between the tip and the surface atoms increases and decreases as the distance gets smaller and larger, respectively. To approach the sample down to the working distance, PC equipment is used to bring the tip near the sample while measuring atomic forces. A highly sensitive piezoelectric drive unit is used to adjust the tip further apart or closer to the sample by adjusting the impressed voltage over the piezoelectric element. The instrument used for processing data from the AFM was a Nanoscope V (Digital Instrument), while the computer software used was Veeco Nanoscope 7.20. There are three primary modes of measuring the surface topography (3-Dimention) by AFM:

1. Tapping Mode (TM) - Constant oscillation amplitude, measuring the RMS of amplitude signal
2. Contact mode (CM) - Constant force, measuring the deflection from the cantilever
3. Non-contact mode - Cantilever is oscillating above resonant frequency. Long range forces decrease the resonant frequency and cause the amplitude of the oscillation to decrease, which is measured

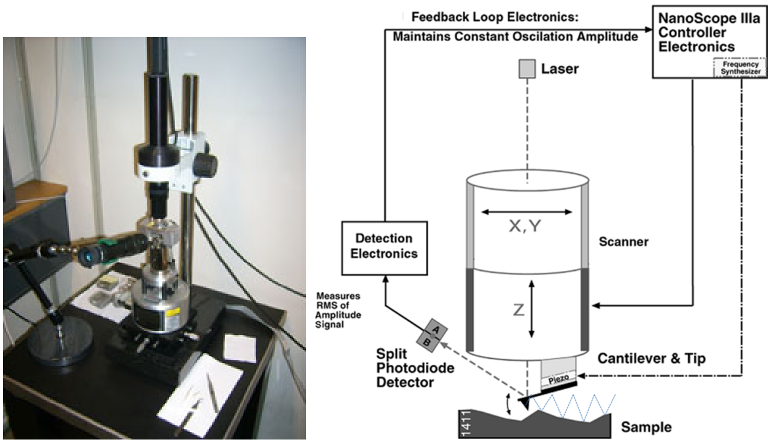

(a) (b)

Figure 4.2: (a) AFM. (b) Drawing of how the AFM-TM works. Source:[59].

In this thesis, AFM-TM has been chosen despite the fact that TM can provide lateral resolution on most samples down to 1-5nm, contrary to the CM providing ”atomic resolution”. The reason we chose the AFM-TM was because of easy access to a TM optimized AFM and a fast image taking procedure. Another advantage of the AFM-TM is good image capturing of non-conductive samples.

The cantilever in TM is oscillating approximately at the resonant frequency and the tip lightly ”taps” on the sample surface. The amplitude below the equilibrium point of the trajectory changes according to the surface topography, see figure 4.2(b). The feedback loop maintains constant oscillating amplitude by maintaining a constant RMS of the oscillation signal acquired by the split photodiode detector [59]. The z-value at each (x,y) coordinates of the topography are saved from the value obtained from the photodiode detector. A silicon tip with specification given in table 4.1 was used.

Spring Constant (k)	20 - 100 N/m
Resonant Frequency	200 - 400 kHz
Nominal Tip Radius of Curvature	5 - 10nm
Cantilever Length	125μm
Cantilever Configuration	Single Beam

Table 4.1: Tapping Mode Etched Silicon Probe (TESP) characteristics.

4.2.1 Limitations

There are mainly two limitations due to the cantilever tip, hence the radius curvature and the tip sidewall angle. The tip should be sharp with a small sidewall angle to obtain high resolution images. Image artifacts due to the cantilever tip are often a problem when the tip gets worn. If the tip becomes dull due to rough treatment small structures may be difficult to depict, i.e. small droplets as seen in figure 4.3. Another image artifact occurs when debris sticks to the tip during an image scan. This can create image distortion, and also contaminate the surface as the debris fall off.

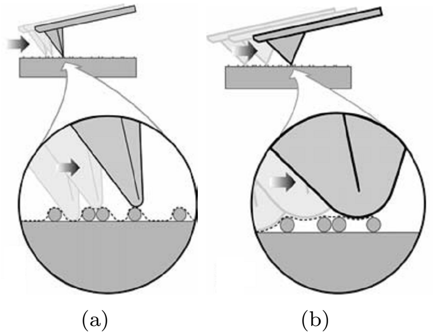

(a) (b)

Figure 4.3: Tip artifact causes resolution limitations. (a) Sharp tip with small sidewall angle. (b) Dull tip with large sidewall angle. Source:[59].

4.3 XRD

X-Ray Diffraction (XRD) is a non-destructive analytical technique which reveals information about the structural arrangement, chemical composition and physical properties of materials.

A material crystal consists of a regular array of atoms. When waves (with wavelength on the same order as the distance between the crystal atoms) enter a crystal they are scattered in all directions by the crystal atoms. These scattered waves can in some directions create constructive interference and in other directions create destructive interference. This scattering of waves is seen as elastic scattering, in which the energy of the X-ray is not changed on reflection [60]. This scattering of incident waves and interference in different direction is generally known as crystal diffraction.

The XRD emits a collimated X-ray beam incident to a sample surface, while the diffraction pattern is sensed by the detector, as seen in figure 4.4. When a known material is investigated the diffraction gives information of the crystal structures and in thin film growth this is important in order to determine the preferred growth direction. The constructive interference origin in different directions as if the waves where reflected by a family of atoms or planes [61]. These crystal planes are listed in tables for each material, where the reflected angle denotes the crystal plane orientation of the material. The commonly known Bragg diffraction law is used to determine the constructive interference of the waves:

$$2d_{hkl}\sin\Theta_{hkl} = n\lambda_{XRD} \tag{4.2}$$

,where d_{hkl} is the spacing of parallel atomic planes, Θ_{hkl} is the angle between the crystal planes and the incident beam. λ_{XRD} is the wavelength of the incident beam. n is an integer known as the order of diffraction. It should be noted that the (hkl) indicates the Miller indices of the crystal plane. More literature of XRD, Miller indices and reciprocal space is found in [60, 61].

In this work an AXS D8 X-ray diffractometer with wavelength of $\lambda_{XRD} = 1.5406\mathring{A}$ has been used.

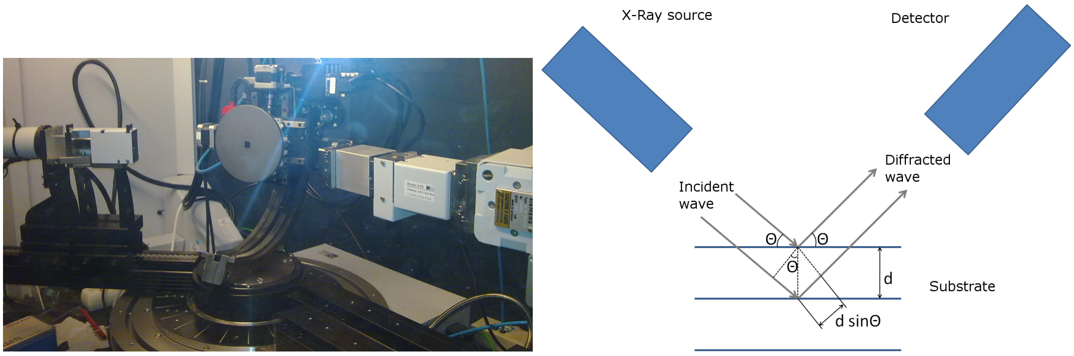

(a) (b)

Figure 4.4: (a) Picture of AXS D8 X-ray diffractometer. (b) Drawing of how the XRD works. The drawing is tilted 90°compared to the picture in (a).

Chapter 5

Experimental Procedure

The procedure of ZnO nanostructures growth was mainly done in four steps, without the characterization step described in chapter 4. The four steps are:

1. Cleaning procedure
2. Annealing substrate
3. Evaporation of thin Au film
4. PLD growth of ZnO

Prior to cleaning, the wafer was cut into small 1cm^2 samples by a wafer cleaver. For good results and reproducibility it is of importance to have the same procedure and experimental setup every time and only change one parameter at the time to investigate the influence of each parameter. Since a lot of the experimental work is influenced by the person doing it, it takes time and practice to develop good procedures which are reproducible. In the next sections, the procedure used during this work has been explained in detail.

5.1 Cleaning Procedure

A standard acetone-ethanol-nitrogen method is used to clean the samples. The samples were first cleaned by acetone in an ultrasonic bath for 10 minutes. Acetone is used since it is highly miscible with water and almost all organic solvents. 10 minutes was chosen since this is the common time interval used in literature and most of the contamination is dissolved. Immediately afterwards, a lot of ethanol were squirted on to the sample, covering the surface. Since the ethanol quickly evaporates, nitrogen is used to blow the surface dry and to avoid drying stains.

5.2 Annealing

The annealing was performed in a high temperature furnace at 1000°C, 1200°C and 1400°C with high oxygen flow, O_2. The oxygen flow was not measured due to the absent of precise pressure gauges. A high flow was chosen to be sure that the Al_2O_3 material was fully oxidized and no defects were formed in the structure. The samples were warmed up at a rate of 5°C/min and stayed at this temperature for 1h. The cooling was set to 5°C/min, but since the furnace could not cool at this high ramping temperature a lower rate actually occured.

5.3 Evaporation

Evaporation of an Au thin film was performed with an e-beam evaporator[1]. The cleaned samples were clamped onto an 8” wafer with paper clips, placed up-side-down on a circular holder and inserted into the loading chamber. The loading chamber was pumped down to a pressure of approximately $5 \cdot 10^{-5}$mbar before the vent valve was open and the wafer holder was loaded into the main chamber with a loading arm. The Au metal was chosen, and since only a very thin layer of approximately 1nm should be evaporated on, the shutter in front of the samples was removed instantly. This was done so that the quartz crystal should detect the evaporated Au atoms as soon as the current was adjusted high enough. The manner of operation of the e-beam evaporated is seen in figure 5.1. The electron source emits electrons with a high voltage anode. The electrons are influenced of a magnetic field which bends the beam about 270° towards the Au source and melts the surface. The molten Au source evaporates and diffuses towards the samples where it condenses and forms a thin film. Since the heating is localized to the source only, the temperature and pressure in the chamber is held low. This causes the Au particles to diffuse in a straight forward line towards the sample. During the manually deposition the electron beam was centered to the Au source melting the entire surface. The current was gradually increased to around 50mA before the quartz crystal started detecting a deposition rate of 0.1Å/s. In order to avoid electromagnetic fluctuations causing some extra layer of Au to be deposited, the current source was turned off a couple of seconds before the desirable thickness was reached. Also the shutter was closed some seconds after the deposition had stopped.

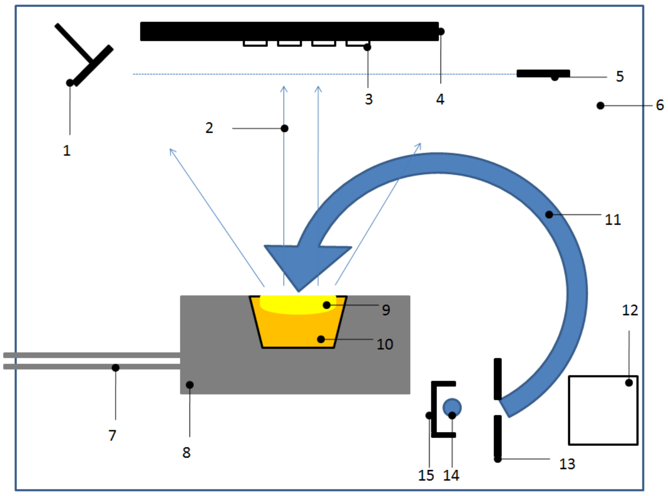

1	Quartz Crystal	9	Molten Au
2	Diffusion of Au particles	10	Au Source
3	Sample	11	Electron beam (270°bent)
4	Wafer	12	Magnet
5	Shutter	13	Anode
6	Vacuum Chamber	14	Electron source
7	Water cooling lines	15	Shield
8	Water cooled copper crucible		

Figure 5.1: Schematic of the e-beam evaporator

---

[1] Electron Beam Evaporator a subcategory of Physical Vapor Deposition (PVD)

5.4 PLD system

PLD has in the last 20 years emerged as one of the most popular and intrinsically simple depositing techniques for research purposes due to the inherent versatile, flexibility, amenability and speed of process [6]. This makes it good for controlled growth of a large variety of nanostructured materials for research environment [62]. It has been shown experimentally that ZnO deposited by 248nm lasers (which is used in this work) exhibited a far superior morphology than films deposited with 532- or 1064-nm lasers, regardless of the experimental conditions [6].

5.4.1 Principle of the PLD

The PLD system owned by NTNU/SINTEF consists mainly of a pulsed KrF excimer laser[2] and a UHV chamber constructed by Twente Solid State Technology (TSST). The laser pathway is illustrated in figure 5.2. The laser beam is total reflected through some mirrors towards the aperture slit creating a rectangular shaped cross section. The laser beam is further adjusted by a beam splitter and an attenuation lens inside a closed box. Afterwards a lens is focusing the beam through a UV transparent view window onto the target inside the UHV chamber. The target is mounted on a raster scanned target carousel, which can remotely be controlled in (x,y,z)-direction. In addition, multiple targets can be selected by rotationg the carousel. In this growth experiment only ZnO was used as the target, but in practice, together five targets can be inserted into the UHV chamber. As the high power laser pulses hit the target, the target surface evaporates and creates a plasma plume normal to the target surface (see figure 5.3). The plume expands towards the samples surface, where the ablated species condense and form a thin layer of atoms. The distance from the target to the sample is essential.

The PLD growth is mainly controlled by 5 parameters: Laser frequency, laser density on target, target-substrate distance, temperature and pressure. In the following experiments these parameters were held constant in order to investigate the influence on substrate annealing, see table 5.1. In order to make reproducible results these parameters were tried to be held constant through focusing on clean and proper sample preparation, several temperature readings and laser power readings as explained in the following sections.

Parameter	value
Duration of deposition	30 min
Laser pulse repetition rate	10 Hz
Fluence on target	1.33 J/cm^2
Distance target-substrate	45 mm

Table 5.1: Constant parameters during PLD growth

5.4.2 Preparation

The sample is glued to the sample holder using a silver paste. The silver paste is uniformly distributed underneath the sample for good heat conduction. Paste which unintentionally oozes out from underneath is carefully removed. This is done to minimize any unwanted Ag evaporation effects during the PLD growth and thus improving the reproducibility of the growth. The sample holder is put on a hot plate and baked at 150°C for 20 minutes to coagulate the paste so the sample sticks to the holder. Afterwards the sample holder is inserted right away into the PLD

---

[2] 248nm, LPXPro 210 from Lambda Physik

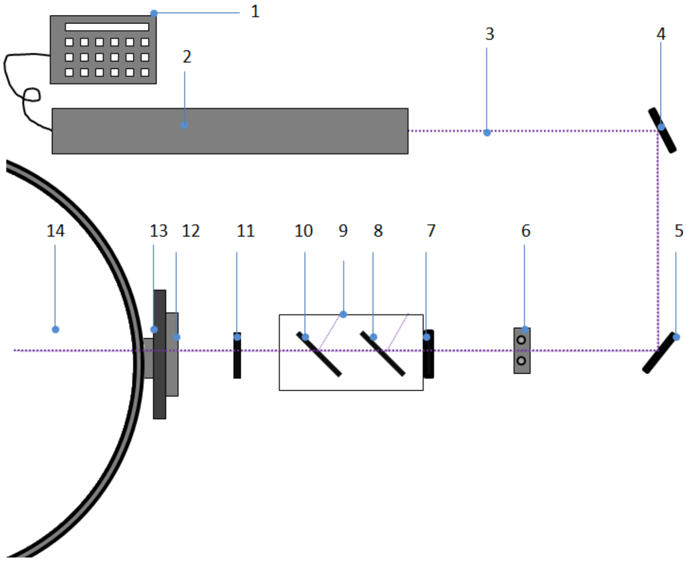

1	Laser control panel	8	Attenuator plate
2	KrF 248nm laser	9	Closed box with absorber
3	Pulsed laser beam	10	Compensator plate
4	Mirror	11	Focusing lens
5	Mirror	12	Viewing window
6	Aperture slit	13	Internal silica disk
7	Shutter	14	Vacuum chamber

Figure 5.2: Schematic of the laser path

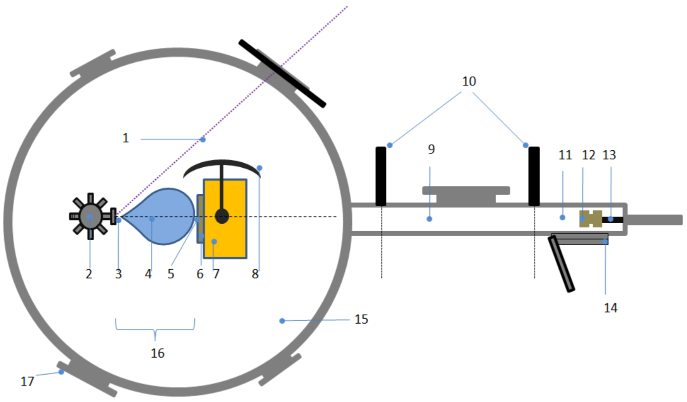

1	Laser Beam	10	Shutter
2	Target carousel	11	Loading Chamber
3	Target	12	Sample Holder
4	Plasma Plume	13	Loading arm
5	Sample	14	Door to loading chamber
6	Sample Holder	15	Main Chamber
7	Heater	16	Target-Substrate Distance
8	Shield	17	Viewing Window
9	Ion Milliong Chamber		

Figure 5.3: Schematic of the PLD chamber

main chamber using a loading arm as shown in figure 5.3. Gas composition and pressure is chosen by a computer controlled software as the sample is starting to warm up at a ramping rate of 10°C/min. The ramping rate is manually increased from 10 to 15°C/min after the temperature is overshoot at approximately 300°C. Ramping the temperature in the PLD chamber makes the Au thin film anneal and droplets are formed.

The target was polished by sandpaper after every second deposition and mounted to the target carousel holder. The target consisted of hot pressed and sintered ZnO manufactured by American Elements with a purity of 99.999%. Pre-ablation is done by covering the sample by the shield, and let the laser remove the surface layer of the ZnO target. Pre-ablation was performed by scanning the surface at the same position as ablation twice. The duration was approximately 10 minutes. This is to remove the first surface layer of the target, in order to remove surface contamination to get as clean surface as possible. This preparation step has been carried on in a very reproducible way.

5.4.3 Laser power

Since there are two UHV chambers in the laboratory, it is important to change the laser path to the correct chamber. A mirror at position $x = -54$mm is selecting the SINTEF UHV which is used during the growth. The adjustable aperture decides the cross-section of the laser beam which passes through the slit. Maximum aperture slit height (h_a) and aperture slit width (w_a) is equal to 28nm. The laser effect is regulated with an attenuator plate as seen in figure 5.2. When the laser pathway is correct, the laser effect is measured with two different power meter in front of the UHV chamber. Also the voltage impressed on the laser, laser pulse energy and laser pressure is measured on the laser control panel. The attenuator is kept constant at 850 which is the maximum attenuation. ZnO can contaminate the UHV chamber, and since ZnO blocks the UV (laser) light, contamination on the entrance window can cause a decrease in laser power onto the target. The laser power was measured right before the entrance window of the UHV chamber and also right after the entrance window (inside the UHV chamber). The entrance window consists of an ”intelligent window” which provides a better control of the ZnO contamination, see figure 5.2. This ”intelligent window” consists of an internal silica disk which can rotate so that a non contaminated area is faced. This is done without opening the chamber and a better control of the laser power onto the substrate is achieved. The energy density on the target was found according the formula given in equation 5.1.

$$\Psi = \frac{P_{laser}}{\nu A_{spot}} \tag{5.1}$$

,where Ψ is the energy density [J/cm^2], P_{laser} is the laser power measured outside the chamber [W] (and checked inside the chamber), ν is the pulse frequency [Hz] and A_{spot} is the area of the spot size on the target [cm^2]

5.4.4 Temperature

The temperature is a very important parameter in the PLD growth. In our case, the temperature mainly affect the growth in three different ways; 1) the size of the catalyst droplets, 2) deterimining the amount of vapor which wants to condense onto the surface, 3) the surface mobility of the deposited material on the sample [63]. The temperature is set in the computer software. This is regulated by the TSST software by increasing the current through a platinum-rhodium thread which is spun around a ceramic plate as shown in figure 5.4. When the set point temperature is attained the current and voltage value on the TSST system is noted. After 5 minutes, manual measurements of the temperature on three places on the sample holder are carried out with an optical pyrometer at a wavelength of 1.5μm. During this work, one optical pyrometer with the same emissivity value have been used. The emissivity depends on the material that is measured and in the case of sapphire there is a pretty large range of values. In that case, a value of silicon (0.7) was chosen. The emissivity value for sapphire is lower and the correct temperature should therefore in each case be higher. The temperature measurements were performed in order to investigate the temperature deviation from experiment to experiment, and also if the Ag paste had any notable influence on the thermal contact. The sample temperature were not measured to be equal to the set point temperature, while the temperature measured above and below the sample showed a temperature above the set point temperature. This may be due to the material and the emissivity of the pyrometer. The sample holder temperature was rather constant from experiment to experiment, while the sample temperature varied. This can indicate that the heater obtains a constant temperature, while the thermal contact from the sample holder to the sample may be a small limitation. Fastening the sample with Ag paste may be a step to improve. Despite the small temperature deviation the results are believed to be reproducible.

5.4.5 Other parameters

The target-substrate distance was held constantly at 45mm at a pressure of 0.5mbar with Argon and Oxygen ambient. The pressure and gas flow can very well be controlled by the TSST system, and was not investigated any further during this work. The pressure influences both the deposition rate and the kinetic energy of the ablated target atoms. An increase in background pressure causes a decrease in the kinetic energy since there are more collisions to background gas

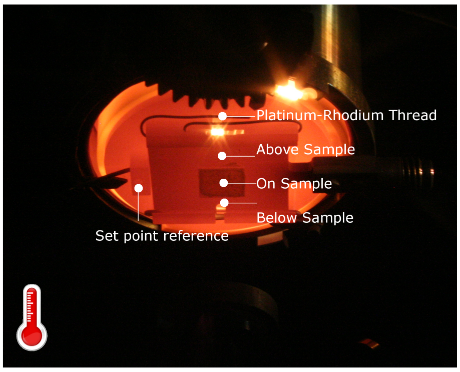

Figure 5.4: Temperature measurements inside UHV chamber.

molecules. The target-substrate distance should therefore be decreased as the pressure increases in order to stay in the plasma plume.

The laser frequency is defined as the number of laser pulses which hits the target per second. As the laser hits the target the surface ejects atom, increasing the frequency leading to an increase in deposited material.

5.5 Conclusion

There are many difficult steps in this experimental procedure as a consequence of operating with nanosized structures and layers. This means that special care has to be taken into consideration while handling the samples, i.e. contamination and procedure. The most crucial and critical procedures during this experimental work have been to: evaporate a known thickness of Au thin film layer, glue the sample onto the PLD holder and also to align the plasma plume from the target to the sample. This is believed to be performed satisfactory and in a reproducible way.

Chapter 6

Structural analysis of annealed Sapphire substrate

The annealing effects of the sapphire substrate surface have previously shown great influence on the film quality of the epitaxial growth of ZnO by metal organic chemical vapor deposition (MOCVD) [64]. It is therefore of interest to investigate the influence of the annealed substrate for the pulsed laser deposition (PLD) growth of nanostructured ZnO. The X-ray diffraction (XRD) and photoluminescence (PL) measurements for MOCVD showed that the optical properties were preferable for the 1200°C temperature in the contrary to un-annealed, 1000°and 1400°C. Explanations of these observations have been omitted, so further investigations are needed. Nevertheless, this behavior may not be the case for PLD.

6.1 Substrate material: sapphire

Formerly the (0001) cut sapphire has been the dominant cut plane of sapphire, in this research also the $(11\bar{2}0)$ cut sapphire, a-plane, will be taken into consideration. The a-plane and c-plane is aligned perpendicular to each other and possess different symmetry and surface potentials [65]. This means that it is favorable for atoms to align in one crystal plane rather than the other (i.e. (0001) and $(10\bar{1}2)$ planes have the lowest and second lowest surface energy, respectively [66]). This may have influence on the annealing results. Sapphire is not a substrate well suited for solar cells application anyway, but it is a good substrate to understand the growth mechanisms because it has the same crystal structure as ZnO. In addition, sapphire is very stable in air and at high temperatures and has a smooth surface, which is important in nanostructure growth.

Pure sapphire (α-Al_2O_3) is used as substrate in this work. Sapphire is an anisotropic, hexagonal crystal with chemical formula Al_2O_3. The hexagonal unit cell can be described with the two parameters $a = 4.759$Å and $c = 12.991$Å as given in figure 6.2 [67]. The sapphire was ordered in 2" wafers by two different suppliers, hence a-plane $(11\bar{2}0)$ from Shirley Epistone in China and c-plane (0001) from Valley Design in USA. The sapphire is cut in either a-plane or c-plane as seen in figure 6.1, and then the upper side is polished into a smoother surface.

6.2 Results and discussion

The as-polished substrate surface was annealed at different temperatures to achieve the best atomically flat surface. The procedure is described in section 5.2. Surface morphology was

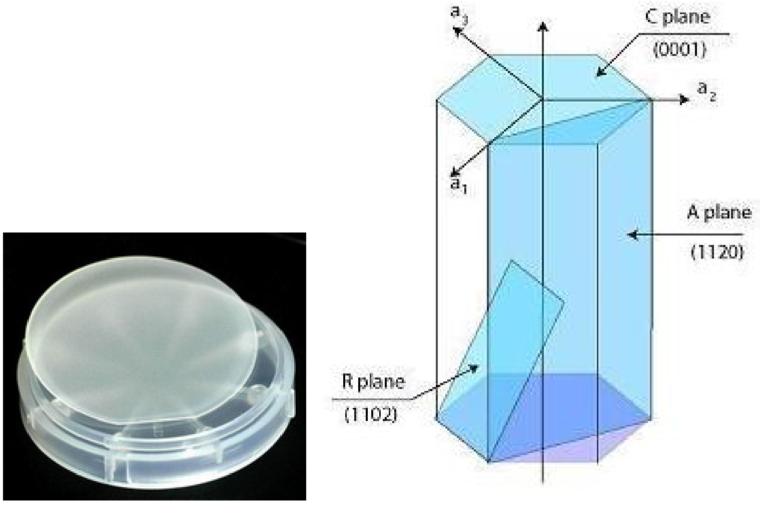

(a) (b)

Figure 6.1: Sapphire ordered from the manufacturer. (a) 2" Sapphire wafer. (b) Sapphire cut in a- and c-plane. Source:[68].

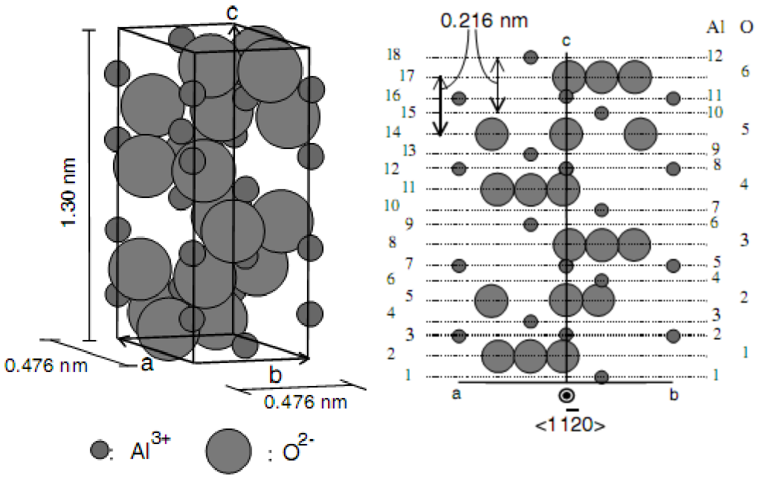

(a) (b)

Figure 6.2: Crystal structure of sapphire (α-Al$_2$O$_3$). (a) Atomic unit cell. The each number of each of the total of 18 layers is given on the left-hand side of (b), and the numbers of six O layers and twelve Al layers are shown on the right-hand side of (b). Source:[69].

observed by AFM described in section 4.2.

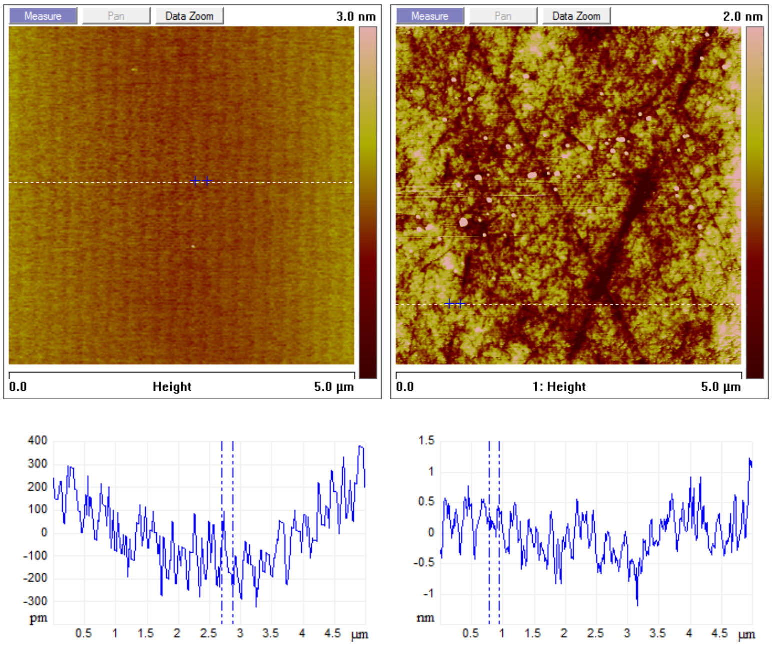

(a) (b)

Figure 6.3: Sapphire delivered from the manufacturer. (a) a-plane has a smooth surface in addition to a step-and-terrace formation. (b) c-plane has rougher surface, surface scratches and no terrace formation is seen.

6.2.1 Pre-Annealing

The as-delivered sample surface is seen by AFM in figure 6.3 for the a-plane and c-plane. As seen in figure 6.3(a) the a-plane has terrace structure with an approximate width of 0.2μm, while in the case of c-plane, just scratches and no terrace structure are observed, figure 6.3(b). From figure 6.3 the overall root-mean square (r.m.s.) roughness is 0.16nm in the case of a-plane sapphire and 0.46nm in the case of c-plane sapphire. In addition the maximum vertical distance from lowest to highest point of the a-plane is in the picture found to be 2.6 nm, while for c-plane; 8.64 nm. The scratches on the c-plane substrate are most likely due to the mechanical polishing of the surface caused by the manufacturer. In general, the polished surface of the sapphire (0001) and ($11\bar{2}0$) substrate possess a small deviation from the actual (0001) and ($11\bar{2}0$) face, where the deviation is usually referred to as the miss-cut angle. The miss-cut angle can be estimated from the terrace step height and the terrace width, since the terrace is the actual (0001) and ($11\bar{2}0$) face [70]. In figure 6.4 the miss-cut angle is depict as α. The terrace width is approximately a factor of 1000 larger than the terrace height, which leads to very small miss-cut angle found to be around 0.03±0.008°. The miss-cut angle to the ($11\bar{2}0$) orientations is given by the manufacturer to be ±0.25°, which shows that the miss-cut angle are within specifications. The miss-cut angle for c-plane is not known, and no angle can be calculated from the as-received c-plane samples. Most of the annealed samples are cut from the same wafer, and will therefore have the same miss-cut angle. The terrace height of a-plane is around 0.125nm, which is approximately c/12

(=0.108nm) of the atomic cell. This is less than one atomic step[1], see figure 6.2(b). The steps are clearly seen from the picture, but the transition is rather hard to measure due to the sub nanometer height difference. It is not known if the observed differences between a-plane and c-plane are due to different suppliers or if it is due to different intrinsic structure.

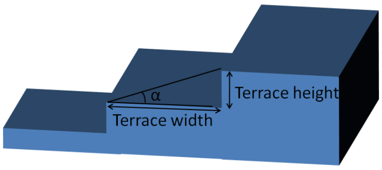

Figure 6.4: Sketch of the terrace formation and the miss-cut angle α. The terrace width is in order 1000 larger than the height.

6.2.2 Post-Annealing

To study the effects of the annealing on the sapphire surface, 3 annealing temperatures have been used 1000°C, 1200°C and 1400°C. In order to check the reproducibility of the process, several samples were used for each annealing temperature and each type of sapphire. Annealed samples are listed in table 6.1. For an overview of captured AFM picture, see table A.1.

Substrate orientation	Annealing temperature	Sample	number
a-plane	1000 °C	a10-a12	3
a-plane	1200 °C	a21-a25	5
a-plane	1400 °C	a31-a35	5
c-plane	1000 °C	c10-c12	3
c-plane	1200 °C	c21-c25	5
c-plane	1400 °C	c31-c35	5

Table 6.1: Samples used during the annealing characterization.

During annealing process at sufficiently high temperatures, atoms of the sapphire have enough kinetic energy to find the lowest energy state and form a very flat surface. It is also well known that in general, due to the miss-cut angle mentioned earlier, the substrate surface will form terraces during the annealing process.

Step and terrace for a- and c-plane

The transformation of the surface is given in figure 6.5 for the a-plane and in figure 6.6 for the c-plane. A series of all annealed surfaces are given in appendix A.

During the annealing process the terrace steps becomes sharper and the terrace width more defined. As clearly seen in figure 6.5(a) and (b) the steps are unfulfilled and there are ”cracks” in the steps like there are ”pieces” that are missing. These ”pieces” are most likely vacant atoms of Oxygen and Aluminum, which have not got enough thermal energy to diffuse and rearrange the lattice structure and found a place in the lattice where it possess the least amount of energy [71]. As seen in the next two pictures, figure 6.5(c) and (d), the steps now have almost vertical align steps to the terrace. In literature there are often found faceted terrace steps during annealing

---

[1] One atomic step - Height of around one Oxygen and 2 Aluminum atoms, $\sim$ 0.21nm or c/6 in atomic unit cell

[66, 69, 72]. This is usually explained by different surface energies of the different planes. Faceted steps are not observed here and can be due to the miss-cut orientation to the different surface energy planes.

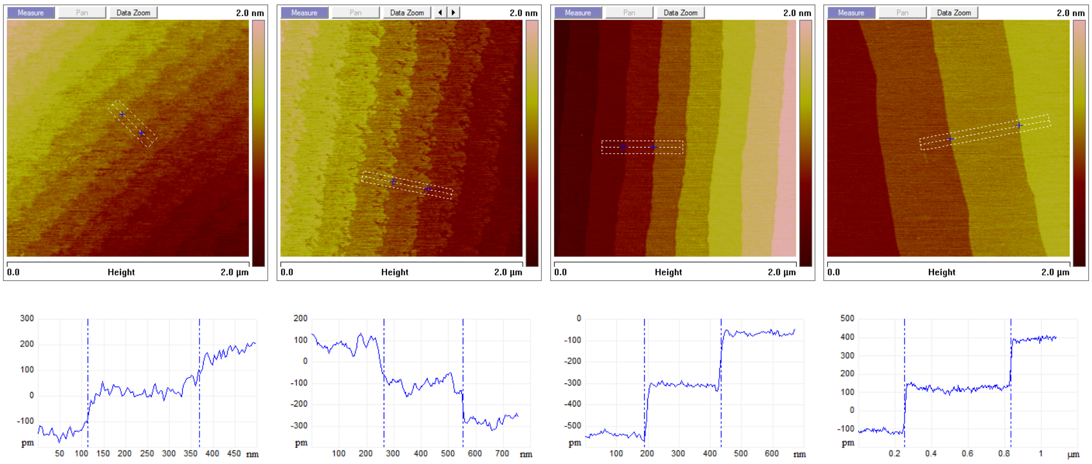

(a) unannelaled (b) 1000°C (c) 1200°C (d) 1400°C

Figure 6.5: a-plane: The formation of step-and-terrace morphology.

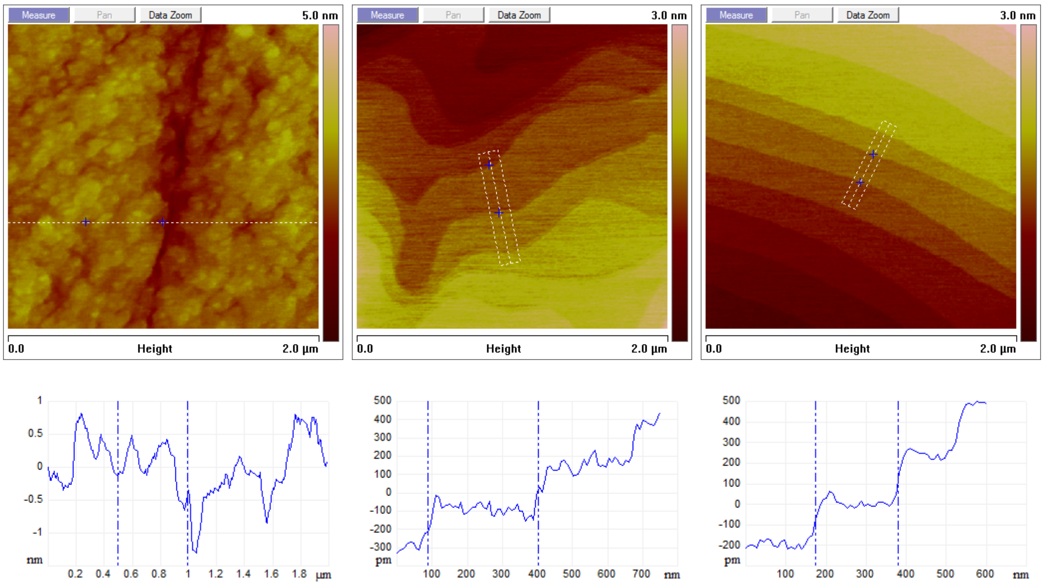

(a) 1000°C (b) 1200°C (c) 1400°C

Figure 6.6: c-plane: The formation of step-and-terrace morphology.

As previously discussed the c-plane substrates are rougher than the a-plane (see figure 6.3).

The topographic transformation from a rough surface to a terrace structure clearly arises for a temperature of 1200°C and above. However, small size AFM pictures of c-plane sapphire annealed at 1000°C shows small and round terraces (see inset of figure 6.7(a)) in addition to the large polishing scratches clearly visible by the large ditches in the picture. Sputtering and etching the surface could be a method of creating a more even surface before annealing, and by this obtain wider and longer terraces at lower annealing temperature i.e. at 1000°C, [73]. Terraces we obtained at 1200°C, have previously been shown for annealing at 1000°C at 1h [74]. At temperature of 1200°C, there are clearly seen terraces, but these are still very round in shape as seen on larger AFM pictures (see figure 6.7(b)) compared to annealed a-plane. Almost straight terraces appear only at annealing temperature of 1400°C.

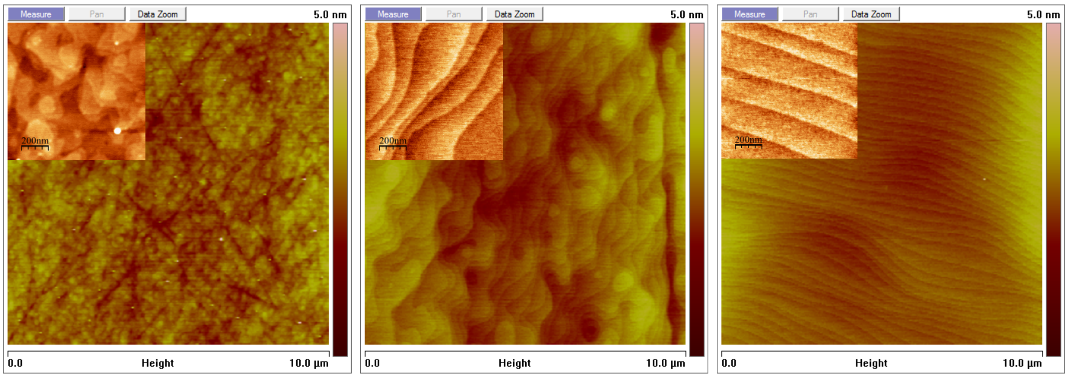

(a) 1000°C (b) 1200°C (c) 1400°C

Figure 6.7: Transformation from rough sample, to island formation and to terrace steps. Size of main picture is 10μm x 10μm, while the inset is 1μm x 1μm.

Terrace width

The influence of annealing temperature on the terrace width is shown in figure 6.8. The standard deviation of the measurements is defined as error bars on the graph. Samples a22 and a32 had very large terrace width, and are most likely from another sapphire wafer with a slightly different miss-cut angle so they are not included in this analysis, and will be discussed later. For a-plane, the terrace width is nearly constant and equal to about 240nm up to 1200°C and increases up to 490nm at 1400°C. The standard deviation of the measurements increases also with temperature, especially above 1200°C. As the annealing temperature increases, the atoms gain more energy and can travel further, also surmounting higher energy barriers i.e. the terrace height. Since we cannot see any change in the terrace step, a conclusion for the increase in terrace width as seen in figure 6.8 for a-plane is hard to find. A possible reason is discussed in the next subsection. In the case of c-plane the decrease in width is negligible, and also no conclusion can be drawn since the standard deviation is rather high. As seen in figure 6.6(b), at 1200°C the terrace width is not uniform over the terrace, so it is hard to extract a certain width. In general, the terrace width for c-plane sapphire is seen to increase from no terraces up to what is believed to be approximately the miss-cut angle terrace width. The miss-cut angle calculated for the annealed c-plane samples is found to be 0.06±0.025°, which is twice the angle compared to the a-plane un-annealed samples. A more uniform width is obtained at an annealing temperature of 1400°C, figure 6.7(c). The high standard deviation may be a consequence of the rough pre-annealed samples.

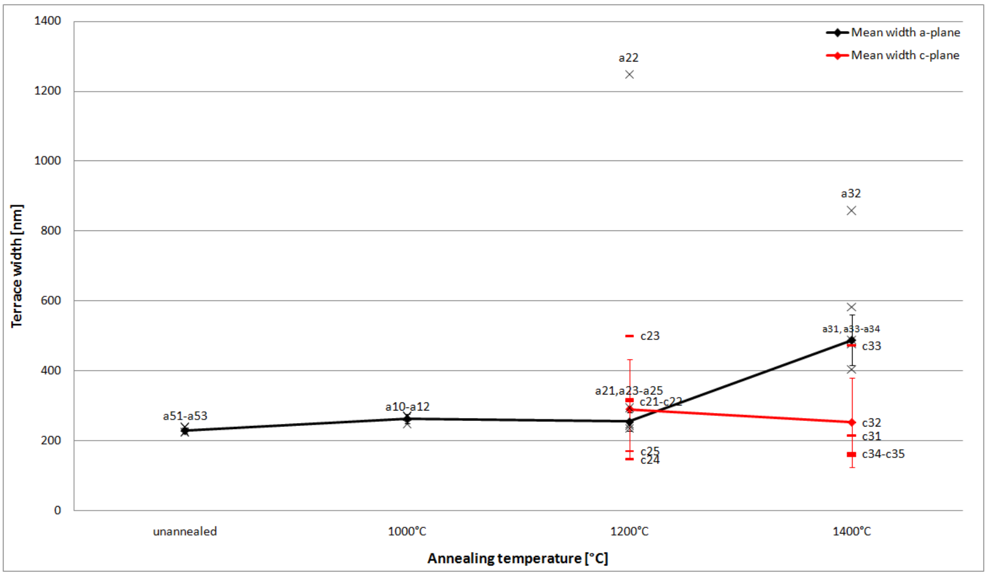

Figure 6.8: Terrace width given for un-annealed and three different annealing temperatures for a-plane, and at two different annealing temperatures for c-plane are given. The error bars represent the standard deviation of the measurements, and thus represent the variation of the terrace width.

Terrace height

The terrace height, influenced by the annealing temperature, is plotted in figure 6.9. For all the annealed samples, the step height is independent of the annealing temperature and is equal to 0.25±0.04nm for both the a- and c-plane, which also have been found in literature [75, 76]. This height corresponds approximately to one sixth of the atomic unit cell (c/6), hence to one atomic layer. These steps are very uniform over the examined surface (up to 10μm x 10μm), and there are no indications of more than one atomic step. Also the standard deviation indicates that we are not dealing with double steps. Increasing the annealing temperature above 1400°C was investigated by Simeonov et al. in 2008 where they claim that, for a-plane, the step height and terrace width increases significantly [66]. At 1400°C there was an observed shift from single atomic steps to double and triple steps, and at 1500°C the double and triple steps were replaced by majorities of triple and quadruple steps. Multiple terrace steps, formed by coalescence of steps, have been shown more pronounced on miss-cut samples [77]. None of these steps were observed in our experiment, and it is believed that this is because of the very low miss-cut angle and that the annealing temperature was not high enough. However the increase in terrace width at 1400°C (see figure 6.8), while keeping the miss-cut angle constant, might indicate that in some areas on the sample surface multiple step formation is likely to happen. This can explain the terrace width increase observed at the annealing temperature of 1400°C.

There is a major difference in step height from un-annealed to annealed a-plane sapphire. The mean height for un-annealed is 0.123±0.0243nm, which is one half of the annealed samples, 0.248±0.0245nm. This is less than one atomic step and seems to be an unfavorable state for the un-annealed samples. This terrace step height seems stable at room temperature, but rapidly doubles to one atomic step during annealing as seen in figure 6.9.

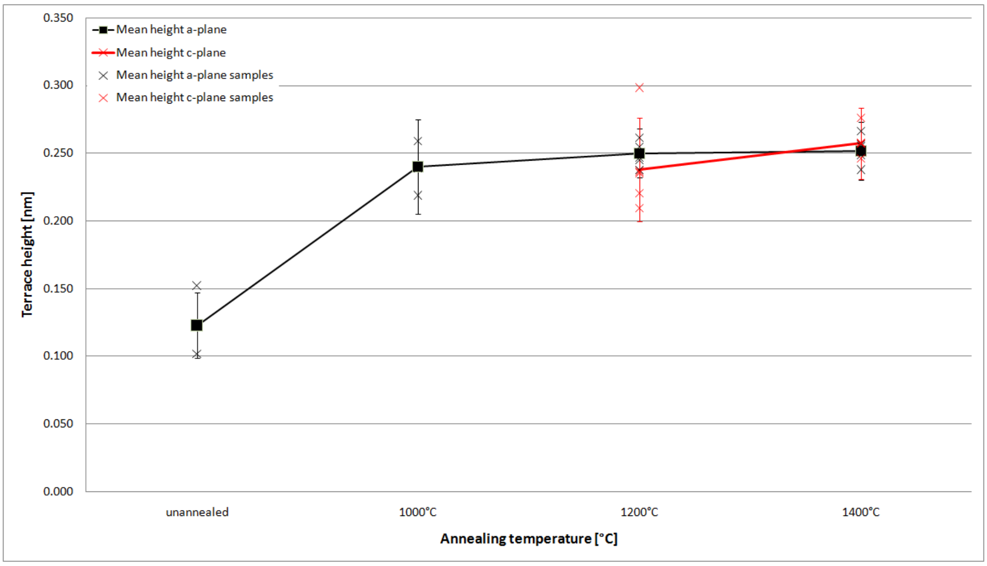

Figure 6.9: Terrace height of a- and c-plane sapphire, the error bars represent the standard deviation of the measurements, and thus represent the variation of the step height.

Surface roughness

In general, the terrace roughness is very low, <0.10nm. The measured terrace r.m.s. roughness for a-plane as a function of annealing temperature is gradually decreasing from 0.08±0.017nm, for un-annealed, to 0.056±0.012nm, for 1400°C annealed temperature (see figure 6.10). Obtaining a smoother surface at higher annealing temperature is expected since the high kinetic energy of the atoms enhances a lower energy state configuration. C-plane terrace roughness was measured to be 0.16±0.019nm and 0.11±0.014nm for 1200°and 1400°C, respectively. Terrace roughness for samples annealed at 1000°C could not be obtained because of the small terrace area. The overall roughness of the annealed c-plane samples calculated from a 2μm x 2μm area picture is also given in figure 6.10. It decreases from 0.33±0.04nm for 1000°C and 0.16±0.02nm for 1200°C, to 0.11±0.04nm for 1400°C. This means it is most likely that all of the scratches from the mechanical polishing were removed.

Large terrace width, sample a22

An interesting observation was done of sample a22 annealed at 1200°C. The sample was most likely from a different sapphire wafer. This sample was special since it had very large terrace width on the order of 1.248μm, contrary to the other samples annealed at the same temperature (around 0.25μm) shown in figure 6.8(a). After annealing, the surface had large round spots on its terraces, figure 6.11. The height of the spots was on the same order as the terrace height. In other words, the spots height was around 0.25nm, or c/6, indicating that this is no contamination.

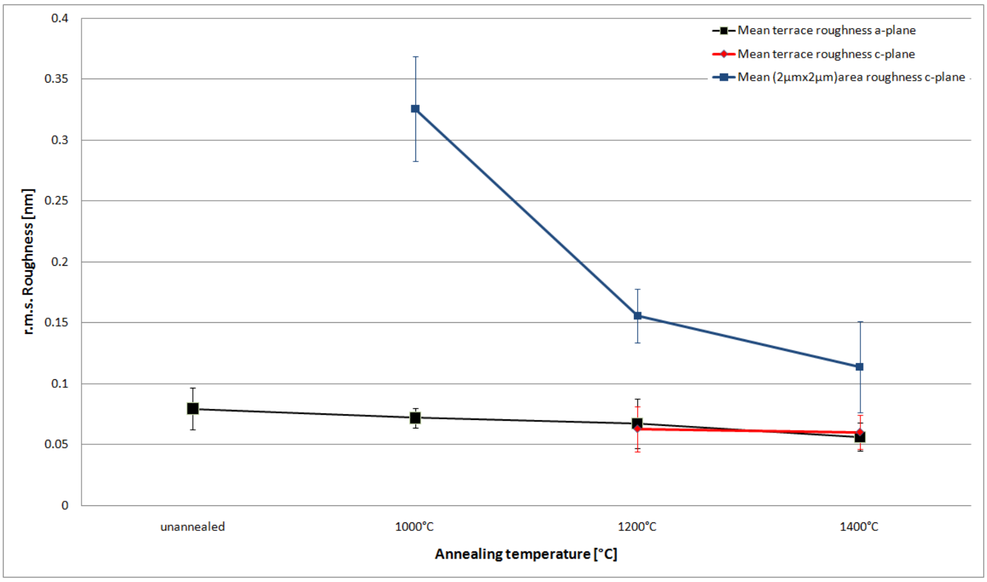

Figure 6.10: Roughness of a- and c-plane annealed sapphire, the error bars represent the standard deviation of the measurements.

The location of these spots was ∼ 700nm onto the terrace, and the sizes were on the order from approximately 30-300nm in diameter. The origin of these spots may be due to the diffusion length of the Al and O atoms during the annealing process. Either the annealing duration or the annealing temperature may cause the atoms to not reach the terrace step. Atoms travelling the diffusion length of approximately 700nm may find a free lattice space and nucleate in circular forms. These spots were only observed on this sample, and are most likely due to the large terrace width. The sample with second largest terrace width was a32 (width=859nm). This sample also had a terrace width above 700nm, and should therefore form spots. However, due to the higher annealing temperature (1400°C versus 1200°C), a higher diffusion length is expected which prevents the spot formation. In any case, as we would like to keep the system as simple as possible in order to understand the ZnO growth mechanisms, the spot formation is rather unwanted and samples showing this type of morphology will not be used for ZnO growth.

6.3 Conclusion

The main observation for post annealing of the sapphire substrate is the terrace formation. The terrace steps are created because the crystal was cut and polished with a mis-cut angle, and the high temperature annealing process promotes the surface reorganization to a lower energy state [78]. Therefore, the width of the terraces depends on the mechanically cut substrate, but also the annealing process. These terraces are very temperature dependent since the surface diffusion length of the atoms will increase with the temperature, which allows them to rearrange the surface structure. The higher the annealing temperature is, the straighter and wider the terraces become. It looks like the c-plane needs at least 1200°C to create terraces, while the a-plane has terrace formation of c/12-height as-received.

The mean height of the terrace steps are found to be around 0.25nm, with some deviations for

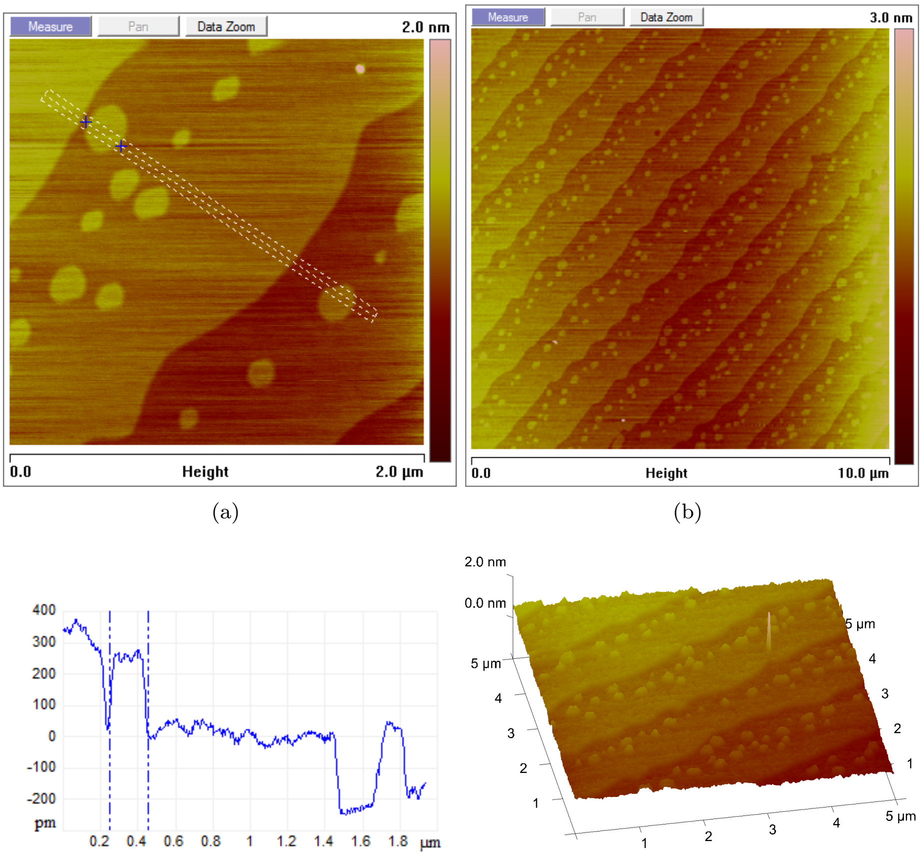

(a) (b)

(c) (d)

Figure 6.11: Sample a22 - Large terrace width. (a)-(c) Cross section of the terrace and two spots. (b) Same observation over a large area. (d) 3-D picture shows the spot and terrace has the same height.

both the a- and c-plane. This is the same as the distance between close packed oxygen planes in the sapphire structure (0.21nm), figure 6.1(b), and there is reason to believe that we are mostly dealing with single atomic plane steps [78, 79].

Different annealing temperature may affect the Au catalyst droplets and the ZnO PLD growth. In the next two chapters the Au droplets (chapter 7) and ZnO nanostructure growth (chapter 8) will be further investigated, and the influence of sapphire substrate annealing temperature will be discussed.

Chapter 7

Au droplets

In this chapter an investigation of the Au droplet formation on sapphire substrate will be looked into. A thin Au layer of approximately 1nm was evaporated on (see section 5.3) and annealed in order to form Au droplets. In section 7.1 an attempt of in situ observation of Au droplet formation by SEM will be carried out by warming a sample up to about 600°C while observing it in a Scanning electron Auger Microscope, referred to as SAM. In section 7.2 droplets on samples with different substrate temperature annealing will be investigated by first annealing at 700°C and afterwards analyze them by SEM and AFM.

Investigating the droplet formation is important in order to understand the catalyst growth of ZnO nanostructures on sapphire substrates. Information about droplet size and density may give some hints towards finding better growth conditions. Controllable diameter and density of the catalyst droplets can most likely lead to controllable size and density of the ZnO nanostructures. It will be investigated in this chapter whether sapphire surface influences the droplet size and density, in addition if the droplets like to arrange along the terrace edges or not.

7.1 Annealing in SAM

The picture of Au droplets at high temperature might be different from the picture in room temperature. This is one of the main reasons for observation of the in-situ Au droplet formation. In an attempt to observe in situ transformation from an Au thin film to Au droplets, two samples were warmed up in a UHV SAM chamber. This was to observe the droplets at elevated temperature to see how they are formed at a temperature very close to the ZnO deposition temperature. In situ observation of Au droplets is desirable since the droplets may change at room temperature versus elevated temperatures. It is also important to know if the droplets are in liquid or solid phase under elevated temperature.

7.1.1 Experiment

The SAM was a Jamp-9500F Field Emission Auger Microscope with a specimen heating device. The instrument could heat the sample up to a temperature of approximately 600°C while capturing images using SE. The initial base pressure in the SAM chamber was below $1.0 \cdot 10^{-8}$mbar. The samples were mechanically clamped onto a sample heater and inserted into the SAM. To calibrate the heating element a test sample was used and the sample temperature was measured with an optical pyrometer at a wavelength of 1.5μm. The temperature range for the optical pyrometer is from 300-1600°C. Temperatures below 300°C were not measured because they are of no importance. The temperature was then manually controlled with a current source connected to the heater. A pressure below $4.0 \cdot 10^{-7}$mbar was maintained during the entire experiment. Figure 7.1 shows the measured sample temperature versus the applied heater current. The spread in measured temperature is due to several measurements during temperature stabilization. The stabilized temperature is given as the maximum temperature in the spread. The stabilization time for the real sample with a heater current at 1A is about 74min, and at a heater current of 1.5A is about 10min.

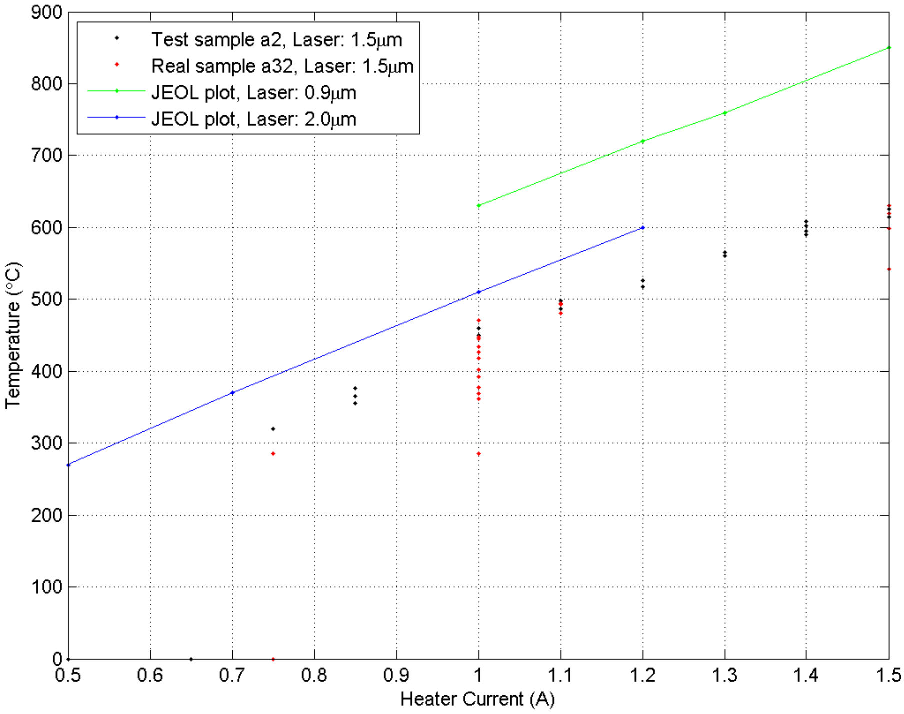

Figure 7.1: Temperature increases almost linearly due to the applied current. Measured data coincide with data given in the manual. Spread in measured temperature is due to several measurements during temperature stabilization.

It can be seen that the measured temperature and the values provided by the vendor follow linear curves, which are parallel to each other. The graphs are most likely parallel because of the dependence of the type of IR thermometer and the measurement environment used. In general, an IR thermometer that uses shorter wavelength is more appropriate for measuring higher temperature [80]. Our measurements are lower than the vendors is due to the fact of the non-adjusted emission intensity level of the IR thermometer (described in section 5.4.4). Figure 7.2 shows the sample temperature (a) and heater current (b) versus time. The relaxation time during heating is about 10 min. Increasing the current from 1.2A to 1.3A increases the temperature from 526°C to 565°C, then it takes approximately 8 minutes for the temperature to saturate. These measurements on the test sample were used for guidelines when measurements were performed on the real sample.

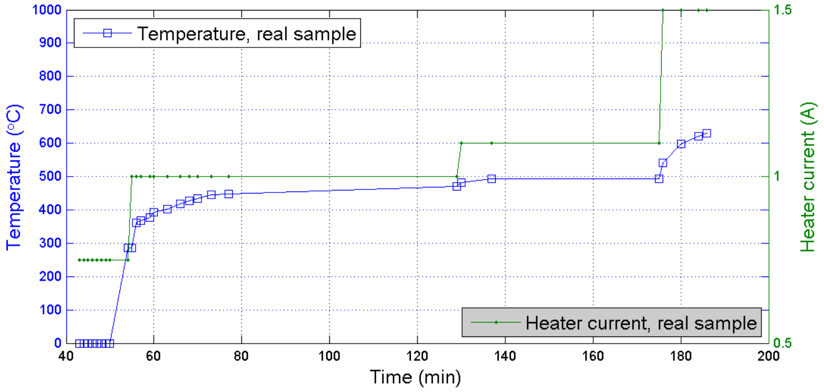

(a)

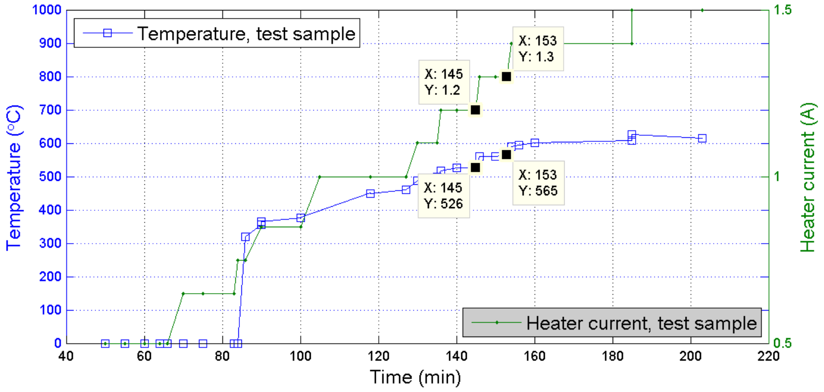

(b)

Figure 7.2: Temperature and current measurements as a function of elapsed time for (a) real sample and (b) test sample

The substrate of the real sample, named a32, consists of a $(11\overline{2}0)$-sapphire substrate annealed at 1400°C, and with a 1.1 nm Au thin film evaporated on. An e-beam evaporator was used for manually depositing the Au thin film at a minimum rate of 0.1Å/s according to a quartz crystal element. The sample was heated according to figure 7.2. At temperatures from 400-600°C the surface was closely investigated at different areas and also at some reference points[1], and images were taken. However, high resolution images were hard to obtain. One of the reasons could be the increase in chamber pressure due to the temperature increase. Another factor was a periodic noise source introduced when connecting the current source to the SAM. An attempt of grounding the current source to the SAM led to no change. A result of the last picture taken after approximately 3 hours ramping of the real sample, at a temperature at 630°C is given in figure 7.3. The periodic noise is seen as two white lines in the picture, more lines were observed when changing the scan speed from slow to fast. The origin of the noise is believed to be external,

---

[1] reference points - points on the sample close to large contamination particles. This to investigate the same spot during temperature ramping

since when the scan speed is changed the data acquisition time is increased and more lines are observed. The noise disappeared when the external current source was disconnected. In the limit of the resolution there was no clear observation of Au droplets. It is possible that Au droplets were formed, but this was not possible to observe in the SAM without some optimization of the image resolution. Examples of optimization could be to remove the external noise or to make the sample more conducting in order to increase the electron beam voltage.

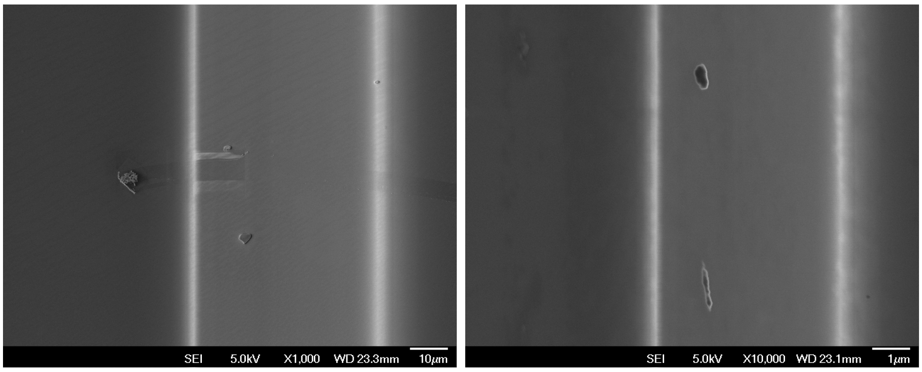

(a) (b)

Figure 7.3: SAM picture of the real sample, a32, at 630°C at a magnification of (a) 1kx and (b) 10kx.

AFM pictures taken of the sample before and after annealing in SAM shows that the terrace structure is visible after a layer of 1.1nm Au is evaporated onto the sample, figure 7.4. The thin film layer looks uniform over the surface. Visual inspection of the sample before and after annealing in the SAM revealed clearly a brighter color of the Au thin film after annealing. This indicates that the morphology of the Au layer have changed, resulting in a more transparent layer. Also, an indication that Au particles coagulate randomly is seen on AFM pictures in figure 7.4(b) and (c). It is therefore certain that something happened to the Au thin film during SAM annealing. The difference is so small that the SAM could not detect these kinds of surface changes.

However, when the real sample (a32) annealed at 630°C in SAM is compared to a sample (a31) annealed at 650°C in PLD chamber it is in the latter case seen a clearer indication of Au droplets, see figure 7.5(a). In the former case no clear Au droplet can be seen, see figure 7.5(b). The annealing condition in SAM was performed with ramping and annealing equal to 3hours at $\sim 3.7 \cdot 10^{-8}$mbar pressure. In the PLD chamber annealing was performed at a temperature rate of 10°C/min and at a pressure of 0.5mbar with (O_2/Ar) gas ambient. This indicates that we have incomplete annealing in the case of SAM. This can be explained by the annealing conditions; time, pressure, gas ambient and temperature. As temperature seems to be the most logical explanation of droplet formation, it is important to have at least 600°C for droplet formation. Since pressure and gas ambient differ greatly, this may also be of influence. Further investigations regarding the droplet formation are needed.

It has previously been shown (on fused quartz substrates, SiO_2) that as the annealing temperature of the Au thin film (thickness: 2-8 nm) increases, the nano particles grow in size because of the enhanced surface diffusivity of Au. This was observed in all of the samples for annealing up to 900°C [81]. At longer annealing time Ostwald ripening comes into play so that the average Au droplet diameter increases with longer annealing times [82]. To be able to control the size

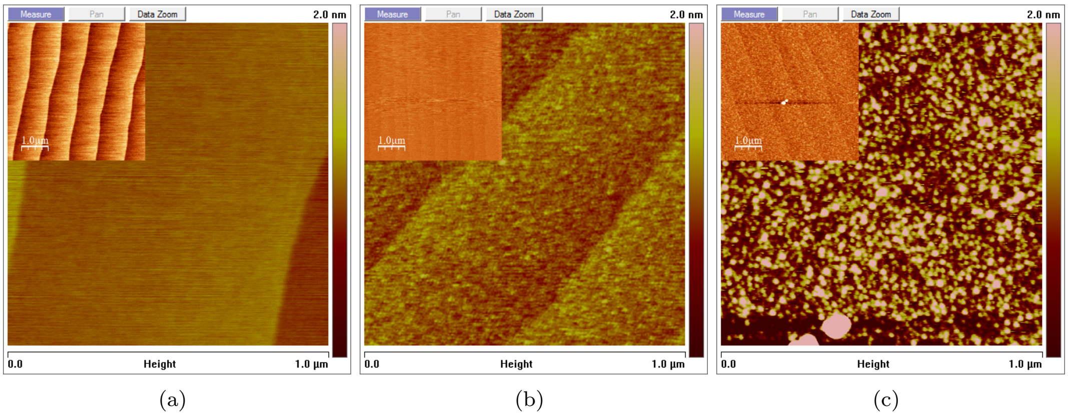

(a) (b) (c)

Figure 7.4: Surface. (a) Annealed substrate without thin film (a32). (b) Annealed substrate with non annealed Au thin film (a33 - Different sample, but same treatment as a32). (c) After ramping and Au annealing in SAM for approximately 3 hours (a32). Size of inset picture is 5μm x 5μm.

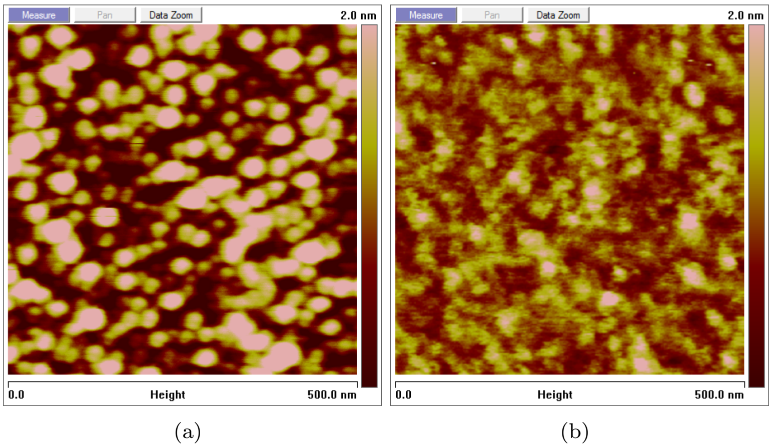

(a) (b)

Figure 7.5: PLD annealing versus SAM annealing. (a) a31 - PLD Annealed, 650°C, 10°/min. (b) a32 - SAM Annealed, 630°C, about 3hours ramping.

and density of the Au droplets as a ZnO nanorod catalyst would be of interest in our hybrid solar cell. This is to optimize the solar cell such as; reducing the electron resistivity in the ZnO nanorod (large droplets), large absorption area (low density/small droplets), high capturing of excitons (high density/small droplets).

7.1.2 Conclusion

No Au droplet formation could be observed during SAM annealing up to a temperature of 630°C, nor any clear droplets by AFM afterwards, even though a clear color change of the sample surface before and after annealing is observed by visual inspection, and also a change of the surface Au layer towards more coalescence of Au was seen by AFM. Droplets could not be observed by SAM because of the limit of the resolution and since the droplet most probably had not coagulated enough due to the low annealing temperature.

7.2 Droplet formation in PLD

In order to investigate the Au catalyst droplets formation pre-deposition, samples were heated in the PLD chamber up to the deposition temperature and removed from the chamber before ZnO deposition. As the terrace height is around 0.25nm it would be interesting to see if the Au droplets align on the terraces or if the terrace structure on the substrate has any influence at all.

Characterization of the annealed Au thin film can be done in both SEM and AFM. The strength of the SEM picturing is the trustworthiness of the pictured Au droplet. While scanning the surface with an AFM tip distortion can occur by a defect tip or the scanning angle of the tip versus the sample. This can be a limitation when looking at the shapes of the nano-sized Au droplets when size and shape are of importance. An advantage of using AFM is the additional knowledge about the height of the droplets, and also it is easier to depict the terrace steps of the substrate. A problem regarding the image capturing in SEM, explained later, led to the characterization of the Au droplets using mainly the AFM. SEM and AFM are two very good methods of microscopy for imaging structures on the nanometer scale, and also complementary techniques that provide a more complete representation of the surface. The AFM provides information about the height with a vertical resolution smaller than 0.5nm in addition to characterization tools like measuring the sizes of the particles in an easier manner than SEM.

7.2.1 Experiment

A thin layer of approximately 1nm was evaporated onto eight samples with different substrate temperature annealing, see table 7.1. The Au layer was evaporated on in two batches, referred to as (#1) and (#2). The temperature was set to 700°C with a ramping rate of 10°C/min. The surface temperature of the samples was measured by an optical pyrometer (λ=1.5μm) 5 minutes after the set point temperature had been reached. After the temperature had been measured the heater was turned off and the samples were cooled down to room temperature. The samples were annealed in the PLD chamber in order to obtain the same environment as before the growth of ZnO nanostructures. A pressure of 0.5mbar with Oxygen/Argon (5%/95%) was ambient during the entire annealing process. Since the substrate holder was rather small the annealing process was carried out in two batches, referred to as (#1) and (#2).

Sample	Substrate annealing	Au layer	Measured annealing temp.
a50	unannealed, $(11\bar{2}0)$, Al_2O_3	1.1nm (#1)	630°C (#1)
c50	unannealed, (0001), Al_2O_3	1.1nm (#1)	633°C (#1)
a10	1000°C, $(11\bar{2}0)$, Al_2O_3	1.3nm (#2)	650°C (#2)
c10	1000°C, (0001), Al_2O_3	1.3nm (#2)	640°C (#2)
a21	1200°C, $(11\bar{2}0)$, Al_2O_3	1.3nm (#2)	623°C (#1)
c21	1200°C, (0001), Al_2O_3	1.3nm (#2)	625°C (#1)
a31	1400°C, $(11\bar{2}0)$, Al_2O_3	1.3nm (#2)	650°C (#2)
c31	1400°C, (0001), Al_2O_3	1.3nm (#2)	640°C (#2)

Table 7.1: Samples used for Au droplet characterization.

7.2.2 Characterization Method

Several analyses were tried out in order to determine the size and density of the droplets. Manually measuring and counting the droplets led to an overestimate of the droplet size and poor statistic information in lack of gathered data. AFM software tools from Nanoscope led to an easier, semi-automatic characterization technique, but also here a manual selection of droplets had to be made. A third method, taking the fast Fourier transform (FFT) of the droplets led to inconclusive results because of the variety of shapes and difficulties in defining the droplets. The last method, using ImageJ software, led to the best reliable results.

Selecting the height scale bar of the AFM picture of about 5nm and choosing a high contrast picture is shown in figure 7.6(a). Nearly formed droplets are automatically separated by a watershed method, and converted to binary bitmap, figure 7.6(b). Droplets less than 5nm are of no interest and thus disregarded. Also, the largest Au ”droplets” are disregarded since these have either not yet been transformed into droplets or they can not be discerned by the AFM measurements, figure 7.6(c). If the case is that the large ”droplets” have not been dissociated by the annealing treatment they will participate in the VLS growth as large Au catalyst. Nevertheless they have been disregarded in order to emphasize the more normal droplets. In the case of droplet density, the larger droplets have been accounted for. As seen in figure 7.6(d), a Gaussian distribution function shows that sample a10 has a mean droplet diameter of 10nm with a standard deviation of approximately 3nm. All histograms of the investigated samples are found in appendix B. An area between $0.25\mu\text{m}^2$-$4.0\mu\text{m}^2$ has been chosen for the AFM droplet measurements. This has influence on the measuring uncertainty due to the resolution of the picture. The smallest area (highest resolution) gives an uncertainty of 1.18nm/pixel, while the largest area (lowest resolution) gives a measuring uncertainty of 4.74nm/pixel. Choosing the best area is a trade-off between accuracy and statistic information, concerning both SEM and AFM. The investigated area has been selected from which picture shows least distortion and best sharpness.

SEM characterization contributed to better certainty of the Au droplets size and density and was very essential to confirm the data acquired from the AFM measurements. SEM also helps because the AFM has the problem of the tip shape, which can affect the captured image of the topography. In figure 7.8 sample c31 is looked at in both SEM and in AFM, comparing the sizes of the Au droplets. As seen, the AFM picture has higher depth resolution and the contrast helps to get a better picture of the surface topography, while the SEM picture may suffer from low contrast, which may be a problem during the characterization. Also a major problem regarding the negative charging of the isolating sapphire surface led to bad imaging of magnifications above 25k. The charging effect is because the number of electrons (secondary and backscattered) hitting the surface is higher than electrons leaving the surface. This can be avoided by reducing the electron voltage, which is the idea behind low voltage SEM for non-conduction specimens without conductive coating. This problem was hard to overcome for some samples when focusing the electron beam at a small area (magnifications above 25k).

Contamination

During SEM analysis, some larger droplets were observed on the substrate surface. These larger droplets (further on referred to as contamination) were not expected, and it is believed that this contamination was introduced after PLD annealing. This is believed because samples first observed by AFM did not have this characteristic, while samples first observed by SEM and afterwards by AFM indicated some sort of contamination. In figure 7.7 these larger droplets, or contamination, are shown. An even distribution over almost the entire sample, and also over several samples was first believed to be Au droplet coagulation due to the electron beam

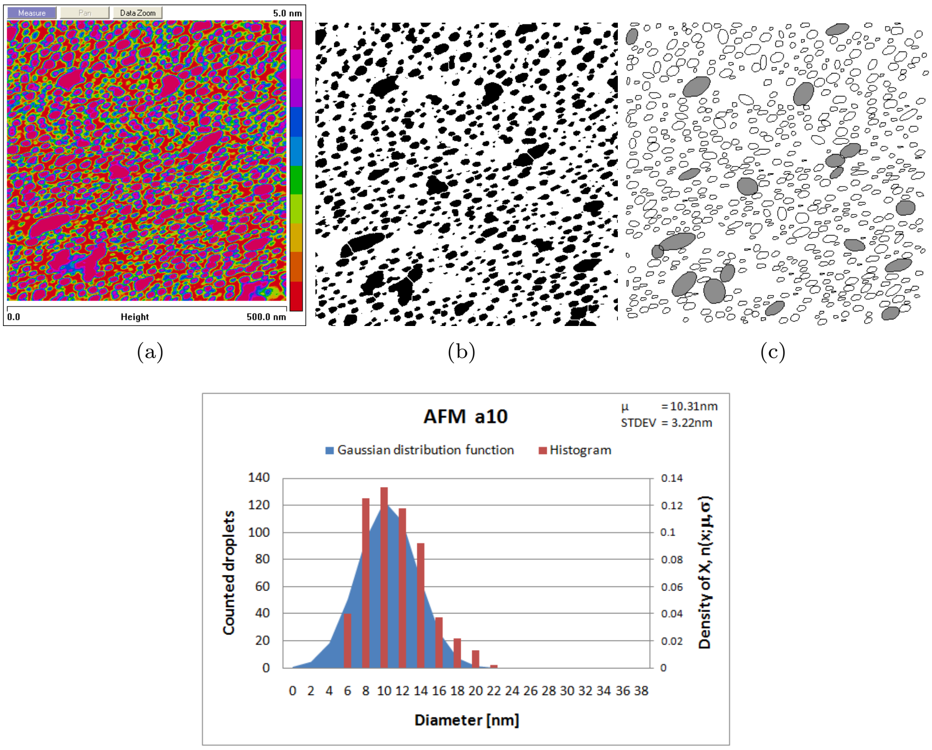

(a) (b) (c)

(d)

Figure 7.6: ImageJ characterization method. (a)-(b) Select and emphasize the Au droplets. (d) Remove large Au droplet. (d) Histogram and Gaussian distribution function for the counted droplets.

of the SEM. However, it is more likely an introduction of some sort of foreign material, since Au on sapphire substrates is known to be very stable, and since several previously experiment regarding Au droplets on sapphire have been reported successfully [83, 43]. An EDX scan on one sample (a10) indicated some traces of Cu on the surface, see figure 7.7(c), in addition to the substrate material Al_2O_3 and the Au droplet. The indication of Cu could come from the Cu tape used to mount the substrate onto the sample holder. The tape is folded onto the surface which could introduce the contamination shown on the samples. Due to lack of results, it can not be concluded if Cu is observed on each sample showing this ”large droplet” phenomenon. No such contamination was observed by SEM or EDX on ZnO nanostructure growth and it is with large certainty that this large droplet contamination is introduced after the samples are removed from the PLD chamber.

7.2.3 Results and discussion

Organization of Au droplets

The terrace width is on the order of 10-20 times wider than the diameter of the Au droplets. For only one case (c31), real organization of Au droplets towards the terrace steps was observed. The terraces are shown in both SEM and AFM characterization, see figure 7.9(a) and (b), respectively.

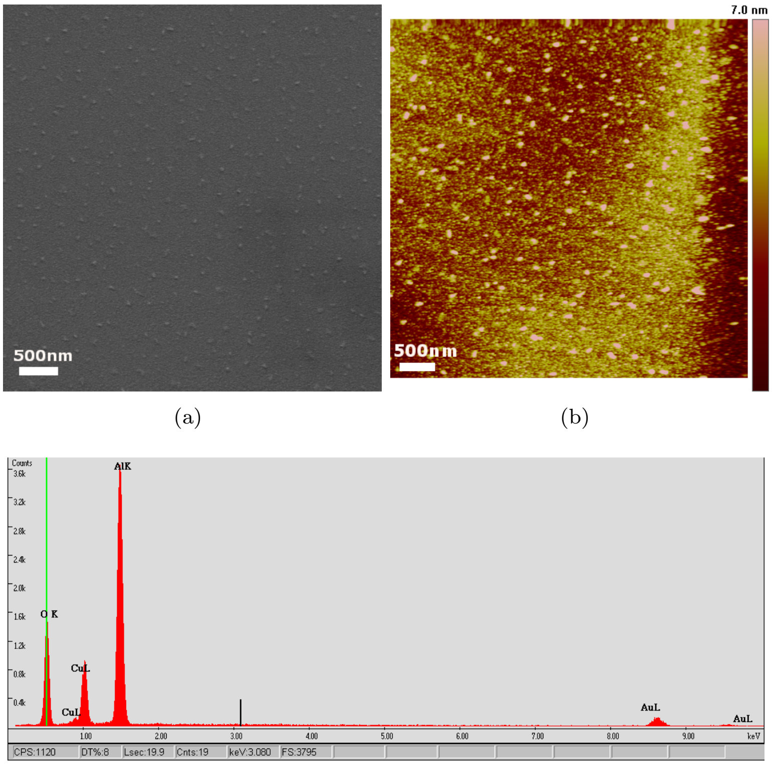

(a) (b)

(c)

Figure 7.7: Contamination on a10 pictured first in (a) SEM and afterwards in (b) AFM. (c) EDX picture indicates Cu contamination.

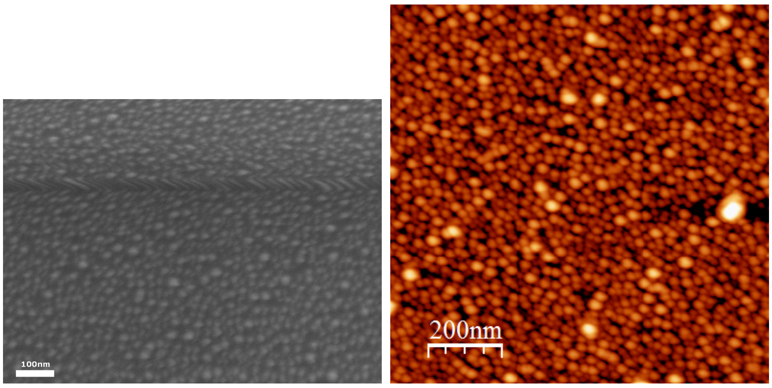

(a) (b)

Figure 7.8: c31 annealed at 700°C in PLD chamber. (a) 1μmx0.75μm SEM image. (b) 1μmx1μm AFM image.

The terrace width is on the order as the terrace formation before Au deposition (figure A.8(a)). Alignment towards the terrace steps imaged by AFM could only be seen at an area of at least 20μm x 20μm. This was not in the standard image capturing series, so terrace structures for other Au droplet samples may be observed at larger capturing areas by AFM. A reason for this can be that the droplets are so small, and the density is so high, that terraces do not show at high magnification. A picture of a larger area shows more height variation, and therefore more contours are noticeable. However, since the other SEM and AFM pictures did not reveal any organization of the droplets towards the terrace steps, it is concluded that the droplets are, in general, not really influenced by the terrace structures. The droplets are also several orders of magnitude higher than the terraces step at an approximate ratio of 4:0.25nm, respectively. An explanation of why the Au droplets do not align towards the terrace step could simply be because the energy was too low. Since the temperature is not high enough, the Au atoms had too low mobility to diffuse towards the terrace step.

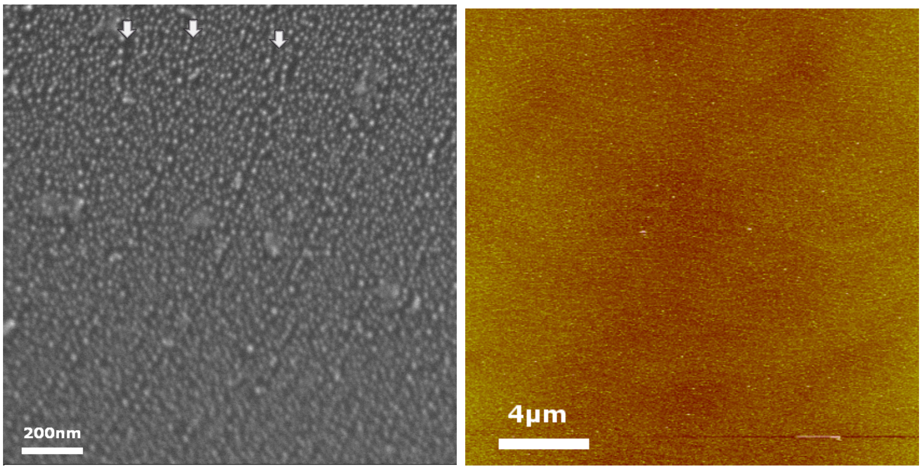

(a) (b)

Figure 7.9: Au droplet alignment towards the terrace structure for c31 shown by (a) SEM and (b) AFM.

Statistics of Au droplets

The diameter of the droplets was derived from the area of a circle, given in equation 7.1. In general, the obtained Au droplet diameter characterized by SEM was a little bit smaller than for the AFM characterization. All the measured data are given in appendix B, and a short summary is listed in table 7.2. As seen in table 7.2 this minor deviation is common to every sample. This is also expected due to the shape of the AFM tip, which can give an overestimation of the droplet size. An underestimation of the diameter in case of the SEM pictures can occur from the ImageJ characterization technique. When a poor contrast picture is obtained by SEM, it can be difficult for the ImageJ software to define the shape and size of the droplets, causing an underestimation of the droplets area. According to the standard deviation of the diameter the AFM and SEM, results are within reason. It is therefore found that the AFM pictures and characterization are to be trusted as confirmed by the SEM characterization.

Sample	Diameter [nm]	St. dev.[nm]	# droplets	Density [droplets/μm^2]	Circ.
AFM a50	22.3	9.5	503	503	0.871
AFM a10	10.3	3.2	600	2400	0.804
AFM a21	22.1	13.2	859	215	0.919
AFM a31	18.3	7.6	326	326	0.830
AFM c50	27.8	14.3	712	178	0.874
AFM c10	12.9	4.6	458	1832	0.871
AFM c21	22.8	11.1	357	357	0.788
AFM c31	15.8	6.5	746	746	0.877
SEM a10	8.8	2.7	1793	3247	0.224
SEM c10	10.2	3.2	5419	1856	0.777
SEM c31	12.0	5.3	615	1130	0.262
SEM c50	18.6	10.4	3758	329	0.725

Table 7.2: Summary of Au droplet measurements

$$A = \pi r^2 \quad \rightarrow \quad d = 2 \cdot \sqrt{\frac{A}{\pi}} \tag{7.1}$$

$$circ = 4\pi \frac{area}{perimeter^2} \tag{7.2}$$

,where perimeter is the length of the outside boundary of the selection.

The droplet density is overall higher in SEM measurements compared to AFM measurements. This indicates that several small droplets are missed in the AFM measurements. This can be in the ImageJ software where the contrast is set to extract the droplets. The droplets vary in height and also the transition between droplets is often unclear. This makes it difficult to determine the height set point. Another limitation which may cause the difference in droplet density is the case of a dull AFM tip. This can influence the results by measuring two small droplets to be one, causing an increase in droplet diameter and a smaller droplet density. A worn tip may miss the smallest droplets in addition to creating bad images. The droplet density measurements have larger deviations and are more uncertain, but can be taken as an indication number. If the droplet density is plotted as a function of the droplet diameter it can be approximated to a power regression function as shown in figure 7.10. This seems reasonable and makes the droplet density data more reliable. A decrease in droplet density as the diameter increases is an indication of the Ostwald ripening as described in section 3.1.1. The Ostwald ripening says that the small particles out-diffuse to the larger ones.

As shown in table 7.2 the circularity of the AFM droplets are much higher than for the SEM droplets. The formula for circularity is given in equation 7.2, and the low circularity in the SEM pictures may be a consequence of the low contrast of the SEM pictures. In addition, the high circularity of the droplet measured by AFM could be due to a dull cantilever tip, which depicts shapes to be more round than they actually are. High circularity is, however, expected since it is a general tendency due to the large difference in surface energy between Au and the substrate[84]. According to the circularity, the AFM predicts the best images.

In table 7.2, the number of counted droplets for AFM and SEM is given. A high number of droplets characterized by SEM give good statistical data at a relatively low measuring uncertainty ($\sim$ 1.1px/nm at 100kx).

In figure 7.11, the average value and the standard deviation of the droplets are pictured. As seen there is no clear correlation between the droplet size and the substrate annealing temper-

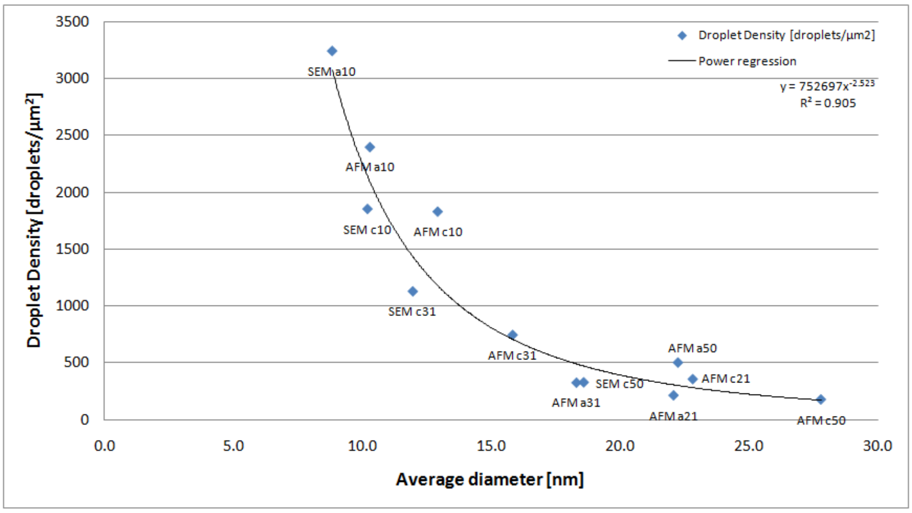

Figure 7.10: Droplet density as a function of the Au droplet diameter.

ature. There may, however, be a correlation of the sample annealed in the same batch. It is seen that the four samples with lowest diameter are the samples which were annealed in batch #2 (see table 7.1). The droplets may, therefore, be very sensitive to the annealing environment and the thermal contact of the Ag paste, even though the annealing experiment was performed under the same conditions. From figure 7.11, it is seen that the increase in diameter also causes an increase in standard deviation, which may indicate the Ostwald ripening effect. This causes the large droplets to increase, and small droplets to decrease and in the end disappear. This causes the standard deviation to increase as the average droplet diameter increases, and it may not be a wanted effect in our case.

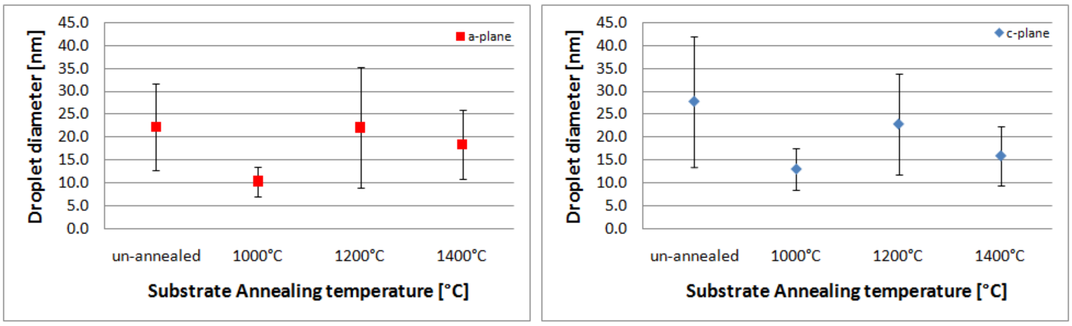

(a) (b)

Figure 7.11: Diameter of Au droplets as a function of annealed substrate temperature for (a) a-plane and (b) c-plane.

7.2.4 Conclusion

Droplets with a diameter around 20nm are formed when annealing a 1nm thin Au film on sapphire ($11\bar{2}0$ and (0001)) substrates at 700°C. These are observed at room temperature and stable over a long period of time, as evidenced by imaging the same sample right after annealing and one month later. Imaging in SEM is quite difficult because of the non-conducting sapphire substrate, and also the characterization is not an easy task because of the difficulty in separating the droplets. Annealing temperature and thermal contact are believed to be important parameters since 700°C is a critical temperature for the Au droplet formation. The substrate annealing temperature and terraces of the different samples could not be correlated to the Au droplet diameter, density or alignment. In the following chapter ZnO will be deposited by PLD on a- and c-plane sapphire substrate annealed at different temperature. The Au droplets will then be formed as the sample is ramped up to the deposition temperature of 700°C. The same droplet formation is expected even though the deposition starts at maximum temperature and the down-ramping is omitted.

Chapter 8

ZnO nanostructures grown by PLD

Influence of sapphire substrate annealing of ZnO nanostructures grown by PLD have been closely investigated. In this chapter the growth of ZnO nanostructure on $(11\bar{2}0)$ and (0001) sapphire substrate will be discussed. The discussion will mainly be based on obtained results. In general, PLD growth of ZnO thin films tend to be c-axis oriented with their hexagonal basal plane parallel to the substrate, regardless of the substrate[6].

8.1 Experiment

The experimental setup with laser path, the PLD chamber and experimental procedure have closely been described in chapter 5. Both a- and c-plane sapphire, annealed with different substrate temperature, were used. Together 8 samples were investigated. In addition un-annealed, 1200°C, and annealed 1400°C substrates were grown twice in order to investigate reproducibility and to look at the differences. In each PLD growth, two samples were introduced into the chamber simultaneously. The growth temperature was set to 700°C, but the sample surface temperature was measured to be around 630°C, while the sample holder temperature was around 720°C (see table 8.1). The laser voltage was adjusted so that the power measured on an external power meter after the optics showed exactly 0.2W at a pulse frequency of 10Hz. The deposition fluence on the target resulted in 1.33J/cm^2, while the pressure was 0.5mbar with 5% O_2 and 95% Ar gas ambient.

Before deposition, the samples were completely covered with a 1nm thin film Au, except for one region noted as the clamp region. This was where the paper-clip was fasted during the Au evaporation. This clamp area was also investigated to understand the difference in growth mechanism.

After PLD of ZnO the samples were investigated by SEM at an accelerating voltage of around 5kV with a standard 30μm aperture and at a working distance of 5mm, as this turned out to be good settings for high resolution imaging. EDX was used to conclude the presence of the right materials, as Zn, O, Al and Au (data not shown here). In addition, XRD data were used to determine the epitaxial growth of the ZnO nanostructures.

Sample name	Substrate name	Substrate annealing temp.	Temperature holder average [°C]	sample average [°C]
ucag090101	-	un-annealed	710	608
acag090101	-	1000°C	710	608
uaag090102	-	un-annealed	715	640
aaag090102	-	1000°C	715	640
acag090404	c22	1200°C	725	637
aaag090404	a23	1200°C	725	637
acag090401	c33	1400°C	760	650
aaag090401	a33	1400°C	760	635
acag090402	c34	1400°C	715	654
aaag090403	a34	1400°C	713	620

Table 8.1: Samples used for ZnO PLD growth. Nomenclature: i.e.: aaag - annealed, a-plane, aluminum oxide, gold. ucag - unannealed, c-plane, aluminum oxide, gold.

8.2 Results and discussion

The deviation from the surface sample temperature and set point temperature is most likely due to measurements with the optical pyrometer explained in chapter 5.4.4. The temperature deviation of about 100°C of the sample surface compared to the heater is also most likely due to the emissivity value of the pyrometer, since two different materials were measured. The low thermal conductivity of sapphire as an insulator may also be an explanation for the low sample temperature. The deviation between the temperature measured on the sample and the heater is most likely due to the Ag paste, since this is temperature difference is not constant. The temperature stability during deposition was rather good as the heater regulated the current and voltage around 13±1A and 14±1V, respectively, in order to obtain a stable temperature.

8.2.1 Combination of VLS and VS growth mechanism

As for Au catalyst growth, a triangular type of nanostructure was obtained, referred to as a *nanosheet*. In figure 8.1 the nanosheet is depict with the Au droplet on top of the ZnO material. The Au particle was on the same order as pre-PLD, hence approximately 15nm-20nm, which clearly implies VLS growth. The nanosheet base width was on the order of about 120-500nm, while the height on the order of 250nm to 1μm. The depth of the nanosheet was slightly larger than the droplet diameter, around 40-50nm.

Another indication of VLS growth is seen in the clamp area of the sample, in the transition area between the Au catalyst and the non-catalyst. In figure 8.2, a different growth mechanism for the non-catalyst area is clearly seen. The nanostructures were higher in the catalyst region. This was observed for every sample, independent of substrate annealing temperature and substrate cut plane.

The nanosheet display an anisotropic thickness distribution. As seen in figure 8.1 the width significantly exceeds the depth. As the Au catalyst droplet are much smaller than the nanosheet width it is unlikely that VLS growth mechanism is the only one present. A combination of VLS and vapor-solid (VS) growth mechanism is therefore proposed [49]. While VLS growth follows one direction, the ZnO get deposits on the side facets vis VS growth as the structure continues to grow. Growth rates at different ZnO facets is most likely causing the anisotropic nanosheet growth. The non-catalyst growth seen on the clamped area is most likely VS growth, in addition to the regions between the nanosheets. This growth mechanism has to be further investigated

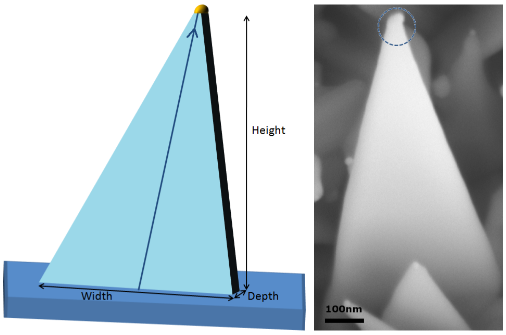

(a) (b)

Figure 8.1: (a) Illustration of nanosheet found for Au catalyst growth of ZnO at 700°C. Au droplet and growth direction is shown. (b) SEM image of nanosheet grown on c-plane sapphire.

in order to be fully understood.

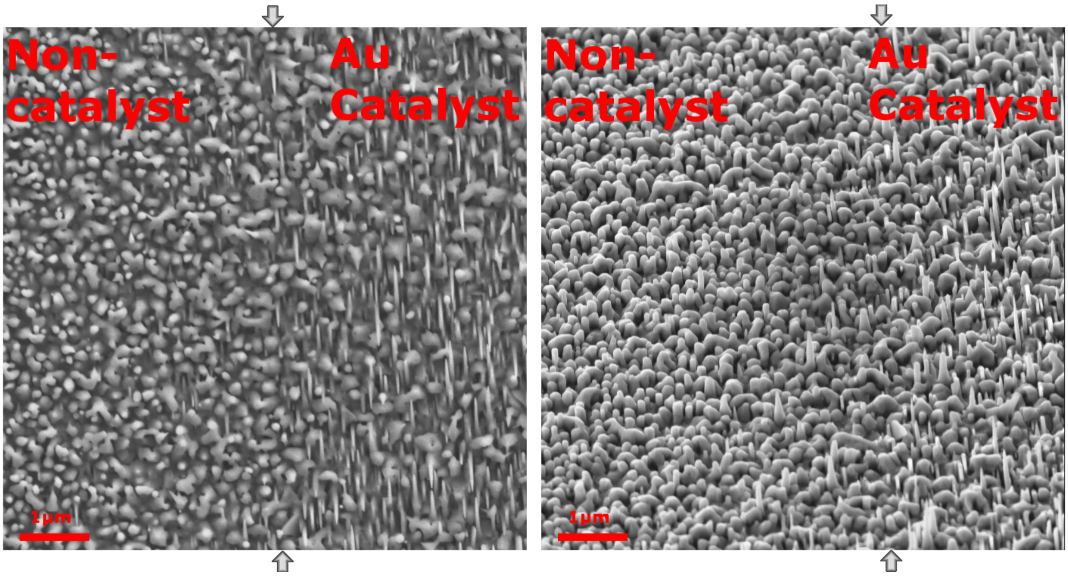

(a) (b)

Figure 8.2: Non-catalyst and catalyst growth in the clamped area. (a) 0°view. (b) 45°tilted view

8.2.2 Growth condition

From the SEM pictures captured after PLD, the substrate annealing treatment had great influence on the ZnO growth. For a-plane sapphire the best ZnO nanostructure growth condition was found to be on substrates annealed at 1000°C-1200°C. No nanosheets were found on un-annealed substrate, and poor growth was found on substrate annealed at 1400°C. For the c-plane sapphire the best ZnO nanostructure growth condition was obtained at substrate annealed at 1200°C-1400°C. Rather poor growth or no nanosheets were found on un-annealed, and annealed at 1000°C substrates.

Nanosheets on a-plane

As seen in figure 8.3, the nanostructure growth is enhanced for substrates annealed at 1000-1200°C. It is believed that the surface plays an important role to the growth of ZnO nanostructures. In general, annealed substrates achieve better growth conditions than un-annealed substrates. This is due to the lowering of the surface energy as a consequence of the better crystal structure after thermal treatment. All a-plane substrates samples are terrace structured, which would, in general, enhance the growth condition (see AFM pictures in figure 8.3(a)-(d)). These terraces are very parallel to each other. As discussed in chapter 6, the annealing treatment makes the terrace steps more defined, decreases the terrace roughness and increases the terrace height. More defined steps and a smoother surface makes the transition more uniform between the substrate and ZnO material. Adatoms sees the same atom connections over a large surface area, and it is easier for them to move over the surface since there are fewer defects. This makes the deposition uniform. The Au catalyst droplets speed up the ZnO growth throughout the VLS mechanism towards the enhanced sapphire substrate.

Good growth; 1000°C-1200°C: More defined terrace structure is believed to be important for good growth condition, and is believed to be one of the reasons for the good growth condition at 1000°C and 1200°C. This better arrangement of substrate atoms is believed to cause a decrease in surface energy. The terrace width is very stable and on the order of 250nm for the 1000°C-1200°C. In addition, the terrace height and roughness are almost the same for these two annealing temperatures. The nanosheet width is around 200nm, however there are no results that indicate that nanosheet width and terrace width are correlated. Nevertheless, the terrace width may have an impact on the growth. Terrace width equal to 250nm seems suitable for this growth.

Poor growth; un-annealed and 1400°C: Almost no nanosheets were observed for the un-annealed sample, see figure 8.3. It was shown in chapter 6 that there was a significant increase in the terrace height from un-annealed to annealed samples, 0.125nm to one atomic step of 0.25nm, respectively. This poor structural arrangement for un-annealed samples is believed to be the reason for the absence of nanosheets, as a consequence for the high surface energy. The roughness and poorly defined terrace steps are also believed to be a general trend which resulted in the low density of nanosheets.

The growth condition for the substrate annealed at 1400°C saw a reduction in nanosheet density, see figure 8.3(h). From the structural analysis of the annealed sapphire substrate in chapter 6, it was found that the terrace width doubled from 250nm to 490nm. This is a significant increase, which is believed to affect the nanosheet growth. The annealing temperature of 1400°C may therefore only act as an indirect parameter, which increases the width, which again affects the growth condition. This can be due to the step-and-flow growth mechanism explained in chapter 3. If the terrace width is increased, the adatoms deposited on the terrace have to diffuse further to reach the nanostructure or the terrace step. This can indicate the influence of the terrace width, where the growth mechanism is switched from step-and-flow towards island growth. Growths on this annealed substrate were carried out twice, at the second time it showed a little better growth density than for the first, but there was still a reduction in growth density,

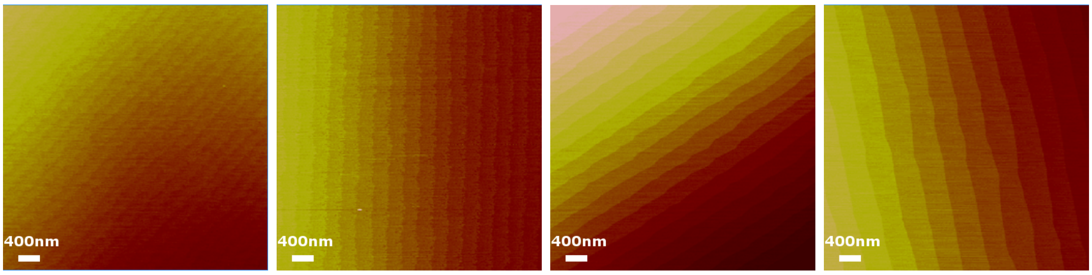

(a) unannealed (b) 1000°C (c) 1200°C (d) 1400°C

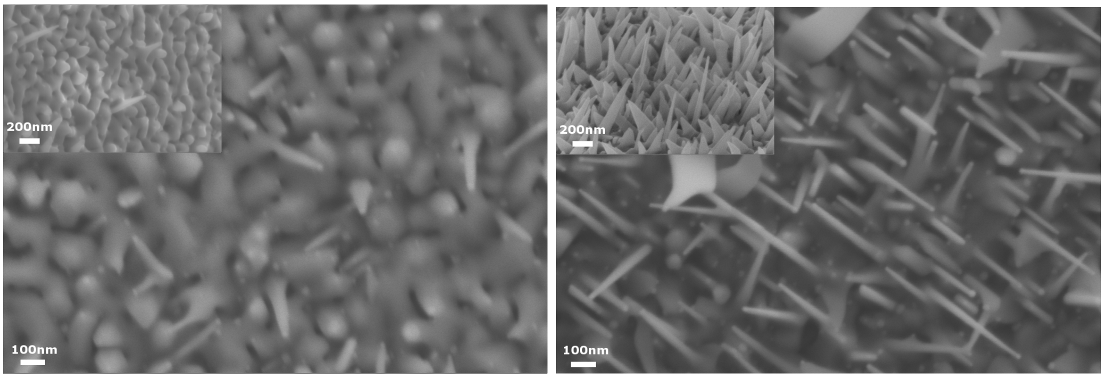

(e) unannealed (f) 1000°C

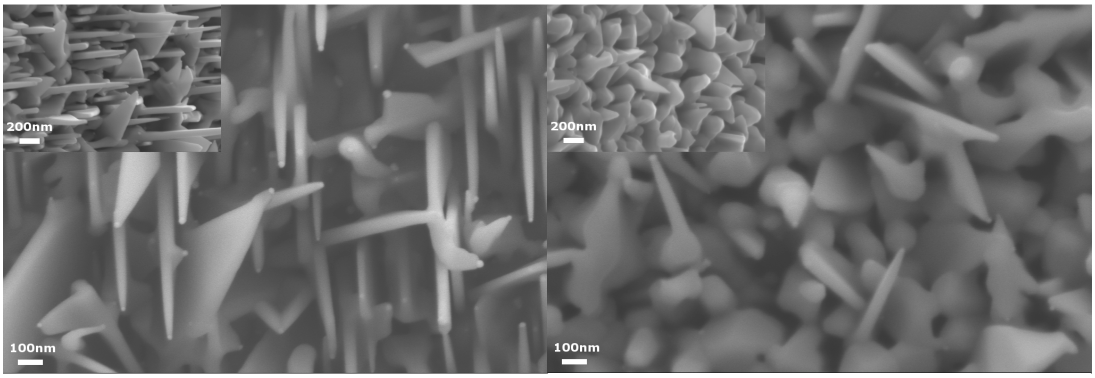

(g) 1200°C (h) 1400°C

Figure 8.3: (a)-(d) Sapphire surface after annealing. (e)-(h) 0°view of ZnO nanostructures grown on a-plane sapphire substrate. The substrate is annealed at different temperature before growth as noted in the subfigure text. The inset is a 45°tilted view. Magnification is 50kx.

see figure 8.5(a). The terrace width of the two samples was 490nm and 470nm, with the same terrace height (~ 0.25nm) and the same roughness (~ 0.06nm).

Nanosheets on c-plane

For ZnO nanostructures on c-plane sapphire, an optimal growth at substrate annealed at temperature 1200°C and 1400°C was found, see figure 8.4(g)-(h). As seen from the substrate surface imaged by AFM, the substrate has clear terrace structures, see figure 8.4(c)-(d). Terrace formation is often a criterion of good structural growth of thin films because of the smooth transition from the substrate atomic layer to the deposited film atomic layer, which leads to good bounding between adatoms and atoms.

Good growth; 1200°C and 1400°C: The terrace height and terrace roughness for these substrates are very similar. The terrace width is for the 1200°C sample around 500nm and for the 1400°C around 470nm. An additional sample with the substrate annealed at 1400°C and a terrace width equal to 160nm showed the same high nanosheet density, see figure 8.5(b). In this case it does not look like the terrace width is of interest, rather it is the presence of terraces. The sample annealed at 1200°C have more of an island type of topography, contrary to the more parallel formed terraces seen at the 1400°C annealed sample. These island terraces deviate a lot, and the mean terrace width has large standard deviation. These terrace structures seems very favorable for nanosheet growth as seen by the high density of nanosheets.

Poor growth; un-annealed and 1000°C: The rough samples of un-annealed and annealed at 1000°C c-plane sapphire did not contribute to a lot of statistical data, see figure 8.4(a)-(d). The only indication of terrace structures was seen on the sample annealed at 1000°C, which leads to the conclusion that terrace formations are needed for good nanosheet growth. The un-structured substrate surface is believed to be the main factor of the nearly absence of nanostructures. High surface energy can be a result of the rough substrate surface, since the surface atoms do not possess the least amount of energy in the lattice structure. While annealing the substrate, and thereby reducing the surface energy, a better growth condition is observed at annealed samples above 1200°C. In addition, a rough surface may cause the nanostructures to grow into each other, destroying the structures and creating more of a film instead of nanostructures. Nanosheets on these rough samples can therefore only grow uninterrupted on elevated topography where they are not interfered with any other sheets. This causes the low density of nanosheets.

Reproducibility

a-plane: Low nanosheet density for un-annealed samples was observed twice, and, according to theory, better growth conditions are expected on annealed samples. The less favorable growth environment for 1400°C compared to 1200°C is also believed to be the case, see figure 8.3(g)-(h). The density of the ZnO nanosheets grown on a sample annealed at 1150°C was very alike the density of nanosheets grown on a 1200°C annealed sample.

The experiment carried out the second time for substrate annealed at 1400°C showed a little better growth than the first results (see figure 8.5(a) and 8.6(d)). In the second experiment, only one sample was in the growth chamber during deposition, also the plasma plume was highly directed towards the sample. This resulted in a little higher density of nanosheets compared with the first experiment, but a decrease from the 1200°C annealed samples is seen. The better alignment of the plasma plume may have affected the growth, this cannot be concluded. Since it is seen, in general, a reduction of nanosheet growth from 1200°C to 1400°C, it is therefore concluded that this is a consequence of the substrate annealing treatment.

c-plane: Poor growth conditions and low nanosheet density were observed twice on un-annealed substrates. However, the first sample showed better growth than the second. In general, for

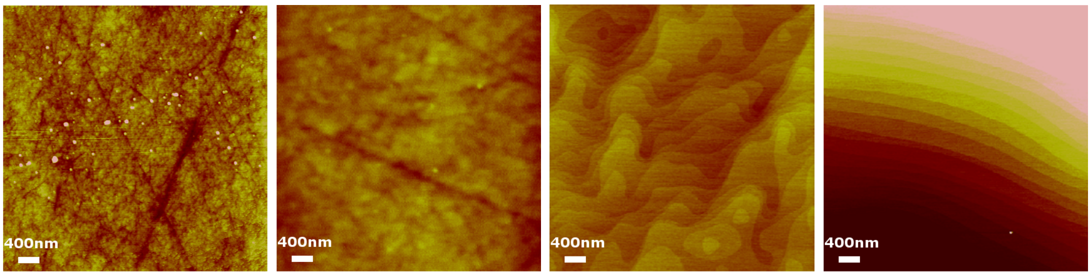

(a) unannealed (b) 1000°C (c) 1200°C (d) 1400°C

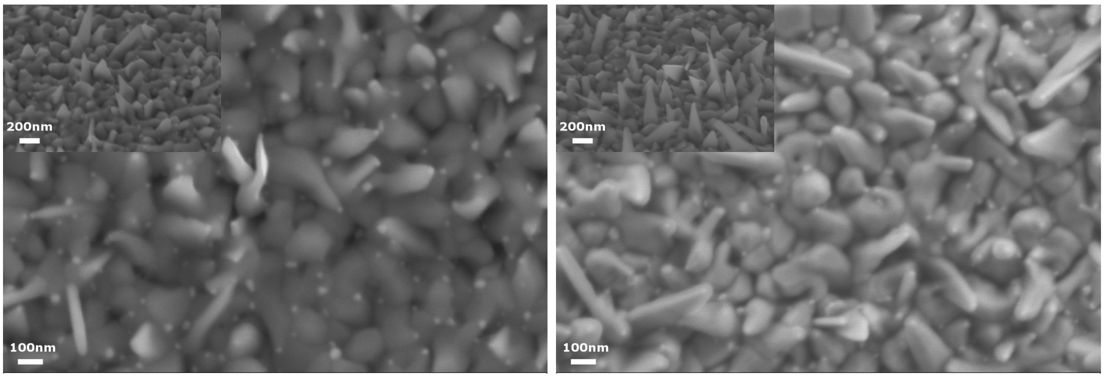

(e) unannealed (f) 1000°C

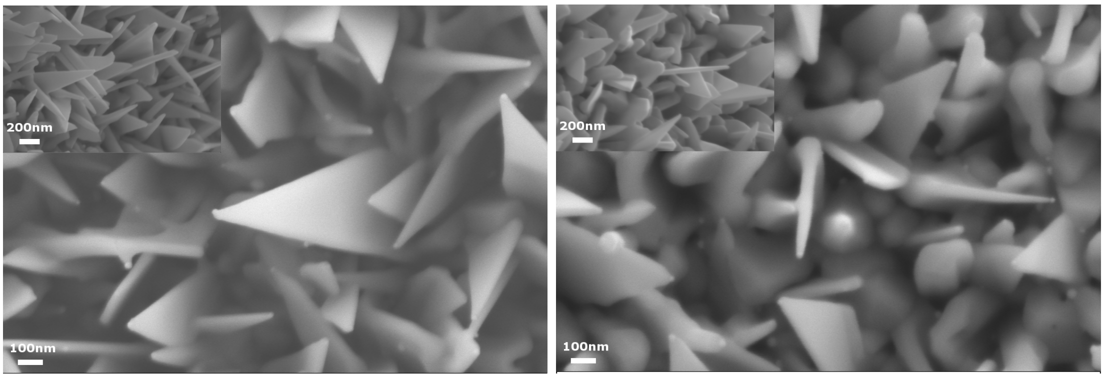

(g) 1200°C (h) 1400°C

Figure 8.4: (a)-(d) Sapphire surface after annealing. (e)-(h) 0°view of ZnO nanostructures grown on c-plane sapphire substrate. The substrate is annealed at different temperatures before growth as noted in the subfigure text. The inset is a 45°tilted view. Magnification is 50kx.

good nanosheet growth conditions, a substrate annealed at a temperature of around 1200°C and above increases the nanosheet density considerably. A sample annealed at 1150°C had a nanosheet density to be fitted between the nanosheets grown at 1000°C and nanosheets grown at 1200°C. A second sample annealed at 1400°C showed nearly reproducible nanosheet density similar to the first sample, see figure 8.5(b) and 8.6(d), respectively. These results are most likely reproducible.

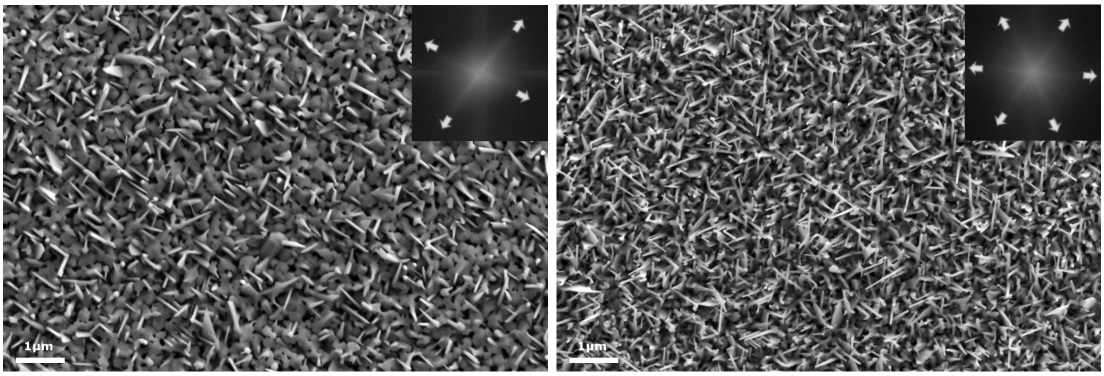

(a) 1400°C (b) 1400°C

Figure 8.5: Samples annealed at 1400°C, grown in the PLD separately with extra care taken regarding the plasma plume oriented towards the samples. (a) a-plane sapphire,(b) c-plane. Magnification is 10kx.

8.2.3 Alignment of Nanosheets

Characterization of nanostructures is far more complicated than characterization of thin films. XRD measures the preferred orientation of the surface structure and is an ideal method for characterizing the structure and orientation of products with respect to the substrate[85]. With low resolution XRD measurements it can be difficult to decide if the crystal structure is oriented differently for individual nanostructures as they are tilted and azimuthally aligned in different directions. Also for XRD scans of nanostructures compared to thin film, it is difficult to know if the XRD reflection comes from the nanostructure or the thin film layer around the nanostructures. This should be kept in mind when analyzing the XRD data. A way of deciding the azimuthally in-plane aligned nanosheets can be Fast Fourier Transform (FFT). When an image is filtered by FFT, information about the geometry of the spatial domain image is gained. The image in the Fourier domain is decomposed into its sinusoidal components, and therefore it is easy to examine certain frequencies of the image. This section has been categorized and divided into two parts, hence the substrates where we obtained no nanosheets and the substrates were we observed nanosheets. The no nanosheets category consists of a-plane un-annealed and annealed at 1400°C and c-plane un-annealed and annealed at 1000°C. The nanosheets category consists of a-plane 1000°C-1200°C and c-plane 1200°C-1400°C.

No Nanosheets

In this case more of a thin-film is deposited rather than nanosheet formation. It is believed that the growth mechanism is mainly controlled by the island mode, as seen in figure 3.4(b). Adatoms do not want to deposit onto the substrate and diffuse over the surface to find a more energetically favorable place. As there are no particular good positions, it nucleates to each other on the surface and forms islands. This is seen on the SEM pictures as small, cone-shaped thin film.

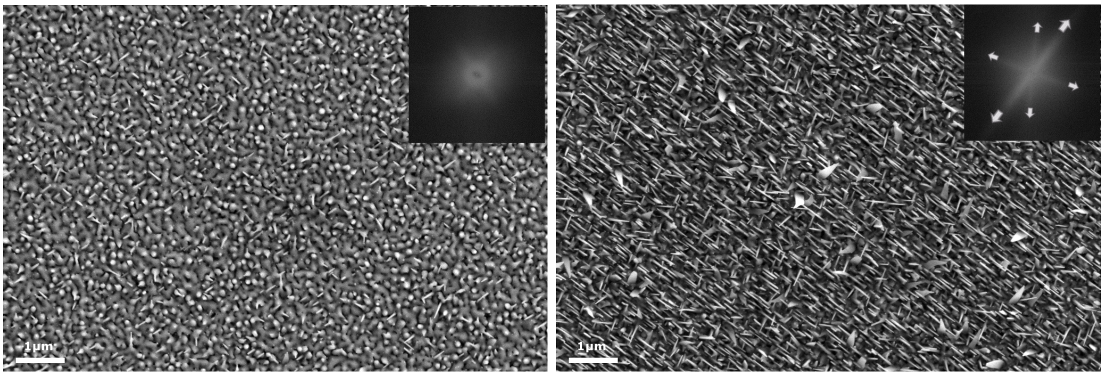

(a) unannealed (b) 1000°C

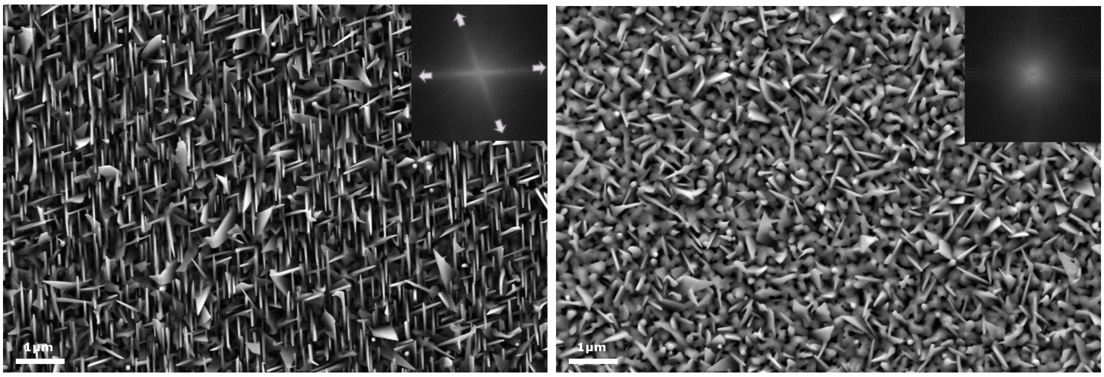

(c) 1200°C (d) 1400°C

Figure 8.6: 0°view of ZnO nanostructures grown on a-plane sapphire substrate. The substrate is annealed at different temperatures before growth as noted in the subfigure text. The inset is the FFT of the picture. Magnification is 10kx.

a-plane: Only blurred spots are seen from the FFT pictures inset in figure 8.6(a) and (d). A special case was observed for the second experiment at 1400°C where more nanostructures are shown. This is explained in more detail in the nanosheet section. The FFT pictures show only a round spot, which is an indication of no symmetry in the picture. Since more of a thin film is seen, it is expected that the FFT picture will not contribute to any new information. The XRD scan result of the surface is given in figure 8.8(a). It shows that for a-plane sapphire the preferred crystal orientation is $(0002)_{\text{ZnO}}$. This is expected since c-axis is commonly found as the fastest and best growth direction. In addition, there is also a crystal orientation of $(10\bar{1}1)_{\text{ZnO}}$. This is the second fastest growth direction of ZnO ($(0001)_{\text{ZnO}} > (10\bar{1}1)_{\text{ZnO}} > (10\bar{1}0)_{\text{ZnO}}$) [54]. It seems therefore reasonable to have thin film growth of these two crystal planes, where the preferred crystal growth direction, $(0001)_{\text{ZnO}}$, is seen as many orders higher than the second preferred growth direction, $(10\bar{1}1)_{\text{ZnO}}$.

c-plane: Blurred spots on the FFT pictures are also seen for the two nanosheet-free samples of c-plane, see inset in figure 8.7(a)-(b). This is an indication for the thin film island growth, where no nanosheet is seen and therefore no in-plane symmetry. The XRD measurements of the sample shows a clear indication of $(0001)_{\mathrm{ZnO}}$ growth followed by a lower intensity peak at $(10\bar{1}1)_{\mathrm{ZnO}}$, see figure 8.8(c). This is also expected.

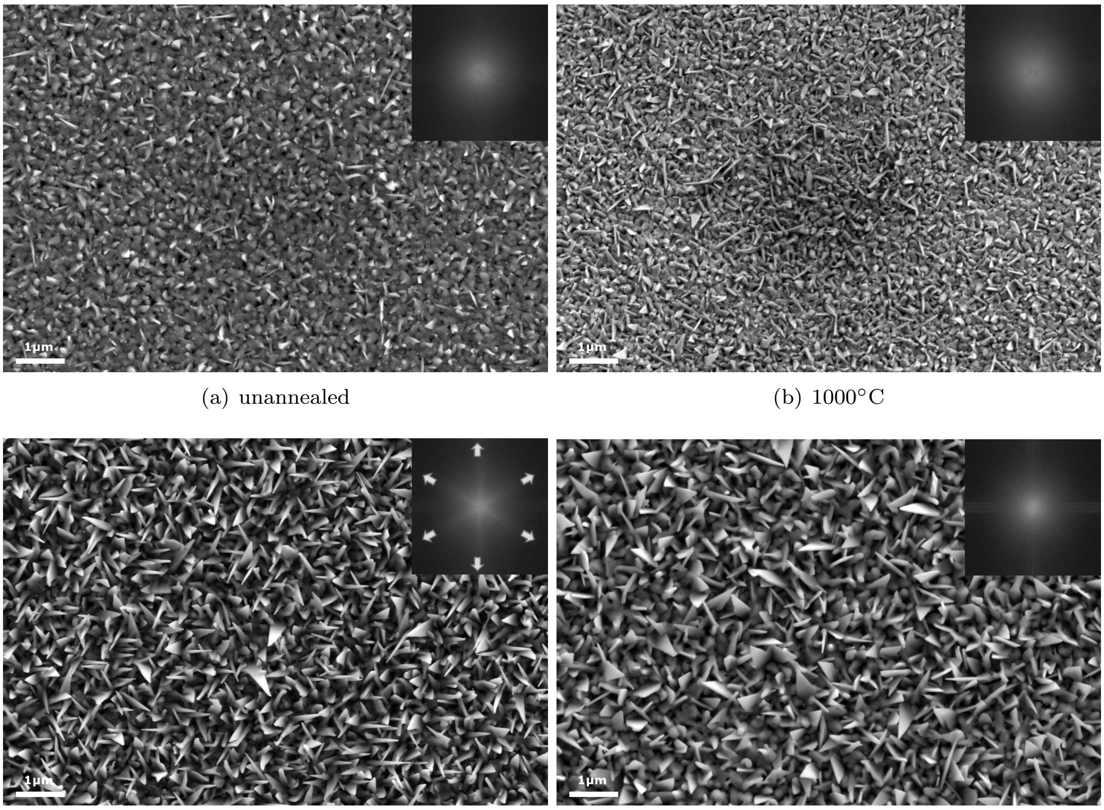

(a) unannealed

(b) 1000°C

(c) 1200°C

(d) 1400°C

Figure 8.7: 0°view of ZnO nanostructures grown on c-plane sapphire substrate. The substrate is annealed at different temperatures before growth as noted in the subfigure text. The inset is the FFT of the picture. Magnification is 10kx.

Nanosheets

The nanosheets grown on sapphire substrate were both tilted (with an inclination angle with respect to the surface) and azimuthally in-plane rotated. A much higher orientation was seen for the a-plane compared to the c-plane.

a-plane: Nanosheets on a-plane sapphire substrate are highly oriented in two directions with some exceptions, where it looks like they are either tilted an angle or azimuthally in-plane rotated. The azimuthally rotated nanosheets may follow the a-plane substrate lattice. From the inset of figure 8.6(b)-(c) the FFT of the spatial picture is given. It indicates a periodic pattern in the picture, which for the substrate annealed at 1000°C looks like a superposition between several orientations. For the substrate annealed at 1200°C it looks like a parallelogram geometry, which is also seen for the second experiment on the 1400°C annealed sample. A

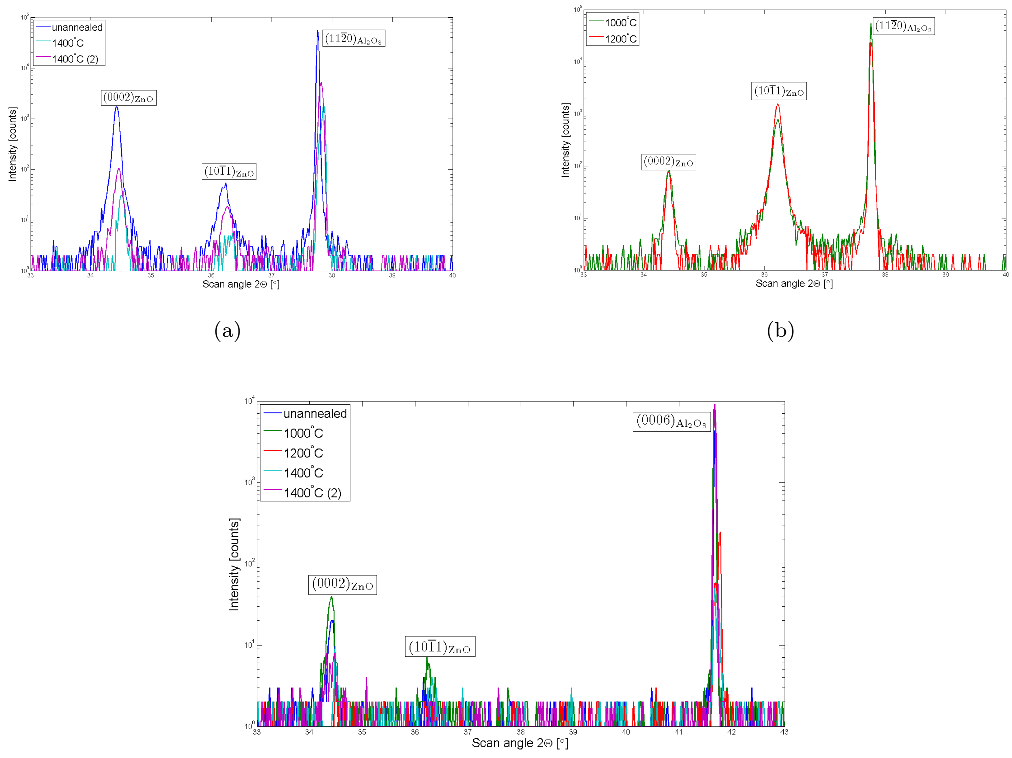

(a)

(b)

(c)

Figure 8.8: XRD scans of Au catalyst ZnO nanosheet growth on sapphire substrate. (a) a-plane sapphire substrate un-annealed and annealed at 1400°C. Poor nanosheet growth condition. (b) a-plane sapphire substrate annealed at 1000°C and 1400°C. Good nanosheet growth condition. (c) c-plane sapphire substrate un-annealed, annealed at 1000°C, 1200°C and 1400°C.

rotation of the parallelogram in the spatial domain results also in a rotation in the frequency domain, see figure 8.9. An angle of 90°between the beams in the FFT image would have resulted in a rectangle. This is not the case since the FFT images do not have 90°, which is an indication of a parallelogram orientation of the nanosheets in the spatial picture. A rectangular crystal plane is actually the case for a-plane $(11\bar{2}0)$ sapphire as seen in figure 6.1(b). The a-plane sapphire surface lattice is of a two-fold symmetry [86]. This is most likely the reason for the more oriented nanosheet alignment seen on a-plane substrate contrary to the c-plane. The substrate may therefore control the azimuthal alignment of the nanosheet. XRD scans of the nanosheets show that the crystal growth direction parallel to the substrate is mainly found to be in the $(10\bar{1}1)_{\mathrm{ZnO}}$ direction. Alignment parallel to the substrate means also that it is perpendicular to the PLD plasma plume. This is the second fastest growth plane and it would be interesting to locate the $(0001)_{\mathrm{ZnO}}$ growth direction for these types of grown nanosheets. One theory is that the $(0001)_{\mathrm{ZnO}}$ growth plane follows the VLS mechanism. As this is only a preliminary study, more research is needed. Possible characterization techniques could be a more exhaustive XRD scan and transmission electron microscopy (TEM) analysis, but also SEM analysis of a 90°tilted sample could be used to calculate the VLS growth direction. This could be done by measuring the tilt angle of the nanosheet and compare it with the angle between the $(10\bar{1}1)_{\mathrm{ZnO}}$ and the $(0001)_{\mathrm{ZnO}}$ plane.

In the XRD scan also a preferred growth direction of $(0001)_{\mathrm{ZnO}}$ was found. This means that the nanosheets grow in different crystal orientation, and more analysis is certainly needed. The intensity from the $(0001)_{\mathrm{ZnO}}$ plane was weaker than for the $(10\bar{1}1)_{\mathrm{ZnO}}$ plane for the nanosheet growth on a-plane sapphire, as seen in figure 8.8(b).

c-plane: Nanosheets do not align in the same manner on c-plane substrates as for a-plane substrates. It is seen from the pictures that the nanosheets are more tilted and more azimuthally in-plane rotated than for the a-plane (figure 8.7(c)-(d) and figure 8.6(b)-(c)). Nevertheless, from the FFT images, a six-fold symmetry is seen for the substrate annealed at 1200°C, and also in the second experiment at substrate annealing at 1400°C, see inset in figure 8.7(c) and 8.5(b). It is a very clear symmetry and it gives information about the azimuthal rotation of the nanosheets on c-plane sapphire. Exactly 60°between each beam in the FFT image indicates a hexagonal azimuthal orientation, which corresponds to the hexagonal c-plane of the sapphire substrate. This explains why the nanosheets look more misaligned than in the case of a-plane. A proposed alignment of ZnO nanosheets due to the different sapphire cut plane is shown in figure 8.9. This azimuthal orientation of c-plane was also seen by Park et al. when non-catalyst ZnO nanorods were grown on buffer layer by PLD [85].

The XRD scan showed a preferred growth direction in the $(0001)_{\mathrm{ZnO}}$ direction. Also a peak for the $(10\bar{1}1)_{\mathrm{ZnO}}$ direction was observed on c-plane sapphire substrate. This was lower than the peak at the $(0001)_{\mathrm{ZnO}}$ direction, contrary to the results obtain for the nanosheet growth on a-plane. It could be that the XRD scan results originate from the clamped area or the growth area between the ZnO nanosheets. It could also be that the nanosheets are oriented differently. To be further concluded, more characterization is needed.

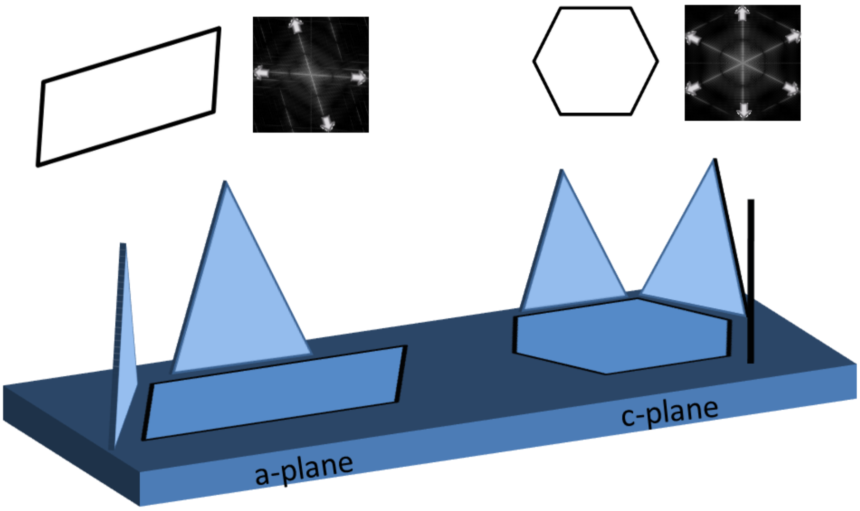

Figure 8.9: Proposed azimuthal in-plane alignment of nanosheets on a-plane and c-plane sapphire. This is mainly based on FFT analysis of annealed sapphire substrates. The FFT image of a four-sided parallelogram and a six-sided hexagon is shown above the nanosheets.

8.3 Conclusion

In this chapter it has been shown that annealed sapphire substrates improve the growth density of Au catalyst ZnO nanosheets. Good growth conditions have been found on a-plane sapphire, when the substrate have been annealed at a temperature of 1000°C and 1200°C prior to Au deposition and PLD. Also, good growth condition on c-plane sapphire have been found when substrates have been annealed at a temperature of 1200°C and 1400°C prior to Au deposition and PLD. This has been explained mainly by the improved substrate surface, where parameters such as terrace structure and surface smoothness have been the main factors of influence. Also, the sapphire cut plane (a- and c-plane) shows influence on the nanosheet alignment. Nanosheets grown on a-plane sapphire are more aligned than nanosheets grown on c-plane as a consequence of substrate crystal structure. Preliminary XRD scans have given an indication to how the ZnO crystal orientation is grown. Further work is needed in order to understand the growth mechanism of nanosheets.

Chapter 9

Conclusion

Influence of parameters prior to the pulsed laser deposition of ZnO has been investigated. Substrate orientation and annealing temperature were changed in order to control the growth parameters of ZnO nanostructures.

It has been found that annealing a- and c-plane sapphire substrates at high temperature (1000°C-1400°C) will form a terrace-and-step morphology with smooth surface. This terrace formation is different for a-plane and c-plane, since terrace-and-step morphology is observed already pre-annealed for a-plane. For c-plane, which is much rougher for un-annealed samples, a smooth surface with nice terrace-and-step is first observed at an annealing temperature of 1200°C. The c-plane sapphire surface was observed to transform from a rough sample to a terrace island formation and finally step-and-terrace formation with a uniform width. The terrace height was found to be around 0.25nm for a-plane annealed >1000°C and for c-plane annealed >1200°C. The terrace width was around 300nm.

Au droplets as a catalyst for the VLS growth mechanism has been investigated. Formation of Au droplets on a sapphire substrate is not a well-known mechanism. In this thesis a theory of thin film nucleation and Ostwald ripening has been accepted as an explanation. Since the Au droplets are very small, on order of 20nm in diameter, and formed on an insulating substrate, it has not been easy is characterize them by AFM and SEM. Measurements showed that they did not align towards the terrace structure of the annealed substrate. Different substrate annealing temperature did not show any correlation towards the Au droplets, where size and density was characterized. In-situ SEM imaging did not give any result due to the limit of the resolution.

As ZnO was deposited by PLD on the sapphire substrate at a temperature of 700°C, nanosheet formation was observed. The growth was mostly through VLS, but the VS mechanism has also been used as an explanation. The terrace-and-step morphology has shown to be very important to gain good Au catalyst nanosheet growth. High density of nanosheets was observed on a-plane substrates annealed at 1000°C and 1200°C, for c-plane high density of nanosheets was observed at substrate annealed at 1200°C and 1400°C. This increase in growth condition is concluded to be due to the substrate annealing treatment. In addition, the azimuthal in-plane alignment of nanosheets on a-plane seems to be correlated. This is most likely due to the two-fold symmetry on the a-plane sapphire substrate. Nanosheets on c-plane sapphire were azimuthally in-plane oriented in a six-fold symmetry, which were correlated to the hexagonal lattice structure of the sapphire substrate.

Future work

In this thesis it has been shown that substrate orientation and substrate annealing influence the ZnO nanostructure growth. It is therefore recommended for further work to anneal the substrate before Au catalyst deposition and PLD growth. This concerns both a-plane and c-plane sapphire substrates, and it should be done in order to improve the growth conditions of the nanostructures. In addition, investigating the substrate surface after annealing by AFM is important to know what kind of step-and-terrace morphology the substrate consists of. Investigating the substrate surface before ZnO growth is therefore recommended to be included in the experimental procedure for further work. This is, since the substrate surface most certain has an influence on the ZnO nanostructure growth.

In order to conclude on the growth mechanism for the nanosheets more sample analysis is needed. Investigating the preferred growth direction, in addition, understanding the VLS and VS growth mechanism better is important in order to control the growth parameters. Therefore investigating the nanostructures more closely with powerful characterization tools like TEM and XRD is important for further work. Also, the preliminary results on the proposed azimuthal in-plane alignment of the nanosheets should be confirmed by further characterization of more samples.

Bibliography

[1] George W. Crabtree and Nathan S. Lewis. Solar energy conversion. *Physics Today*, 60:37, 2007. `http://ptonline.aip.org/getpdf/servlet/GetPDFServlet?filetype=pdf&id=PHTOAD000060000003000037000001&idtype=cvips`.

[2] P. Ravirajan, D.D.C. Bradley, J. Nelson, S.A. Haque, J.R. Durrant, H.J.P. Smit, and J.M. Kroon. Efficient charge collection in hybrid polymer/TiO_2 solar cells using poly(ethylenedioxythiophene)/polystyrene sulphonate as hole collector. *Appl. Phys. Lett.*, 86:143101–1–3, 2005.

[3] D.C. Olson, J. Piris, R.T. Collins, S.E. Shaheen, and D.S. Ginley. Hybrid photovoltaic devices of polymer and ZnO nanofiber composites. *Thin Solid Films*, 496:26–29, 2006.

[4] D.C. Olson, S.E. Shaheen, M.S. White, W.J. Mitchell, M.F. AM van Hest, R.T. Collins, and D.S. Ginley. Band-offset engineering for enhanced open-circuit voltage in polymer-oxide hybrid solar cells. *Adv. Funct. Mater.*, 17:264–269, 2007.

[5] Monica Lira-Cantu and Frederik C. Krebs. Hybrid solar cells based on meh-ppv and thin film semiconductor oxides (TiO_2, Nb2o5, ZnO, CeO_2 and CeO_2-TiO_2): Performance improvement during long-time irradiation. *Solar Energy Materials and Solar Cells*, 90:2076 – 2086, 2006. `http://dx.doi.org/10.1016/j.solmat.2006.02.007`.

[6] Douglas B. Chrisey and Robert W. Eason. *Pulsed Laser Deposition of Thin Films.* Wiley & Sons, 2007.

[7] Min Guo, Peng Diao, and Shengmin Cai. Hydrothermal growth of perpendicularly oriented ZnO nanorod array film and its photoelectrochemical properties. *Applied Surface Science*, 249:71 – 75, 2005. `http://dx.doi.org/10.1016/j.apsusc.2004.11.053`.

[8] Yefan Chen, D. M. Bagnall, Hang jun Koh, Ki tae Park, Kenji Hiraga, Ziqiang Zhu, and Takafumi Yao. Plasma assisted molecular beam epitaxy of ZnO on c-plane sapphire: Growth and characterization. *Journal of Applied Physics*, 84:3912–3918, 1998. `http://dx.doi.org/10.1063/1.368595`.

[9] W.Y. Song, J.H. Yang, D.V. Dinh, T.I. Shin, S.M. Kang, S.-W. Kim, and D.H. Yoon. Vertical growth of Zno nanowires on c-al_2o_3 substrate by controlling ramping rate in a vapor-phase epitaxy method. *Journal of Physics and Chemistry of Solids*, 69:1486 – 1490, 2008. `http://dx.doi.org/10.1016/j.jpcs.2007.10.040`.

[10] Jiming Bao, Mariano A. Zimmler, Federico Capasso, Xiaowei Wang, and Z. F. Ren. Broadband ZnO single-nanowire light-emitting diode. *Nano Letters*, 6:1719–1722, 2006. `http://dx.doi.org/10.1021/nl061080t`.

[11] M. Law, L.E. Greene, J.C. Johnson, R. Saykally, and P. Yang. Nanowire dye-sensitized solar cells. *Nature Materials*, 4:455–459, 2005. `http://dx.doi.org/10.1038/nmat1387`.

[12] Zhiyong Fan and Jia G. Lu. Gate-refreshable nanowire chemical sensors. *Applied Physics Letters*, 86:123510, 2005. `http://dx.doi.org/10.1063/1.1883715`.

[13] Y.S. Lee and T.Y. Tseng. Correlation of grain boundary characteristics with electrical properties in ZnO-glass varistors. *J. Mater. Sci. Mater. Electron.*, 9:65, 1998.

[14] W. I. Park, J. S. Kim, G.-C. Yi, and H.-J. Lee. ZnO nanorod logic circuits. *Advanced Materials*, 17:1393–1397, 2005. `http://dx.doi.org/10.1002/adma.200401732`.

[15] Woong-Ki Hong, Dae-Kue Hwang, Il-Kyu Park, Gunho Jo, Sunghoon Song, Seong-Ju Park, Takhee Lee, Bong-Joong Kim, and Eric A. Stach. Realization of highly reproducible ZnO nanowire field effect transistors with n-channel depletion and enhancement modes. *Applied Physics Letters*, 90:243103, 2007. `http://dx.doi.org/10.1063/1.2748096`.

[16] Rolf Brendel, Jürgen H. Werner, and Hans J. Queisser. Thermodynamic efficiency limits for semiconductor solar cells with carrier multiplication. *Solar Energy Materials and Solar Cells*, 41-42:419 – 425, 1996. `http://dx.doi.org/10.1016/0927-0248(95)00125-5`.

[17] Martin A. Green, Keith Emery, Yoshihiro Hishikawa, and Wilhelm Warta. Solar cell efficiency tables (version 32). *Prog. Photovolt: Res. Appl.*, 16:435–440, 2008.

[18] Martin A. Green. Third generation photovoltaics: solar cells for 2020 and beyond. *Physica E: Low-dimensional Systems and Nanostructures*, 14:65 – 70, 2002. `http://dx.doi.org/10.1016/S1386-9477(02)00361-2`.

[19] Bauhuis GJ, Mulder P, Schermer JJ, HaverKamp EJ, van Deelen J, and Larsen PK. High efficiency thin film GaAs solar cells with improved radiation hardness. *20th European Photovoltaic Solar Energy Conference, Barcelona*, pages 468–471, 2005.

[20] J. F. Geisz, Sarah Kurtz, M. W. Wanlass, J. S. Ward, A. Duda, D. J. Friedman, J. M. Olson, W. E. McMahon, T. E. Moriarty, and J. T. Kiehl. High-efficiency GaInP/GaAs/InGaAs triple-junction solar cells grown inverted with a metamorphic bottom junction. *Applied Physics Letters*, 91:023502, 2007. `http://dx.doi.org/10.1063/1.2753729`.

[21] R.R. King, D.C. Law, K.M. Edmondson, C.M. Fetzer, G.S. Kinsey, H. Yoon, R.A. Sherif, and N.H. Karam. 40% efficient metamorphic GaInP/GaInAs/Ge multijunction solar cells. *Applied Physics Letters*, 90:183516–+, 2007. `http://dx.doi.org/10.1063/1.2734507`.

[22] Masakazu Ito, Kazuhiko Kato, Keiichi Komoto, Tetsuo Kichimi, and Kosuke Kurokawa. A comparative study on cost and life-cycle analysis for 100 mw very large-scale pv (vls-pv) systems in deserts using m-si, a-si, cdte, and cis modules. *Progress in Photovoltaics: Research and Applications*, 16:17–30, 2008. `http://dx.doi.org/10.1002/pip.770`.

[23] N. S. Sariciftci, L. Smilowitz, A. J. Heeger, and F. Wudl. Photoinduced Electron Transfer from a Conducting Polymer to Buckminsterfullerene. *Science*, 258:1474–1476, 1992. `http://dx.doi.org/10.1126/science.258.5087.1474`.

[24] G. Yu, J. Gao, J.C. Hummelen, F. Wudl, and A.J. Heeger. Polymer photovoltaic cells: Enhanced efficiencies via a network of internal donor-acceptor heterojunctions. *Science*, 270:1789–1791, 1995. `http://dns.ntu-ccms.ntu.edu.tw/references/SCIENCE-270-1789-1995.pdf`.

[25] Pavel Schilinsky, Christoph Waldauf, and Christoph J. Brabec. Recombination and loss analysis in polythiophene based bulk heterojunction photodetectors. *Applied Physics Letters*, 81:3885–3887, 2002. `http://dx.doi.org/10.1063/1.1521244`.

[26] F. Padinger, R.S. Rittberger, and N.S. Sariciftci. Effects of postproduction treatment on plastic solar cells. *Advanced Functional Materials*, 13:85–88, 2003. `http://dx.doi.org/10.1002/adfm.200390011`.

[27] Gang Li, Vishal Shrotriya, Jinsong Huang, Yan Yao, Tom Moriarty, Keith Emery, and Yang Yang. High-efficiency solution processable polymer photovoltaic cells by self-organization of polymer blends. *Nature Materials*, 4:864, 2005. `http://dx.doi.org/10.1038/nmat1500`.

[28] J. Y. Kim, S. H. Kim, H.-H. Lee, K. Lee, W. Ma, X. Gong, and A. J. Heeger. New architecture for high-efficiency polymer photovoltaic cells using solution-based titanium oxide as an optical spacer. *Advanced Materials*, 18:572–576, 2006. `http://dx.doi.org/10.1002/adma.200501825`.

[29] Jin Young Kim, Kwanghee Lee, Nelson E. Coates, Daniel Moses, Thuc-Quyen Nguyen, Mark Dante, and Alan J. Heeger. Efficient Tandem Polymer Solar Cells Fabricated by All-Solution Processing. *Science*, 317:222–225, 2007. `http://dx.doi.org/10.1126/science.1141711`.

[30] Brian A. Gregg. Excitonic solar cells. *The Journal of Physical Chemistry B*, 107:4688–4698, 2003. `http://dx.doi.org/10.1021/jp022507x`.

[31] Kevin M. Coakley and Michael D. McGehee. Conjugated polymer photovoltaic cells. *Chemistry of Materials*, 16:4533–4542, 2004. `http://dx.doi.org/10.1021/cm049654n`.

[32] M. Theander, A. Yartsev, D. Zigmantas, V. Sundström, W. Mammo, M. R. Andersson, and O. Inganäs. Photoluminescence quenching at a *polythiophene*/*c*60 heterojunction. *Phys. Rev. B*, 61:12957–12963, 2000. `http://dx.doi.org/10.1103/PhysRevB.61.12957`.

[33] C. J. Brabec N. S. Sariciftci, J. C. Hummelen. Plastic solar cells. *Advanced Functional Materials*, 11:15–26, 2001. `http://dx.doi.org/10.1002/1616-3028(200102)11:1<15::AID-ADFM15>3.0.CO;2-A`.

[34] University of Southern California Thompson Research Group. Organic solar cells. `http://met.usc.edu/` [Online 28.04.2009].

[35] C. G. Allen, D. J. Baker, J. M. Albin, H. E. Oertli, D. T. Gillaspie, D. C. Olson, T. E. Furtak, and R. T. Collins. Surface modification of ZnO using triethoxysilane-based molecules. *Langmuir*, 24:13393–13398, 2008. `http://dx.doi.org/10.1021/la802621n`.

[36] L. C. Tien, S. J. Pearton, D. P. Norton, and F. Ren. Synthesis and microstructure of vertically aligned ZnO nanowires grown by high-pressure-assisted pulsed-laser deposition. *Journal of Materials Science*, 43:6925–6932, 2008. `http://dx.doi.org/10.1007/s10853-008-2988-0`.

[37] R. S. Wagner and W. C. Ellis. Vapor-liquid-solid mechanism of single crystal growth. *Applied Physics Letters*, 4:89–90, 1964. `http://dx.doi.org/10.1063/1.1753975`.

[38] Seu Yi Li, Chia Ying Lee, and Tseung Yuen Tseng. Copper-catalyzed ZnO nanowires on silicon (1 0 0) grown by vapor-liquid-solid process. *Journal of Crystal Growth*, 247:357 – 362, 2003. `http://dx.doi.org/10.1016/S0022-0248(02)01918-8`.

[39] X.F. Duan and C.M. Lieber. General synthesis of compound semiconductor nanowires. *Advanced Materials*, 12:298, 2000. `http://dx.doi.org/10.1002/(SICI)1521-4095(200002)12:4<298::AID-ADMA298>3.0.CO;2-Y`.

[40] M. H. Huang, Y. Wu, H. Feick, N. Tran, E. Weber, and P. Yang. Catalytic growth of zinc oxide nanowires by vapor transport. *Advanced Materials*, 13:113–116, 2001. `http://dx.doi.org/10.1002/1521-4095(200101)13:2<113::AID-ADMA113>3.0.CO;2-H`.

[41] H. E. Okamoto. Au-zn (gold-zinc). *Journal of Phase Equilibria and Diffusion*, 27:427, 2006. `http://dx.doi.org/10.1007/s11669-006-0027-x`.

[42] J.C. Harmand, M. Tchernycheva, G. Patriarche, L. Travers, F. Glas, and G. Cirlin. GaAs nanowires formed by au-assisted molecular beam epitaxy: Effect of growth temperature. *Journal of Crystal Growth*, 301-302:853 – 856, 2007. `http://dx.doi.org/10.1016/j.jcrysgro.2006.11.106`.

[43] WangWang, Jinhui Song, Christopher J. Summers, Jae Hyun Ryou, Peng Li, Russell D. Dupuis, and Zhong L. Wang. Density-controlled growth of aligned ZnO nanowires sharing a common contact: A simple, low-cost, and mask-free technique for large-scale applications. *The Journal of Physical Chemistry B*, 110:7720–7724, 2006. `http://dx.doi.org/10.1021/jp060346h`.

[44] R.T. Rajendra Kumar, J. Grabowska, J.P. Mosnier, M.O. Henry, and E. McGlynn. Morphological control of ZnO nanostructures on silicon substrates. *Superlattices and Microstructures*, 42:337 – 342, 2007. `http://dx.doi.org/10.1016/j.spmi.2007.04.077`.

[45] V. E. Sandana, D. J. Rogers, F. H. Teherani, R. McClintock, M. Razeghi, H.-J. Drouhin, M. C. Clochard, V. Sallet, G. Garry, and F. Fayoud. MOCVD growth of ZnO nanostructures using au droplets as catalysts. *Zinc Oxide Materials and Devices III*, 6895:68950Z, 2008. `http://dx.doi.org/10.1117/12.775632`.

[46] K. Mergenthaler, V. Gottschalch, J. Bauer, H. Paetzelt, and G. Wagner. Growth and characterization of ZnO nanostructures on sapphire substrates. *Journal of Crystal Growth*, 310(23):5134 – 5138, 2008. `http://dx.doi.org/10.1016/j.jcrysgro.2008.08.004`.

[47] H. E. Okamoto. Al-Au (aluminum-gold). *Journal of Phase Equilibria and Diffusion*, 26:391–393, 2005. `http://dx.doi.org/10.1007/s11669-005-0098-0`.

[48] Ph. Buffat and J-P. Borel. Size effect on the melting temperature of gold particles. *Phys. Rev. A*, 13:2287–2298, 1976. `http://dx.doi.org/10.1103/PhysRevA.13.2287`.

[49] Lisheng Wang, Xiaozhong Zhang, Songqing Zhao, Guoyuan Zhou, Yueliang Zhou, and Junjie Qi. Synthesis of well-aligned ZnO nanowires by simple physical vapor deposition on c-oriented ZnO thin films without catalysts or additives. *Applied Physics Letters*, 86:024108, 2005. `http://dx.doi.org/10.1063/1.1851607`.

[50] Mingxia Qiu, Zhizhen Ye, Jianguo Lu, Haiping He, Jingyun Huang, Liping Zhu, and Binghui Zhao. Growth and properties of ZnO nanorod and nanonails by thermal evaporation. *Applied Surface Science*, 255:3972 – 3976, 2009. `http://dx.doi.org/10.1016/j.apsusc.2008.10.093`.

[51] Augustinus Josephus Helena Maria Rijnders. *The initial growth of complex oxides : study and manipulation*. PhD thesis, University of Twente, October 2001. `http://doc.utwente.nl/58102/`.

[52] Raghvendra S. Yadav and Avinash C. Pandey. Needle-like ZnO nanostructure synthesized by organic-free hydrothermal process. *Physica E: Low-dimensional Systems and Nanostructures*, 40:660 – 663, 2008. `http://dx.doi.org/10.1016/j.physe.2007.08.087`.

[53] Chennupati Jagadish and Stephen J. Pearton. *Zinc oxide bulk, thin films and nanostructures.* Elsevier, 2006.

[54] R. A. Laudise and A. A. Ballman. Hydrothermal synthesis of zink oxide and zink sulfide. *The Journal of Physical Chemistry*, 64:688–691, 1960. `http://dx.doi.org/10.1021/j100834a511`.

[55] Michael Quirk and Julian Serda. *Semiconductor manufacturing Technology.* Prentice Hall, 2001.

[56] Max Knoll. Aufladepotentiel und sekundaremission elektronenbestrahlter korper. *Zeitschrift für technische Physik*, 16:467–475, 1935.

[57] K. D. Vernon-Parry. Scanning electron microscopy: an introduction. *III-Vs Review*, 13:40 – 44, 2000. `http://dx.doi.org/10.1016/S0961-1290(00)80006-X`.

[58] G. Binnig, C. F. Quate, and Ch. Gerber. Atomic force microscope. *Phys. Rev. Lett.*, 56:930–933, 1986. `http://dx.doi.org/10.1103/PhysRevLett.56.930`.

[59] J. Thornton. *SPM Training Notebook.* Copyright © 2003 Veeco Instruments Inc., 2003.

[60] Charles Kittel. *Introduction to Solid State Physics.* John Wiley & Sons, 2005.

[61] Tudor E. Jenkins. *Semiconductor Science: Growth and characterization techniques.* Prentice Hall, 1995.

[62] K. Ariga and H.S. Nalwa, editors. *Bottom-up Nanofabrication: Supramolecules, Self-Assemblies and Organized Films*, chapter Pulsed laser deposition of nanostructured semiconductors. American Scientific, CA, 2007.

[63] S H Dalal, D L Baptista, K B K Teo, R G Lacerda, D A Jefferson, and W I Milne. Controllable growth of vertically aligned zinc oxide nanowires using vapour deposition. *Nanotechnology*, 17:4811–4818, 2006. `http://stacks.iop.org/0957-4484/17/4811`.

[64] Yinzhen Wang, Shunquan Wang, Shengming Zhou, Jun Xu, Jiandong Ye, Shulin Gu, Rong Zhang, and Qiushi Ren. Effects of sapphire substrate annealing on ZnO epitaxial films grown by mocvd. *Applied Surface Science*, 253:1745–1747, 2006.

[65] Jung-Hae Choi, Doh-Yeon Kim, Bernard J. Hockey, Sheldon M. Wiederhorn, Carol A. Handwerker, John E. Blendell, W. Craig Carter, and Andrew R. Roosen. Equilibrium shape of internal cavities in sapphire. *Journal of the American Ceramic Society*, 80:62–68, 1997. `http://dx.doi.org/10.1111/j.1151-2916.1997.tb02791.x`.

[66] Kamen Simeonov and David Lederman. Surface structure of $(11\bar{2}0)$ Al_2O_3 single crystals after high temperature annealing. *Surface Science*, 603, 2009. `http://dx.doi.org/10.1016/j.susc.2008.11.015`.

[67] H. Bialas and H.J. Stolz. Lattice dynamics of sapphire (corundum) part i: Phonon dispersion by inelastic neutron scattering. *Z. Physik B*, 21:319–324, 1975.

[68] Substrate technology. `http://www.substratestech.com/` [Online 28.04.2009].

[69] Yu Shiratsuchi, Masahiko Yamamoto, and Yasuhiro Kamada. Surface structure of self-organized sapphire (0001) substrates with various inclined angles. *Jpn. J. Appl. Phys.*, 41:5719–5725, 2002. `http://dx.doi.org/10.1143/JJAP.41.5719`.

[70] S. Tabuchi, H. Tabata, and T. Kawai. Sputtering and annealing effect of sapphire substrate for an orientation of lead phthalocyanine films. *Surface Science*, 571:117 – 127, 2004. `http://dx.doi.org/10.1016/j.susc.2004.08.016`.

[71] K.G. Saw. Effect of diffusion length on the nucleation of chemical vapour deposition diamond. *Surface Science*, 601, 2007. `http://dx.doi.org/10.1016/j.susc.2007.06.052`.

[72] O. Kurnosikov, L. Pham Van, and J. Cousty. About anisotropy of atomic-scale height step on (0001) sapphire surface. *Surface Science*, 459:256 – 264, 2000.

[73] J. Cui, A. Sun, M. Reshichkov, F. Yun, A. Baski, and H. Morkoç. Preparation of sapphire for high quality iii-nitride growth. *MRS Internet Journal Research Nitride Semiconductor*, 5, 2000.

[74] M. Yoshimoto, T. Maeda, T. Ohnishi, H. Koinuma, O. Ishiyama, M. Shinohara, M. Kubo, R. Miura, and A. Miyamoto. Atomic-scale formation of ultrasmooth surfaces on sapphire substrates for high-quality thin-film fabrication. *Applied Physics Letters*, 67:2615–2617, 1995. `http://dx.doi.org/10.1063/1.114313`.

[75] M. Yoshimoto, M. Furusawa, K. Nakajima, M. Takakura, and Y. Hishitani. Diamond film growth in an oxygen atmosphere. *Diamond and Related Materials*, 10:295 – 299, 2001. `http://dx.doi.org/10.1016/S0925-9635(00)00485-4`.

[76] G. H. Lee and H. N. Aiyer. Initial growth behaviour of linbo3 films on [alpha]-al2o3 substrates with atomic scale step structure. *Solid State Communications*, 118:441 – 444, 2001. `http://dx.doi.org/10.1016/S0038-1098(01)00148-X`.

[77] Primoz Rebernik Ribic and Gvido Bratina. Behavior of the (0001) surface of sapphire upon high-temperature annealing. *Surface Science*, 601:44 – 49, 2007. `http://dx.doi.org/10.1016/j.susc.2006.09.003`.

[78] Yang Gan, Erica J. Wanless, and George V. Franks. Lattice-resolution imaging of the sapphire (0001) surface in air by afm. *Surface Science*, 601:1064–1071, 2007.

[79] K. Yoshida, M. Yoshimoto, K. Sasaki, T. Ohnishi, T. Ushiki, J. Hitomi, S. Yamamoto, and M. Sigeno§. Fabrication of a new substrate for atomic force microscopic observation of dna molecules from an ultrasmooth sapphire plate. *Biophysical Journal*, 74:1654–1657, 1998.

[80] JEOL Serving Advanced Technology. *Manual: Speciment heating device.*

[81] Y K Mishra, S Mohapatra, D Kabiraj, A Tripathi, J C Pivin, and D K Avasthi. Growth of au nanostructures by annealing electron beam evaporated thin films. *Journal of Optics A: Pure and Applied Optics*, 9:410–414, 2007. `http://stacks.iop.org/1464-4258/9/S410`.

[82] Vladimir Sivakov, Frank Heyroth, Fritz Falk, Gudrun Andrä, and Silke Christiansen. Silicon nanowire growth by electron beam evaporation: Kinetic and energetic contributions to the growth morphology. *Journal of Crystal Growth*, 300:288 – 293, 2007. `http://dx.doi.org/10.1016/j.jcrysgro.2006.11.329`.

[83] Hila Sadan and Wayne D. Kaplan. Au–sapphire (0001) solid–solid interfacial energy. *Journal of Materials Science*, 41:5099–5107, 2006. `http://dx.doi.org/10.1007/s10853-006-0437-5`.

[84] Akane Kinjo, Hiroki Okuyama, Nobuyuki Iwata, and Hiroshi Yamamoto. Preparation of nano-structured c_{60} thin films. *Japanese Journal of Applied Physics*, 44:736–738, 2005. `http://jjap.ipap.jp/link?JJAP/44/736/`.

[85] Dong Jun Park, Dong Chan Kim, Jeong Yong Lee, and Hyung Koun Cho. Synthesis and microstructural characterization of growth direction controlled ZnO nanorods using a buffer layer. *Nanotechnology*, 17:5238–5243, 2006. `http://stacks.iop.org/0957-4484/17/5238`.

[86] M.Y. Chern, Y.C. Huang, and W.L. Xu. A-plane sapphire: A well-matched substrate for epitaxial growth of indium tin oxide. *Thin Solid Films*, 515:7866 – 7869, 2007. `http://dx.doi.org/10.1016/j.tsf.2007.04.023`.

Appendix A

All annealing results

A.1 a-Plane

Un-annealed

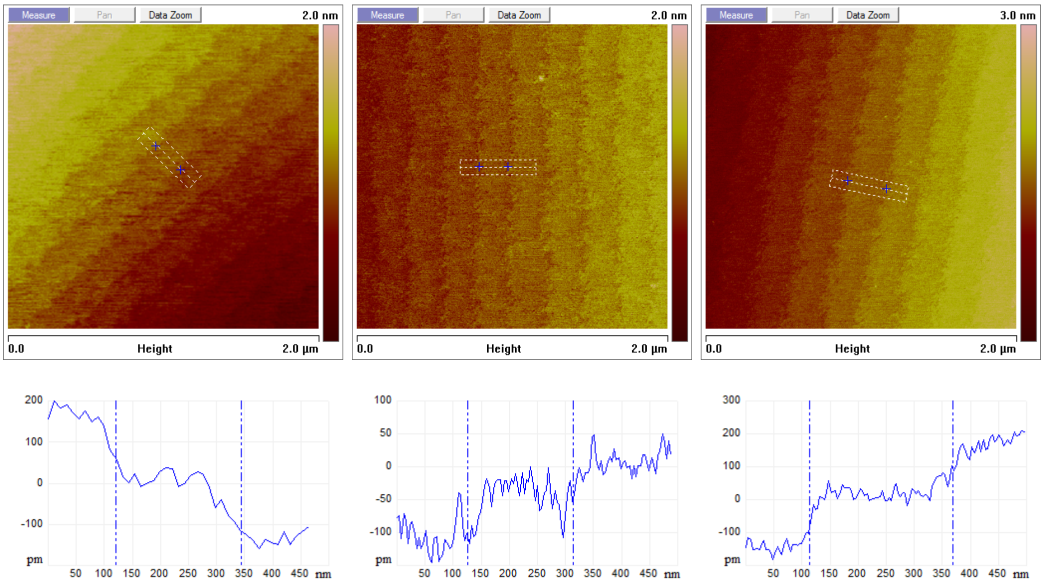

(a) a51 (b) a52 (c) a53

Figure A.1: AFM picture of un-annealed a-plane sapphire substrate

a-Plane: 1000°C

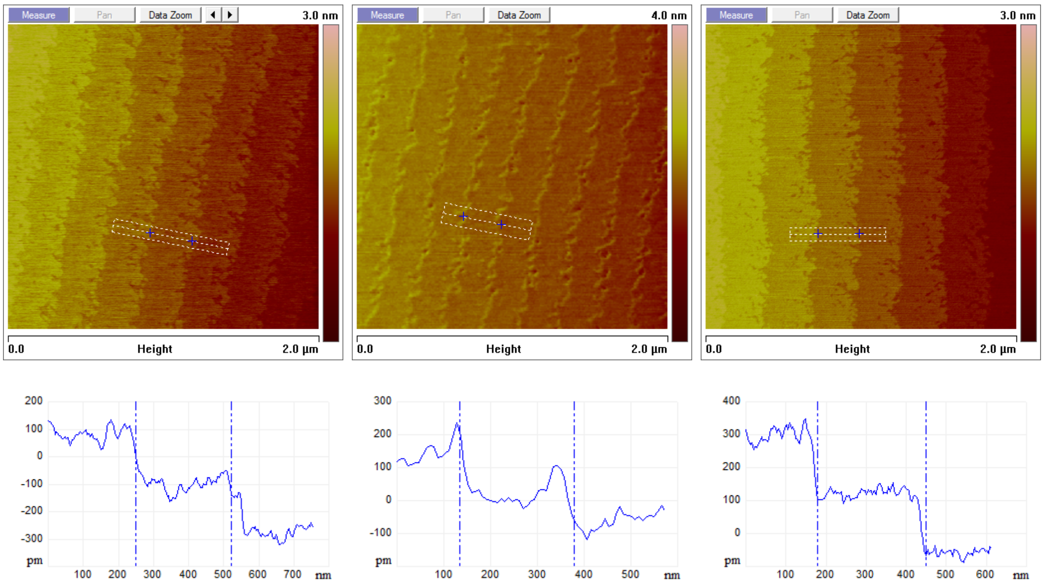

(a) a10 (b) a11 (c) a12

Figure A.2: AFM picture of a-plane sapphire substrate annealed at 1000°C.

a-Plane: 1200°C

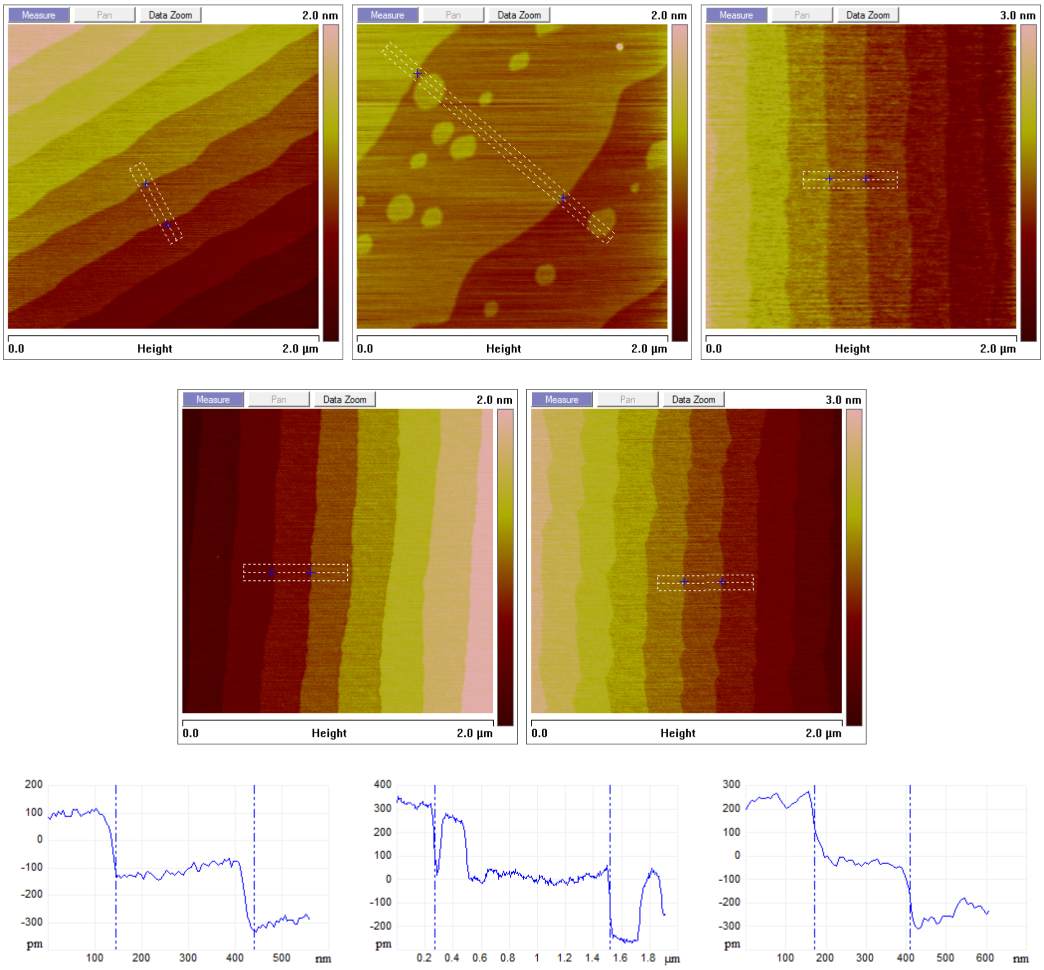

(a) a21 (b) a22 (c) a23

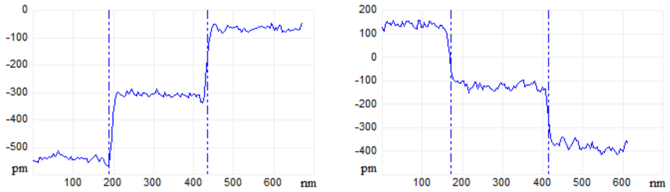

(d) a24 (e) a25

Figure A.3: AFM picture of a-plane sapphire substrate annealed at 1200°C.

a-Plane: 1400°C

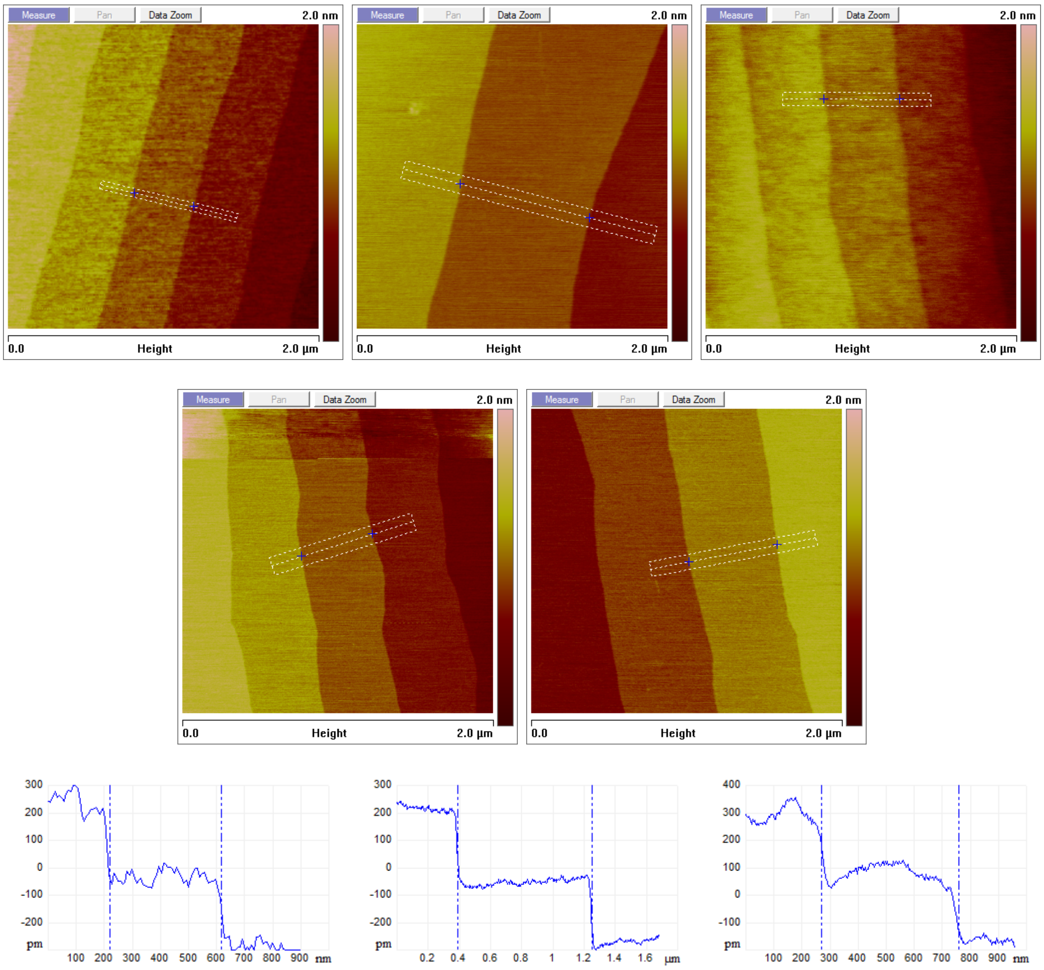

(a) a31 (b) a32 (c) a33

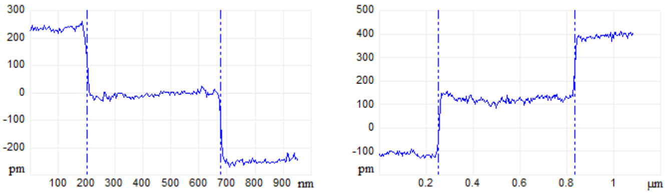

(d) a34 (e) a35

Figure A.4: AFM picture of a-plane sapphire substrate annealed at 1400°C.

A.2 c-Plane

Un-annealed

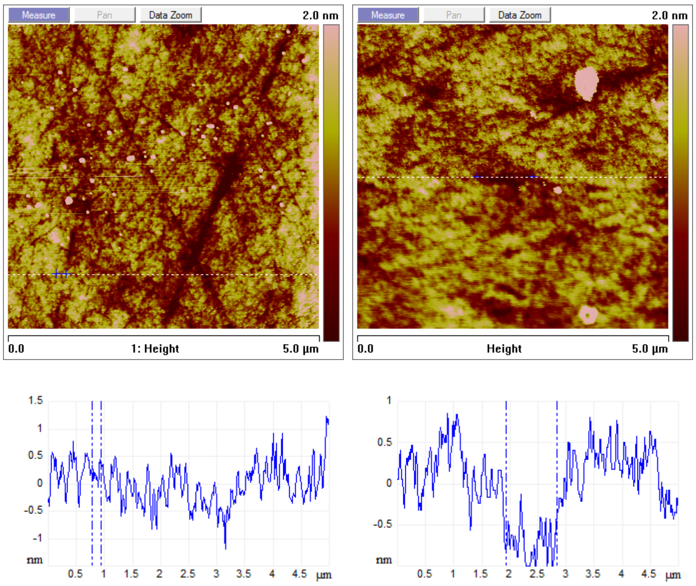

(a) c55 (b) c52

Figure A.5: AFM picture of un-annealed c-plane sapphire substrate.

c-Plane: 1000°C

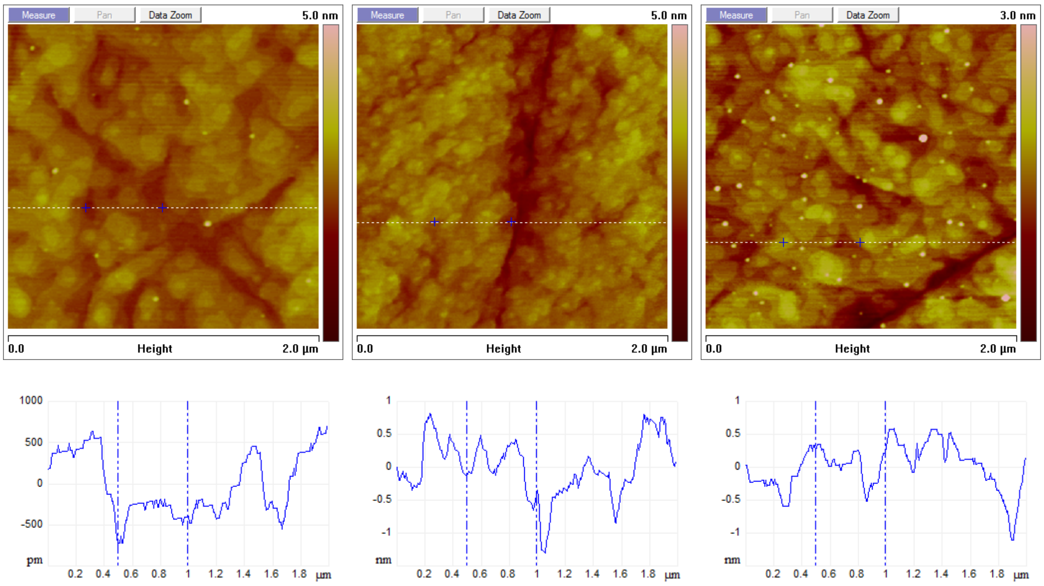

(a) c10 (b) c11 (c) c12

Figure A.6: AFM picture of c-plane sapphire substrate annealed at 1000°C.

c-Plane: 1200°C

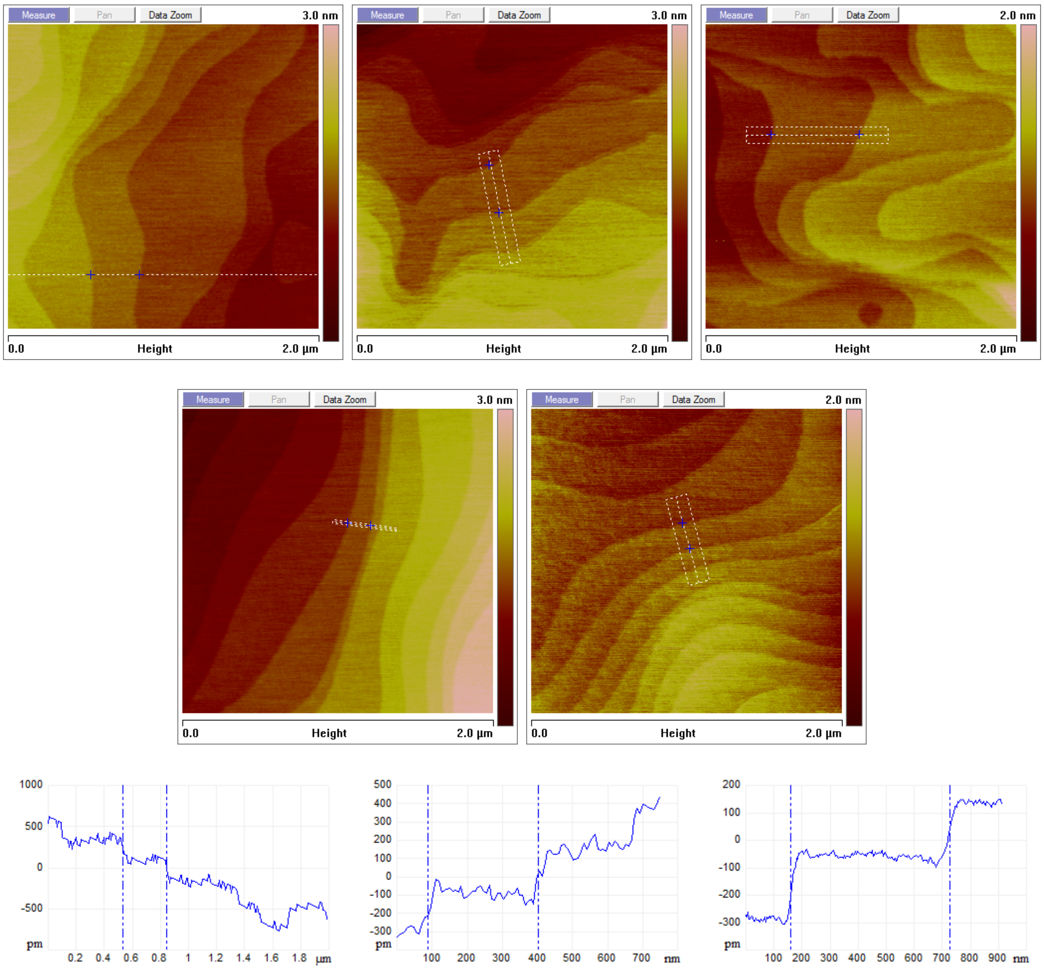

(a) c21 (b) c22 (c) c23

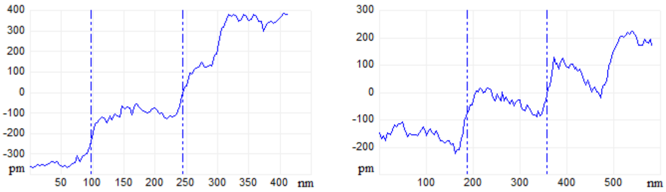

(d) c24 (e) c25

Figure A.7: AFM picture of c-plane sapphire substrate annealed at 1200°C.

c-Plane: 1400°C

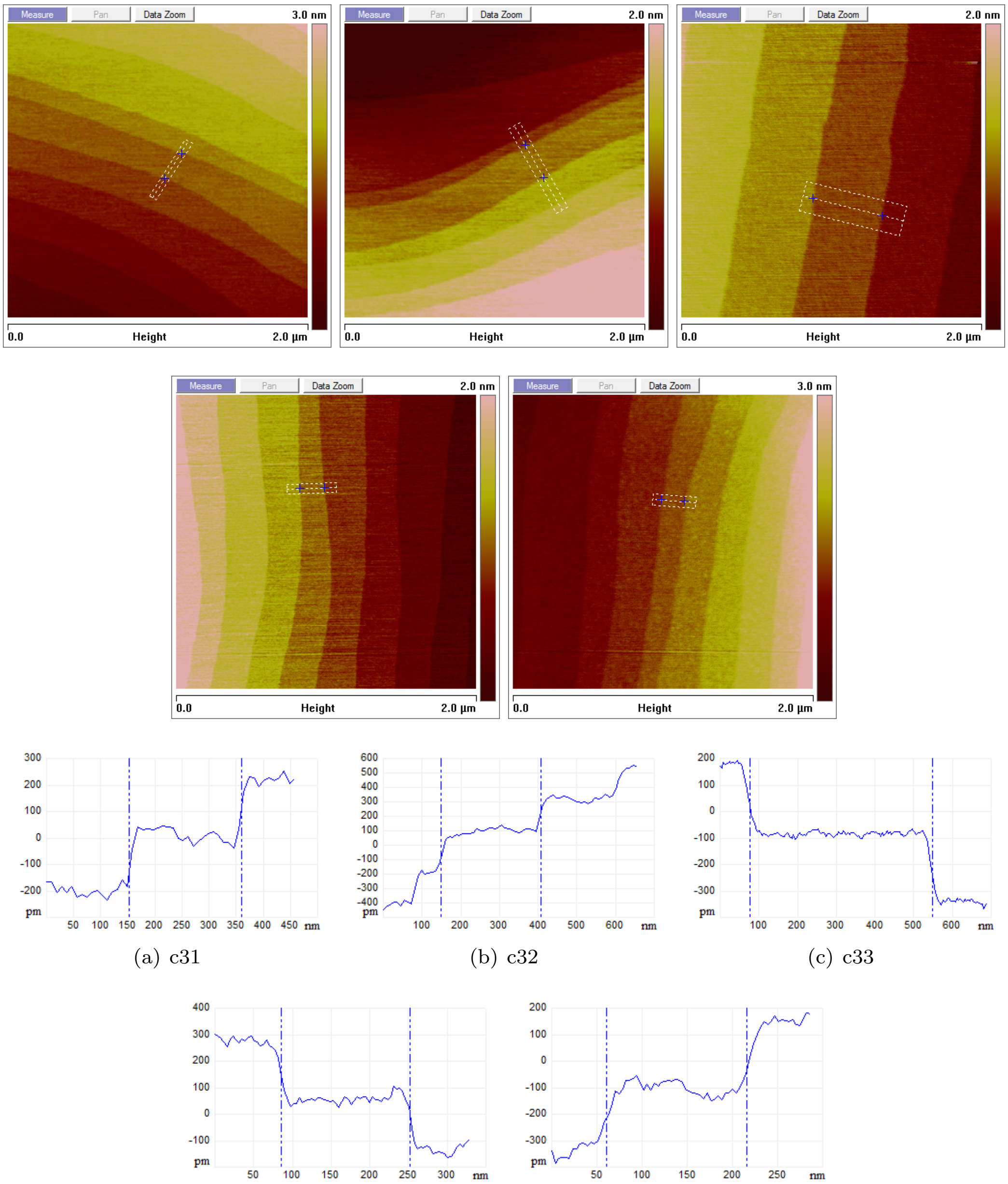

(a) c31 (b) c32 (c) c33

(d) c34 (e) c35

Figure A.8: AFM picture of c-plane sapphire substrate annealed at 1400°C.

			AFM			
Plane	Annealing temp.	Sample	1μm	2μm	5μm	10μm
a-plane	0°C	a51	x	x	x	
a-plane	0°C	a52	x	x	x	
a-plane	0°C	a53		x		
a-plane	1000°C	a10	x	x	x	
a-plane	1000°C	a11	x	x	x	x
a-plane	1000°C	a12	x	x	x	x
a-plane	1200°C	a21	x	x	x	x
a-plane	1200°C	a22	x	x	x	x
a-plane	1200°C	a23		x		
a-plane	1200°C	a24	x	x	x	
a-plane	1200°C	a25	x	x	x	x
a-plane	1400°C	a31	x	x	x	x
a-plane	1400°C	a32	x	x	x	x
a-plane	1400°C	a33	x	x	x	x
a-plane	1400°C	a34	x	x	x	x
a-plane	1400°C	a35	x	x	x	x
c-plane	0°C	c4	x		x	
c-plane	0°C	c52	x	x	x	x
c-plane	1000°C	c10	x	x	x	x
c-plane	1000°C	c11		x	x	
c-plane	1000°C	c12		x	x	
c-plane	1200°C	c21	x	x	x	x
c-plane	1200°C	c22		x	x	x
c-plane	1200°C	c23	x	x	x	x
c-plane	1200°C	c24	x	x	x	x
c-plane	1200°C	c25		x	x	x
c-plane	1400°C	c31	x	x	x	x
c-plane	1400°C	c32		x	x	x
c-plane	1400°C	c33	x	x	x	x
c-plane	1400°C	c34	x	x	x	x
c-plane	1400°C	c35	x	x	x	x

Table A.1: Characterization summary of annealed sapphire substrate.

Appendix B

All Au droplets results

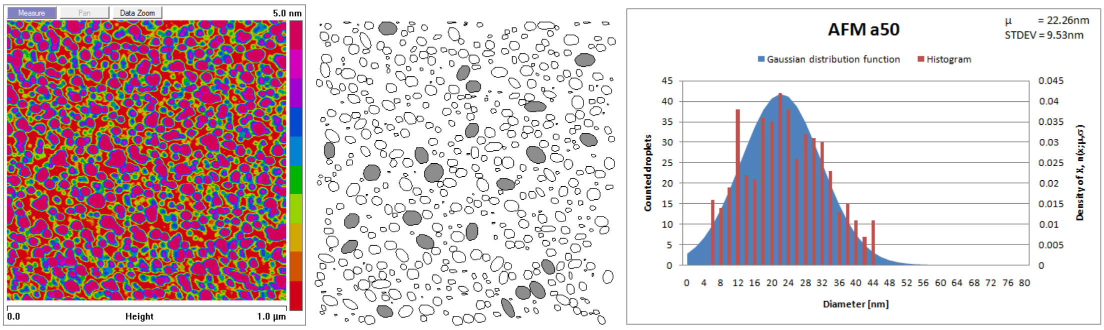

(a) (b) (c)

Figure B.1: AFM picture of Au droplets on un-annealed a-plane sapphire substrate.

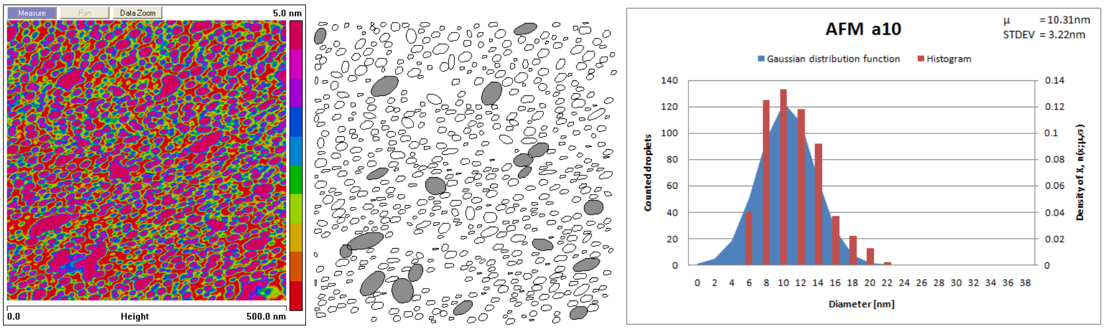

(a) (b) (c)

Figure B.2: AFM picture of Au droplets on a-plane sapphire substrate annealed at 1000°C.

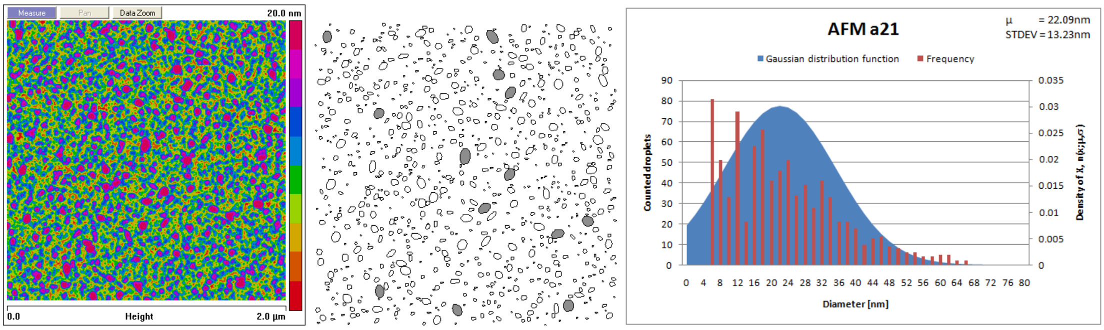

(a) (b) (c)

Figure B.3: AFM picture of Au droplets on a-plane sapphire substrate annealed at 1200°C.

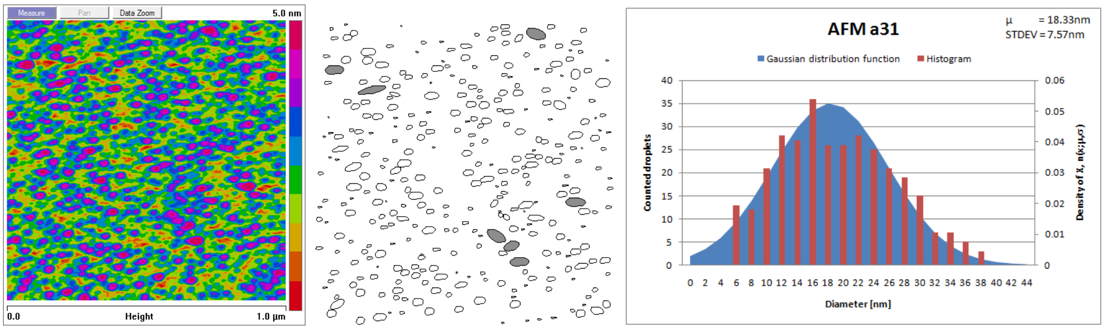

(a) (b) (c)

Figure B.4: AFM picture of Au droplets on a-plane sapphire substrate annealed at 1400°C.

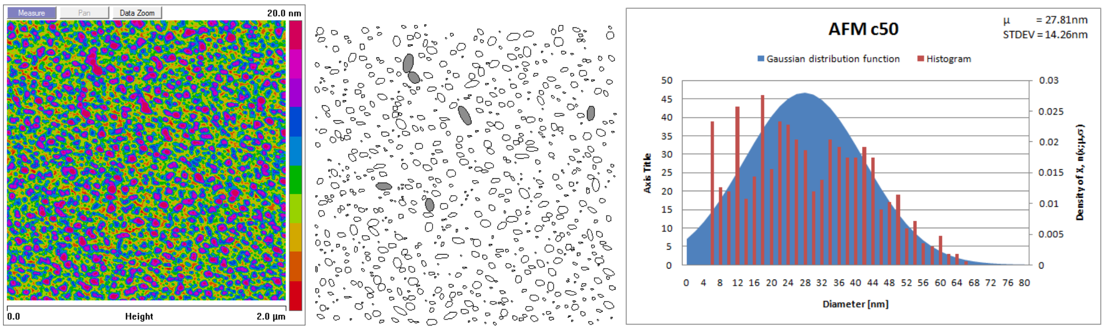

(a) (b) (c)

Figure B.5: AFM picture of Au droplets on un-annealed c-plane sapphire substrate.

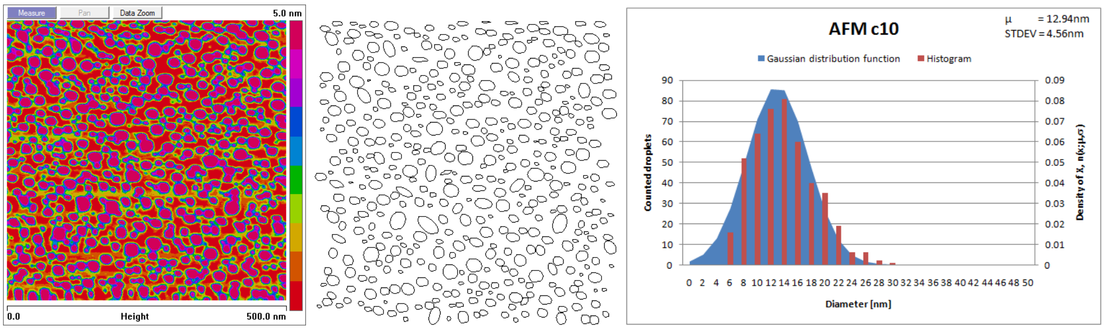

(a) (b) (c)

Figure B.6: AFM picture of Au droplets on c-plane sapphire substrate annealed at 1000°C.

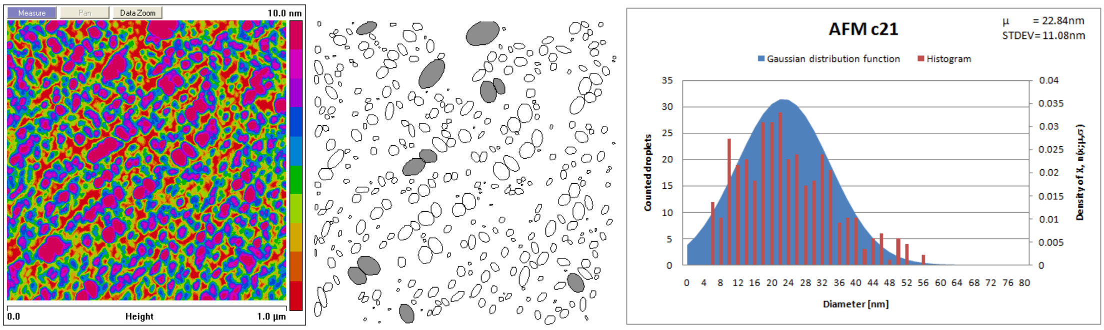

(a) (b) (c)

Figure B.7: AFM picture of Au droplets on c-plane sapphire substrate annealed at 1200°C.

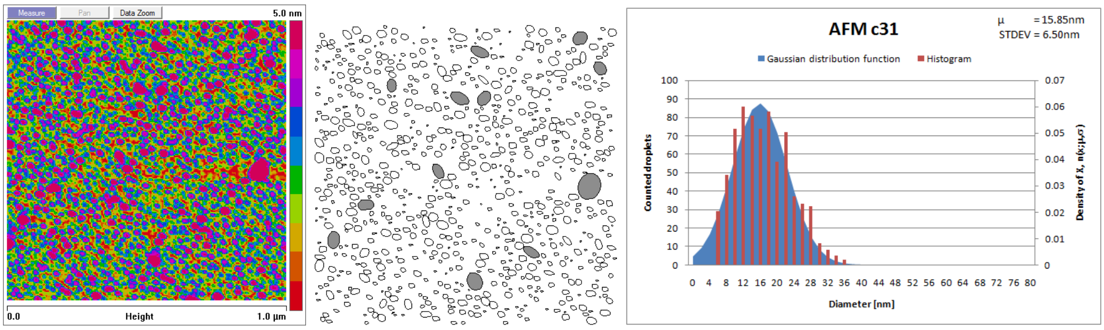

(a) (b) (c)

Figure B.8: AFM picture of Au droplets on c-plane sapphire substrate annealed at 1400°C.

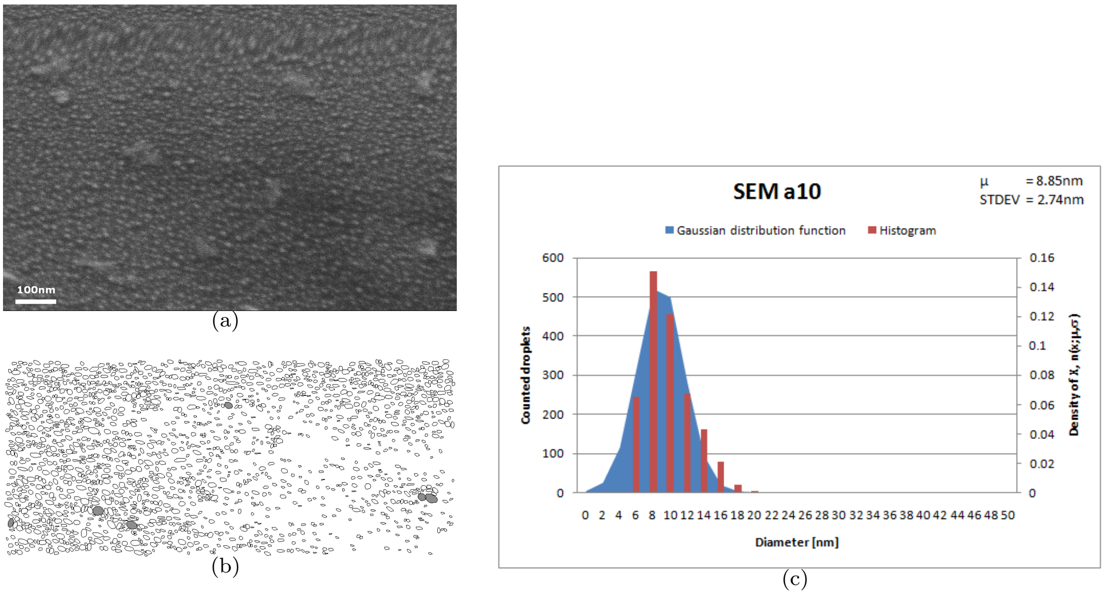

(a) (b) (c)

Figure B.9: SEM picture of Au droplets on a-plane sapphire substrate annealed at 1000°C.

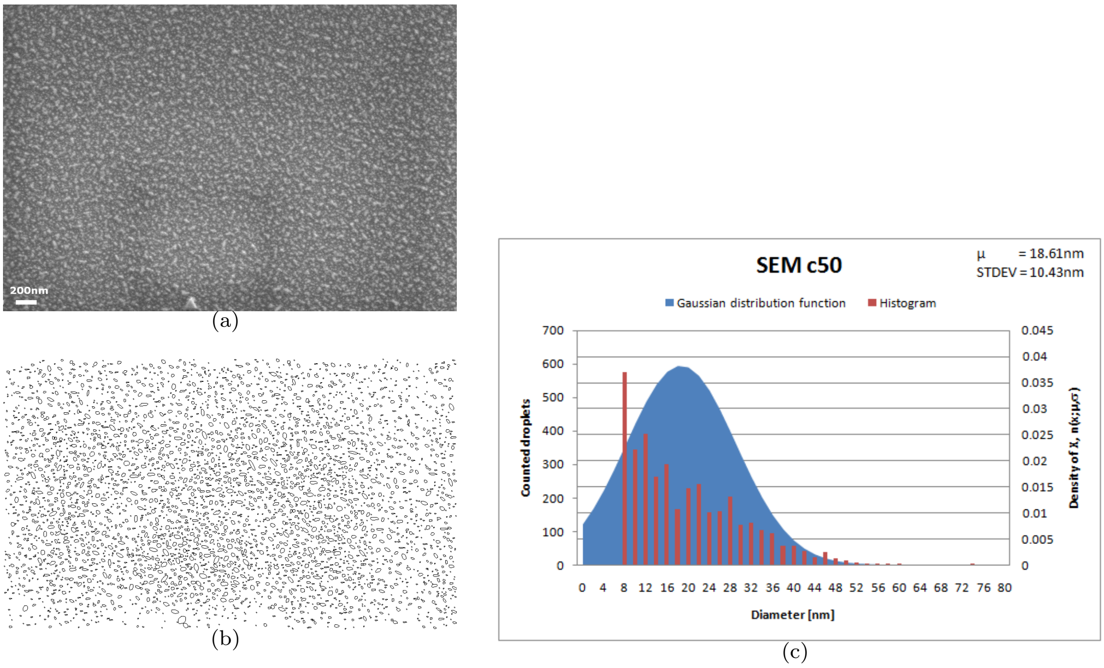

(a) (b) (c)

Figure B.10: SEM picture of Au droplets on un-annealed c-plane sapphire substrate.

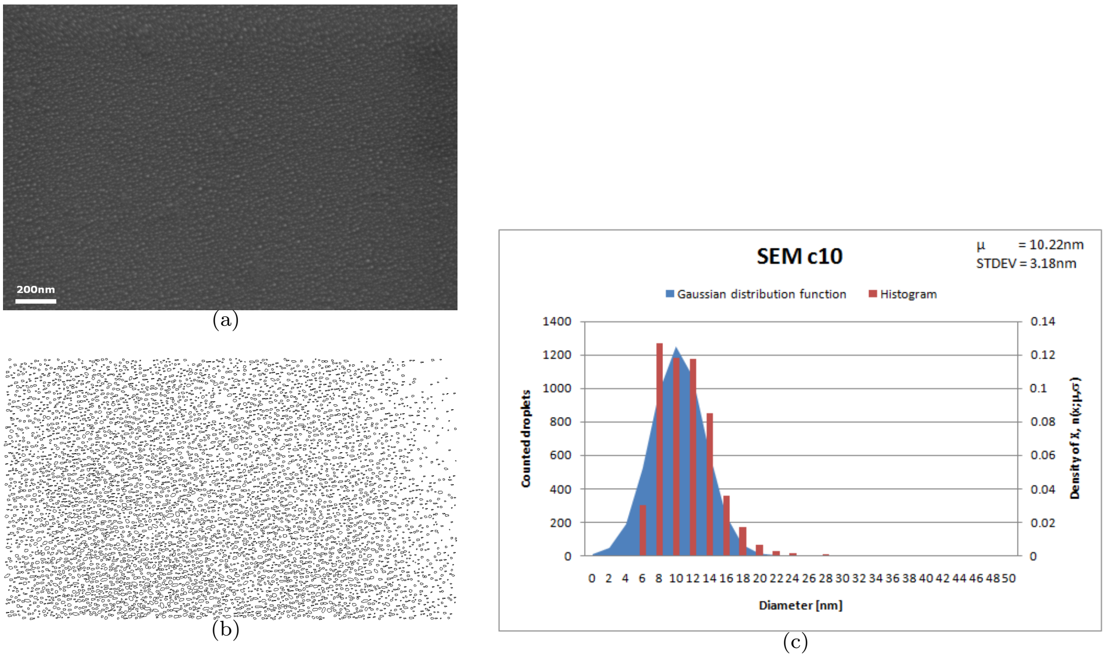

(a)

(b)

(c)

Figure B.11: SEM picture of Au droplets on c-plane sapphire substrate annealed at 1000°C.

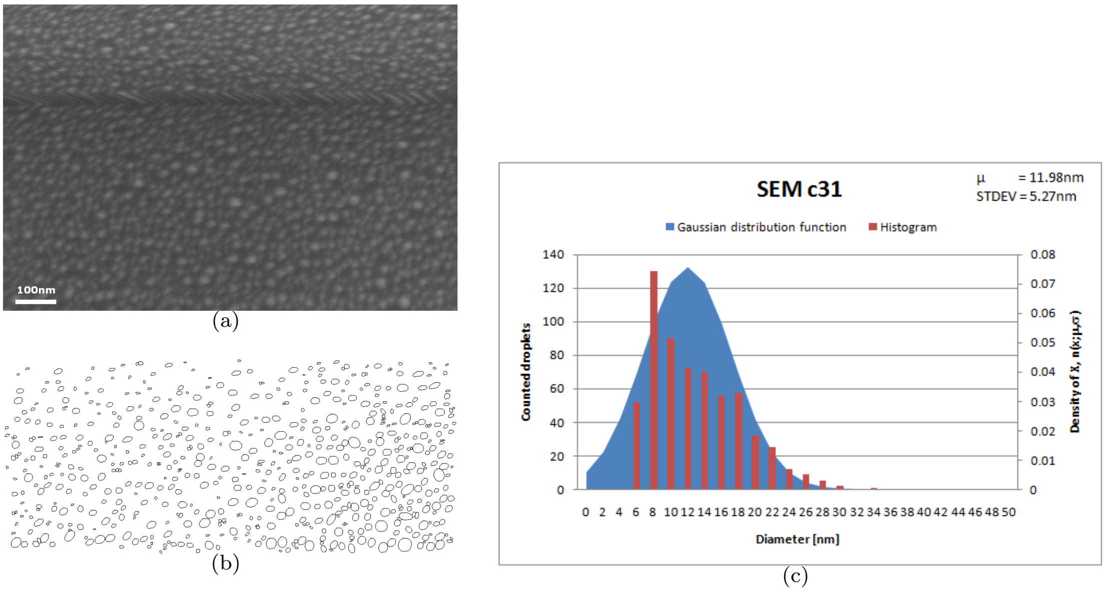

(a)

(b)

(c)

Figure B.12: SEM picture of Au droplets on c-plane sapphire substrate annealed at 1400°C.

Sample	Substrate	AFM						SEM		
	ann.temp. [°C]	0.5μm	1μm	2μm	5μm	10μm	20μm	10kx	50kx	100kx
a50	-	x	x	x	x	x				
a10	1000°C	x	x	x	x	x		x	x	x
a21	1200°C	x	x	x	x	x				
a31	1400°C	x	x	x	x	x	x	x		
c50	-	x	x	x	x			x	x	
c10	1000°C	x	x	x	x		x	x	x	
c21	1200°C	x	x	x	x	x	x			
c31	1400°C	x	x	x	x	x	x	x	x	x

Table B.1: Characterization summary of Au droplets.